REVIEW

Check for updates

2D material-based sensing devices: an update

Jahan Zeb Hassan, [iD] †[a] Ali Raza, [iD] †*[b] Zaheer Ud Din Babar, [iD] †[bc] Usman Qumar,[a] Ngeywo Tolbert Kaner [iD] [d] and Antonio Cassinese [iD] [b]

In recent decades, two-dimensional materials have attracted significant attention due to their unique chemical and physical properties, which are useful for various applications. In addition to optoelectronic devices and energy harvesting and storage, 2D materials are used in many sensing applications. Two-dimensional structures have numerous attributes, such as high surface sensitivity, excellent biocompatibility, and high elasticity, making them effective as sensing devices. In this review, we aim to provide an update on the recent developments in the field of sensors fabricated using atomically thin 2D materials. A survey of different types of sensors is presented, including gas, electrochemical, biomedical, and health sensors, together with recent findings on their real-world applications. Furthermore, human body temperature monitoring, electrography, sweat detection, respiratory gas, and saliva sensors are also reviewed to assess current trends toward human chemical signal detection. Given that 2D materials encompass a vast array of novel materials, we highlight the contemporary trend in the applications of 2D materials and suggest the exciting future of the 2D family. By thoroughly addressing the fundamental aspects, recent developments, and associated challenges, our recommendation in terms of future challenges and prospects will pave the way for readers.

[a]Department of Physics, Riphah Institute of Computing and Applied Sciences (RICAS), Riphah International University, 14 Ali Road, Lahore, Pakistan

[b]Department of Physics "Ettore Pancini", University of Naples Federico II, Piazzale Tecchio, 80, 80125 Naples, Italy. E-mail: ali.raza@unina.it

[c]Scuola Superiore Meridionale (SSM), University of Naples Federico II, Largo S. Marcellino, 10, 80138, Italy

[d]School of Physics, Harbin Institute of Technology, Harbin 150001, China

† J. Z. Hassan, A. Raza, and Z. U. D. Babar contributed equally to this work.

Jahan Zeb Hassan obtained his M. Sc. degree in physics from the University of Gujrat, Pakistan, in 2017 and M. Phil from Riphah International University, Islamabad, in 2020. Hassan completed his research work in Solar Cell Applications Lab at GCU Lahore. He later worked as Research Assistant in the same lab to synthesize 2D materials for energy harvesting applications. Hassan worked as Lecturer (visiting) in Physics at GC University Faisalabad (Chanab College Sub Campus). Currently, he is a Member of American Physical Society with research direction of designing layered materials for sensing and storage devices.

Ali Raza obtained his BS (Physics) degree from the University of Gujrat (Pakistan) in 2016 and Master's in Material Physics from Riphah International University, Islamabad, in 2019. Raza completed his M. Phil research in the Solar Cell Applications Lab at GCU Lahore and later worked as Research Associate in the same lab in the field of catalytic and energy harvesting applications of pure and engineered 2D materials (TMDCs, Graphene, h-BN, and MXenes). Later, he served as Lecturer (Research) at the Department of Physics, University of Sialkot. Currently, he is a doctoral fellow at the Department of Physics "Ettore Pancini", University of Naples Federico II, Italy. His current research directions are the fabrication of functional 2D materials for sensing and green energy-harvesting applications.

6016 | *J. Mater. Chem. A*, 2023, **11**, 6016–6063

This journal is © The Royal Society of Chemistry 2023

1 Introduction

Over the past two decades, research on 2D materials has witnessed a remarkable increase after Geim and Novoselov's ground-breaking experiments in 2004 and the discovery of graphene.[1] Since then, based on its exceptional physical characteristics, graphene has become prominent in various research areas of nanoscience and condensed matter physics/chemistry, significantly contributing to a wide range of interdisciplinary fields. Accordingly, the large-scale preparation of graphene-based materials has gained extensive consideration, leading to cutting-edge research and innovative technologies.

Concurrently, various enterprises and manufacturers have contributed to the industrialization of graphene. Furthermore, due to its physicochemical characteristics and wide spectrum of applications, interest in graphene has shifted beyond academics to scientific research and industry.[2] However, its susceptible nature to oxidative environments, evidence of certain toxicity, and ideal conductive characteristics, which make it unswitchable, are the primary shortcomings of this wonder material.[3] Thus, the initial enthusiasm created by the "graphene rush" has shifted to exploring more stable and atomically thin materials. Examples of this type of layered materials are boron nitride,[4] recently discovered class of

Zaheer Ud Din Babar earned his MS in Physics from National University of Sciences and Technology (NUST), Pakistan, in 2019. During his Master's research, he investigated the magnetic properties of Nb_2C MXene and reported its superconductive nature. Currently, Babar is a PhD Scholar in "Mathematical and Physical Sciences for Advanced Materials and Technologies (MPHS)" at Scuola Superiore Meridionale (SSM) and pursuing his research project at the Department of Physics "E. Pancini", University of Naples Federico II, Italy. His current research interest includes the synthesis of 2D-MXenes and their nanocomposites with gold and magnetic nanoparticles for (bio)sensing applications.

Ngeywo Tolbert Kane received his Bachelor of Education (Science) degree with honors from Moi University, Eldoret (Kenya), in 2006. He completed his Master of Science in Physics (2014–2016) at the University of Eldoret. Currently, he is a final year PhD scholar in Physics at the Harbin Institute of Technology (HIT, China). His work is on nonlinear optics in emerging two-dimensional ferroelectrics, sensing, and electronic devices under the mentorship of Professor Yongyuan Jiang.

Usman Qumar obtained his M.Sc. in Physics from the University of Gujrat (Pakistan) in 2017 and his M. Phil (Physics) from Riphah International University, Islamabad in 2020. Qumar performed his M. Phil research in the Solar Cell Applications Lab at GCU Lahore and later worked as a Research Assistant at the department of Physics Riphah International University Lahore Campus. Currently, he is working as a lecturer (visiting) in the Physics department at University of Gujrat. His current research areas are the fabrication of 2D materials for energy harvesting (chemical and mechanical) applications. Qumar is a member of international journal of Pakistan Science Society and American Physical Society (APS).

Antonio Cassinese is a Professor of Experimental Physics of Matter at the Department of Physics, University of Naples Federico II. He received PhD in Physics at the same University in 1996, spending a period as Associated Research at the CERN Laboratories and the University of Wuppertal, Germany, under Marie Curie individual fellowship. From 2002 to 2014, he was a permanent Researcher at the University of Naples Federico II. The scientific activity was carried out to investigate the electrical properties of superconductors, oxides, organic (polymer), and inorganic hybrids materials to understand physical fundamental aspects and possible practical applications in the electronic fields. He produced more than 200 research publications in peer-reviewed journals. Currently, Cassinese is running a research group with activities belonging to the fabrication of 2D and organic materials for electronic devices and manipulation of spin with high Q microwave cavities for quantum sensing applications.

This journal is © The Royal Society of Chemistry 2023

J. Mater. Chem. A, 2023, **11**, 6016–6063 | **6017**

materials (e.g., MXenes) composed of transition metal carbonitrides, nitrides, and carbides,[5] semiconducting transition metal dichalcogenides (TMDCs),[6] and phosphorene.[7–9] Table 1 presents some of the principal advancements and recent discoveries in the field of 2D materials. Several pioneering discoveries regarding liquid phase exfoliation are also discussed, including biomedical and sensing applications. The wide range of physical and chemical properties of 2D materials shows significant possibilities for applied research, given that their properties are dependent on their dimensionality.[10] Further, various optoelectronic characteristics can be realized, ranging from the extraordinary semi-metal conductivity of graphene[11] to the semiconducting properties of certain TMDCs.[12] These TMDCs provide a tunable bandgap energy with easy conversion from bulk materials (indirect-form) to single-layered materials (direct-form).[13] These properties result in distinct photoluminescence (PL) characteristics, thus permitting diverse applications, e.g., electroluminescent devices,[14] photodetectors,[15] luminescent probes,[16] and transistors.[17] Furthermore, chemical functionalization can offer desirable optoelectronic properties in the above-mentioned 2D materials. For example, due to their large surface/volume ratio, their demand has increased in the field of sensing and broadened their application area from the quantitative determination of heavy metal ions (e.g., Cd^{2+}, Pb^{2+}, As^{3+}, and Hg^{2+}),[18] gases (e.g., NH_3),[19] and ultrasensitive detection of essential biomolecules (e.g., DNA and proteins)[20] to single molecule detection[21] and beyond.[22] Notably, 2D material-based sensors do not possess intrinsic properties to interact with target molecules selectively. Thus, it is possible to manipulate the interaction between 2D nanosheets and molecules/ions by modifying their inherent properties. Chemical adsorption (i.e., chemisorption) of interacting

substances via covalent bonds on the basal planes of 2D materials provides significant control of their sensing profile. In contrast, physical adsorption (i.e., physisorption) of interacting molecules on the basal planes of 2D materials via non-covalent interactions is preferred in sensing.[23] These non-covalent interactions offer high recovery rates and are considered promising for real-time monitoring and rapid onsite analysis. Given that physisorption depends on the nature of the molecules and the interacting surface, it has certain limitations. This involves the ineffective and unstable immobilization of molecules, which can potentially cause false positive and negative results. Primarily, a direct electrical response is desirable for practical applications, where the interaction of analytes with 2D materials generates an enticing optical response, for instance, a variation in PL characteristics offers a variety of opportunities. Graphene and its oxide (GO) are known to be effective fluorescence quenchers compared to organic substances. Hence, Förster resonance energy transfer (FRET) sensors have attracted significant attention in recent years, particularly in biomedical applications. Generally, in biomedical applications, FRET can detect in vitro and in vivo changes and be used to precisely measure nanometer-scale distances.[24] This has resulted in the development of nano-biosensors with exceptional selectivity, increased bio-stability, and improved sensitivity. In this regard, single-layer MoS_2 nanosheets with superior fluorescence quenching efficiency are a suitable sensing platform for small molecule determination and DNA detection.[25] The use of 2D materials in FRET sensors is not limited to energy acceptors. Alternatively, suitable functionalization produces photoluminescent flakes, which act as energy donors, and thus quenched by electron-deficient compounds, e.g., for the detection of trinitrophenol, which is an integral component of intense

Table 1 Principal advancements and recent discoveries in 2D materials flatland

Material	Timeline	Comments	Ref.
		Hallmarks in discovery, exfoliations, and sensing applications	
TMCCs	2022	Discovery and first report of liquid phase exfoliation[a]	42
MBenes	2017	Discovery of MBenes	43
	2018	Liquid phase exfoliation[b]	44
	2021	In silico study on destabilization of amyloid-β accumulation	45
MXenes	2011	Liquid phase exfoliation[c]	46
	2014	$Ti_3C_2T_x$ nanosheets towards H_2O_2 sensing	47
	2017	$Ti_3C_2T_x$ nanosheets for photothermal conversion	48
Graphene	2004	Synthesis of single-layer graphene	49
	2008	First report on DNA sensing	50
	2008	Earliest findings on drug delivery for cancer treatment	51
	2009	Liquid-phase exfoliation[d]	52
TMDCs	1986	First studies on a single-layer MoS_2	53
	2011	Liquid-phase exfoliation[e]	54
	2011	Detection of NO at room temperature	55
	2013	Earliest study on MoS_2 as NIR photothermal agent	56

Abbreviations: TMCCs = transition metal carbo-chalcogenides (a combination of MXenes and TMDCs at the atomic level), MBenes = transition metal borides, NIR = near-infrared. [a] TM_2X_2C layers were intercalated electrochemically with lithium and subsequently sonicated in water. [b] Synthesis of 2D-CrB (MBene) by immersing Cr_2AlB_2 (MAB phase) in HCl for 6 h at room temperature. [c] Ti_3AlC_2 MAX powder was immersed in 50% HF solution at RT for 2 h. [d] Immersion and exfoliation of graphite in an organic solvent such as N-methyl-pyrrolidone. [e] Immersion of MoS_2, WS_2, and BN in various organic solvents followed by bath sonication and centrifuge.

6018 | J. Mater. Chem. A, 2023, 11, 6016–6063

This journal is © The Royal Society of Chemistry 2023

explosives.[26] Recently, 2D materials have been the focus of research for the fabrication of extremely selective and sensitive sensing devices to detect organic vapors, humidity, and hazardous chemicals. These 2D material-based devices are widely used in emission control, environmental monitoring, and diagnosis. In this regard, a broad spectrum of materials has been developed, ranging from carbon materials to metal oxides and various polymers. Certainly, 2D materials should be highlighted owing to their noteworthy features and potential use.[27,28] These materials include layered metal oxides, black phosphorus, hexagonal boron nitride (h-BN), pnictogens, TMDCs, and MXenes. Because of their high adsorption capacity and broad surface area, these materials exhibit improved performances for gas sensing. Two configurations of the above-mentioned 2D materials have been utilized in gas sensors, *i.e.*, field-effect transistors (FETs)[29] and chemiresistors.[30] Because of their ease of attachment, point-of-care sensing, and the ability to construct compact wearable electronic devices, 2D materials have become superior technology for assessing human physiological signals.

They play a vital role in disease diagnosis, regular health assessment, rehabilitation treatment, and preventive medicine.[31,32] Currently, in the fabrication of conventional wearable products mainly containing silicon and organic materials, biological compatibility is not an issue. Consequently, researchers are focused on developing multipurpose wearable electronic devices with pertinent features such as light weight, flexibility, and increased performance. These features can enable the development of devices with superior recognition of different types of electrography[33] including electromyography, electro-oculography, electroencephalography, and electrocardiography, which generate mechanical[34,35] and bio-signals in human fluid.[36] These signals greatly influence operational indicators for activities and vital signs. As previously indicated, extensive studies on 2D material-based sensing are motivated by their inherent mechanical properties. In addition to continuous fitness tracking and health monitoring of the wearer and their surroundings, these characteristics can be used to create wearable and portable sensing devices, which can significantly impact our society.[37] Wearable chemical sensors can perform various tasks, including data acquisition, analytical operations, processing, communication, and safety monitoring. In this case, it is crucial to assess the trends of smart technologies and their possible future activities concerning 2D materials.

Several reviews have been published on 2D materials;[24,38–41] however, the current review presents an update on the recent development in the field of sensor devices comprised of atomically thin 2D materials. An investigation on different types of sensors is presented, including gas, electrochemical sensing, biomedical, and healthcare sensors, with recent studies on the active application areas of these materials (see Fig. 1). This study considers different aspects of various sensing applications, including human chemical signal monitoring and personalized healthcare; and also outlines the current challenges and future perspective of these 2D materials.
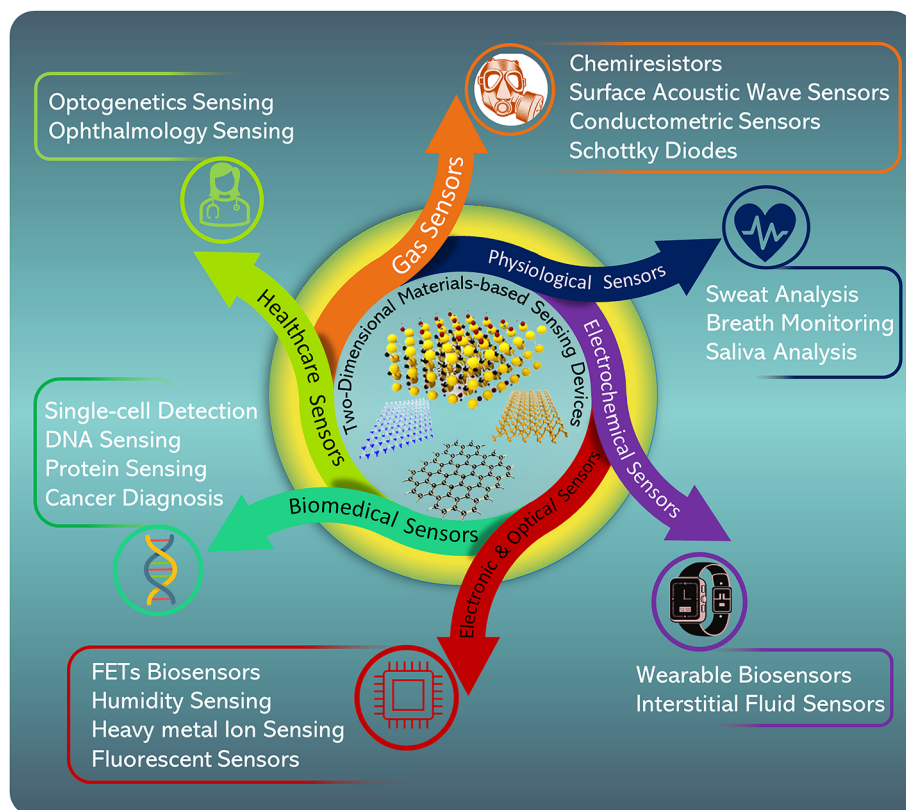

Fig. 1 Highlights of 2D materials in various sensing devices.

This journal is © The Royal Society of Chemistry 2023

J. Mater. Chem. A, 2023, **11**, 6016–6063 | **6019**

2 Why 2D materials for sensing?

2D materials have variable thicknesses ranging from a few nanometers to several centimeters,[38,57,58] providing exceptional physiochemical properties that are useful for chemical detection through electrical transduction (Fig. 2). Among them, graphene, an atomically thin 2D carbon nanosheet with a hexagonal crystalline structure, has dominant physiochemical, electro-optical, and thermal–mechanical properties and holds great promise for application in chemical and biological sensors, electronics, photonics, medicine, and energy conversion and storage.[49,59,60] 2D materials such as phosphorene,[8] h-BN,[61] TMDCs,[62] layered metal oxides,[63] 2D metal–organic frameworks (MOFs),[64] covalent organic frameworks (COFs),[65] and several other 2D compounds[66] have been significantly employed during the past ten years. Depending on the type of sensor, transduction mechanism, and inherent properties, 2D materials can substantially improve the performance of the sensor. 2D materials exhibit remarkable characteristics, which provide sensitive sensing compared to their bulk counterparts (Table 2). 2D materials have some particular features such as good in-plane stability and extended surface for molecular interactions, i.e., monolayer graphene contains a surface area with a theoretical maximum of 2630 cm^2 g^{-1}.[67] Furthermore, the quantum confinement arising perpendicular to the 2D plane leads to unique optical and electrical properties such as large carrier mobility (μ) of 10^4 cm^2 V^{-1} s^{-1} for graphene[68,69] and tunable bandgap, i.e., 1.2 to 1.8 eV, for 2H phase MoS_2,[70–72] which makes MoS_2 a potential candidate for a multitude of potential applications in optoelectronics.[71,73–75]

Generally, considering the surface effects of 2D materials, they offer a vast surface area for enhanced molecular interactions, enabling high sensitivity and extremely low detection limits, even for ultralow analyte concentrations. Additionally, the active sites on their surface boost their interaction with the target species and facilitate the immobilization of additional recognition elements, such as metallic nanoparticles (NPs) and receptors. In the case of electrochemical sensing, the presence of active sites endows these materials with electrocatalytic characteristics that enhance the current, while lowering the redox potential in the presence of the analyte. In addition, good selectivity can be achieved using 2D material-based sensors by taking advantage of their rich surface chemistry, which can be enhanced through chemical functionalization or defect engineering.[76–78] Furthermore, considering the factors such as sensitivity and selectivity can also enhance the performance of sensors, improving their detection efficiency.[79,80] Wang et al. showed that glassy carbon electrodes coated with graphene could increase the faradaic current by 20 times, while lowering the reduction potential of H_2O_2 by about 0.4 V.[77] Another aspect of graphene-based sensors is that there are several approaches to increase their specificity and selectivity. In this case, one practical approach is to decorate the basal plane of graphene with different organic groups and biomolecules, which act as receptors for the analyte of interest.[81,82]

Here, covalent and non-covalent approaches are the two main categories of surface modification or functionalization techniques (e.g., chemical) commonly used to enhance the sensing potential of 2D materials.[79,83,84] Covalent methods are recognized as reliable and allow the attachment of functional groups to the surface of 2D materials, allowing the modification
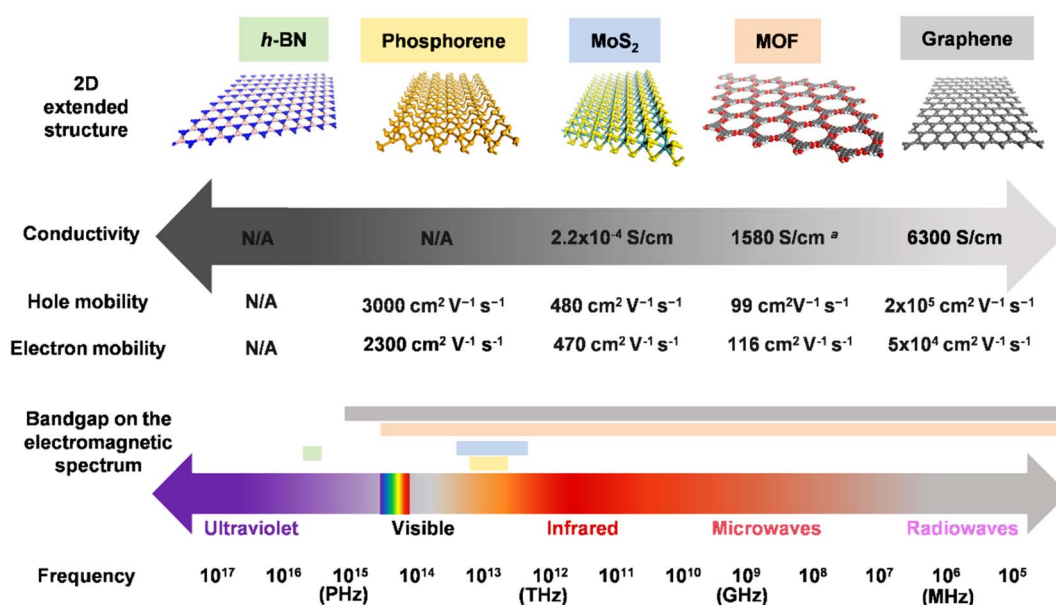

Fig. 2 Various atomically thin 2D crystals with corresponding carrier mobilities, conductivities, and electronic bandgap energy.[101] 2D materials possess a variety of chemical structures, for instance, h-BN,[102] MOFs,[103] and MoS2,[104] contain a mixed structure of elements, while black phosphorus[105] and graphene[106] are composed of pure elemental sheets. There is a wide range of electronic structures in 2D materials, ranging from insulation in h-BN to metallic conductivity in graphene. The broad spectrum of properties of different 2D materials introduces a paradigm shift in the field of sensing. Adapted with permission from ref. 38 Copyright 2019, the American Chemical Society.

6020 | J. Mater. Chem. A, 2023, 11, 6016–6063

This journal is © The Royal Society of Chemistry 2023

Table 2 Comparison of different characteristics of various 2D materials as a sensing platform

Materials	Conductivity charge mobility	Band structure and bandgap	Properties		Biocompatibility cytotoxicity	Applications
			Chemical stability	Surface functionalization		
TMCCs	Recently discovered family of 2D materials[a]					To be determined
MBenes	Metallic conductivity[43]	Metallic[107,b]	Manifest outstanding stability in aqueous media at ambient conditions[107]	No experimental evidence shows the presence of terminal groups on the surface of MBenes[c]	Better compatibility and negligible cytotoxicity[d]	In silico study on amyloid-β deformation[45,e]
MXenes	Up to 2.4×10^4 S cm^{-1}. DC conductivity of ≈ 9880 S cm^{-1} in Ti$_3$C$_2$T$_x$ films produced by spin coating[108,f]	Tunable bandgap via intercalation and terminations[109,110]. Bare MXenes are metallic, while terminated ones are predicted to be semiconducting[111]. Metallic for Ti$_3$C$_2$	Offer a homogeneous suspension in aqueous solutions; however, susceptible to oxidation under ambient conditions and/or in an oxygen-rich environment[95,112]	Abundant intrinsic surface terminations offer profuse loading of analyte-sensitive species for biorecognition and VOC sensing[95,113–115]	Biocompatible and negligible cytotoxicity[116,117]	Electrochemical, optical, gas, stress/strain sensors, and many biomedical applications[118,119]
Graphene	Carrier mobility in the order of 10^3 at RT[120]	Unique structure with zero band gap (BL graphene) but tunable up to 250 meV[121,122,g]	GO has improved dispersion in aqueous solutions and is relatively stable[123]	However, no intrinsic surface termination in pristine graphene can be functionalized for sensing applications[124,125]	Cytotoxic have biosafety concerns[126,127]	Do[76,128]
TMDCs	(i) SL MoS$_2$ has charge mobility of 200 cm^2 V^{-1} s^{-1} at RT[129]. (ii) The conductivity of 5.0 S cm^{-1} (MoS$_2$)[130]	Tunable bandgaps[130]. SL MoS$_2$ = 1.8 eV. SL WS$_2$ = 1.45 eV. SL WSe$_2$ = 1.7 eV	Degradation occurs in a moisture and oxygen environment[131]	Lacking intrinsic surface functionalization of external species linkage[132]	TMDCs have variable cytotoxicity reported[133,134]	Do[19,135]

Abbreviations: BL = bilayer, SL = single layer. [a] According to ab initio calculations, the bandgap is predicted to be metallic, while other properties are yet to be determined. However, the initial study only reports its superconductivity. [b] MBenes have prominent Fermi states and are metallic; however, thorough studies are required to determine a figure of merit. [c] According to the preliminary reports on MBenes, it is easy to terminate the MBenes surface with O, OH, and F functional groups after exfoliating from their bulk MAB phases. However, few theoretical studies suggest that functionalized MBenes have better redox electrochemistry and have potential in lithium–sulfur batteries.[136] [d] So far, the cytotoxicity and biocompatibility of 2D MBenes have not been extensively investigated and should be explored further. [e] Molecular dynamic simulations were performed on the prevention of Aβ amyloid aggregation (a potential biomarker of Alzheimer's and Parkinson's disease). [f] Ti$_3$C$_2$T$_x$ produced by EN-MILD method. [g] In sp^2 hybridized graphene, π-electrons move freely on the surface, providing a high electron transfer rate that makes it suitable to fabricate electrochemical transducers.[137]

This journal is © The Royal Society of Chemistry 2023

J. Mater. Chem. A, 2023, **11**, 6016–6063 | **6021**

of their crystalline structure and resultant electrical characteristics.[85,86] However, although 2D materials exhibit effective selectivity, altering their surface can change their electrical nature, making them poor choices for sensing. Furthermore, the covalent functionalization of graphene has the concomitant drawback of reducing its conductivity. In contrast, flexible non-covalent functionalization enables the modification of the electrical and physical characteristics of 2D materials without affecting their crystalline structure.

Moreover, the non-covalent features of 2D materials can be studied based on their van der Waals, electrostatic, and π–π interactions, which can be used to change the doping concentrations in a controllable way.[87] Given that conductivity is a characteristic of graphene and other 2D materials that improves sensitivity, particularly in electrically transduced sensors,[38] it is now conceivable to scale miniature devices due to the exceptional charge transport properties of 2D materials, which are preserved in thin sub-nanometer layers. Furthermore, the large lateral dimensions of 2D materials ensure excellent electrical contacts in electronic devices.[88]

In particular, the exceptional sensing ability of 2D materials in gas sensing can be explained by several of their properties. The entire surface of these materials is available to adsorb gases due to their 2D structure, which maximizes their interaction with the surface. Furthermore, noise reduction is guaranteed by their excellent crystallinity and good conductivity. Also, the low-resistance ohmic connections on graphene allow its simple integration with a range of device topologies. Based on these notions, Novoselov and colleagues demonstrated a sensitive graphene sensor capable of identifying a single gas molecule interacting with its surface.[89] The authors showed that graphene is a 2D material that is electrically quiet and suitable for the fabrication of single-electron detectors. 2D materials are excellent candidates for sensing applications due to their above-mentioned physical and chemical characteristics. Presently, a wide variety of top-down and bottom-up synthetic protocols has been created and developed to fine-tune the number of layers, lateral dimensions, composition, and overall quality of 2D materials, enabling their unique qualities to be fine-tuned for a particular application. Due to their accessibility and distinct properties, graphene and TMDCs have been extensively studied for applications in sensing.[73,90] However, there are some limitations associated with these materials, particularly in the field of sensing.[87]

The zero band gap of graphene is a significant disadvantage for any optoelectronic application. Similarly, the application and development of MoS_2 is limited by its many shortcomings. Specifically, owing to its high surface energy, the number of electrochemically active sites is reduced by restacking. Also, due to its interaction with oxygen and water, monolayer MoS_2 is unstable in the natural environment.[91,92] When used for electro(bio)chemical sensing, the sensitivity of MoS_2 is limited by its poor electrical conductivity and Young's modulus.[93,94] Recently, due to their outstanding characteristics, individual 2D materials, especially graphene and TMDCs, have received increasing attention in the field of chemical sensing. Accordingly, considering the variety of 2D materials available and their

various qualities, combining them in hybrid structures can be an effective way to benefit from their common features. In this case, different 2D materials can be stacked to create heterostructures using the same van der Waals interactions that hold the layers of 2D materials together in their bulk crystals. In contrast to individual structures, materials in proximity to the heterojunction exhibit a synergistic effect, resulting in new and improved properties. Furthermore, doping can provide additional control to change the aforementioned physical characteristics of 2D materials. According to Wang *et al.*, doping graphene with heteroatoms can modify its electrocatalytic characteristics, further improving the performance of the fabricated electrodes. Consequently, the electrodes modified with graphene and N-doped graphene showed remarkable sensitivity for the detection of H_2O_2 and glucose. Additionally, a new class of 2D materials known as MXenes has attracted significant interest from the scientific community and is being extensively investigated for use in sensing applications.[95] The tunable surface chemistry and versatile physical properties of MXene introduce new sensing capabilities and successfully circumvent several limitations.

2.1 2D monoelements

The most obvious alternatives to graphene are the other elements in group IVA, which have the same number of electrons. However, 2D materials are an emerging field, and thus their potential has not been fully realized and the degree of their potential properties and highly efficient commercial-level device applications remain untapped.[27,96] To date, numerous theoretical calculations have been performed to evaluate their basic properties, while experimental investigations are in their early stage, while practical synthesis methods are being investigated to introduce definite synthetic routes and possible limitations. In this case, the neighboring groups to group IVA (VA and VIA) provide a solution of some of these limitations due to their sizeable bandgap, which is advantageous for logic electronics. One closely associated category of 2D crystals is single-element 2D Xenes, which obtain their etymology from sp^2-hybridized alkene bond and usually consist of a single layer of atoms arranged in a honeycomb-like structure.[97] The electronic structures of group IVA Xenes, *i.e.*, silicene, germanene, and stanene (where X = Si, Ge, and Sn, respectively), which are regarded as counterparts to graphene, are known to fluctuate remarkably. In particular, group IVA Xenes exhibit isoelectronic properties to graphene. Similarly, up-and-down atomic bulking around their honeycomb structure results in more considerable interatomic distances, providing a novel route toward covalent functionalization.

The buckled structure and inherent strong spin-orbital coupling identified in the 2D topological insulators provide a path for an advanced quantum state of matter. In the bulk form, solid-state materials have an insulating electronic configuration and small dissipated conducting channels around all their edges, which are protected from backscattering by time-reversal symmetry. This the 2D topological insulator effect can facilitate the realization of materials with exceptional

6022 | *J. Mater. Chem. A*, 2023, **11**, 6016–6063

This journal is © The Royal Society of Chemistry 2023

conductivity and completely shielded from defects and scattering disturbances. The electronic nature and stability of 2D Xenes are significant concerns in realizing realistic Xene-based devices, particularly in sensing. Specifically, free-standing sheets from group IVA elements contain higher consistency under normal conditions, which is a complicated matter. In this case, the use of chemical approaches to control the functional groups present in 2D Xene materials is a viable method for regulating their properties and enhancing their stability. Hence, organic moiety-based functionalization in an ambient temperature and pressure environment is necessary. In nanoelemental nanosheets, every atom in their structure is covalently bonded with a ligand, which cancels out the π bonding. In this case, the ligand pairs covalently with the half-filled P_z-orbital to create a gap.

Also, the semiconducting bandgap configuration and its size are determined by the ligand and the skeleton elements. A buckled structure can be chemically altered by replacing its hydrogen atoms with organic functional groups. Organo-modified graphene quantum dots, germanane, silicane, and other theoretically estimated free-standing 2D group-IV "Xene" materials are very similar. Thus, chemically modified, self-supporting 2D Xene materials are excellent candidates for a nanotechnological strategy that incorporates metaphysical aspects for basic research and application. The fabrication of various silicene and germanene Bi-layer frameworks has been demonstrated both theoretically and experimentally. Some practical conditions, such as external charge distribution and surface stress, determine the formation of these structures. Surface-substituted ligands usually achieve structural flexibility in the entire region between different nanoscale materials. Primarily, carbon atoms form a strong covalent bond between them owing to their various hybridization states (sp, sp^2, and sp^3), which enable the development of structures with varying arrangements. The various carbon allotropes are well-developed, and among them, the planar honeycomb lattice is the most attractive. Although 2D graphene has a perfect carbon atom arrangement, its gapless structure limits its practical use in nanodevices. Alternatively, due to their high quantum confinement and edge effects, functionalized graphene and nano-sized graphene fragments can be used in bandgap applications. Quantum confinement exists in graphene regardless of its size, which results in intriguing behaviors that do not appear in typical semiconducting nanocrystals. Usually, an oxygen-rich environment results in the oxidation of 2D Xenes,[98,99] while ultrahigh vacuum can drastically reduce this phenomenon.[99] However, the decomposition mechanism is unclear, and oxidation may still occur through other atmospheric molecules, such as water.[100]

3 Various sensing platforms

Sensing is essential to monitor harmful environmental chemicals, detect toxic gases, diagnose diseases, and monitor human health. Thus, the development of robust and efficient sensing systems to detect specific analytes (chemical and/or biological) such as gases, toxic ions, chemicals, and biomolecules, while maintaining stability, sensitivity, and selectivity for particular domains is critical in various applications. In this section, we introduce various 2D materials to create sensor systems, including electrical, fluorescence, electrochemical, and biomedical sensors. 2D materials, including graphene and TMDCs enable the development of different sensing platforms to detect a variety of external species owing to their excellent conductivity, wide effective surface area, enhanced sensitivity, and exceptional potential to quench the fluorescence signal.

3.1 Gas sensors

3.1.1 Chemiresistors. Chemiresistors are the most extensively studied among classes of gas-sensing devices. In this type of sensor, gas molecules adsorbed on the surface of the sensing substrate change the electrical resistance, thus allowing a sensitive detection.[138] Furthermore, chemiresistors have a variety of benefits, including ease of manufacturing, ease of operation, low cost, eco-friendly nature, and the potential for further downsizing.[139,140] Chemiresistors are composed of sensing materials produced via a binary metallic (or interdigitated) transducer and an inert substrate. Moreover, they can detect CO, O_2, Cl_2, H_2, SO_x, and NO_x with various organic gases.[141,142] Chemiresistors were produced (via spin-coating) using chemically derived single-layer graphene sheets over double-sensor substrates composed of distinct materials, consisting of four-point electrodes and micro-hot plates. The four-point electrodes were engaged on thermally developed SiO_2, whereas the micro-hot plates were designed on Si_3N_4 using a small stress approach. The proposed sensors were used to detect NH_3, NO_2, and 2,4-dinitrotoluene. Simultaneously, the micro-hot plate sensors could be used to examine the temperature dependence of the NO_2 reaction.[143] However, it is important to highlight that for 2,4-dinitrotoluene, which is a relatively volatile component present in trinitrotoluene explosives, the proposed sensors showed a relatively lower limit of detection (LOD) of 28 parts per billion (ppb) at room temperature (21 °C). Cho et al. employed chemical vapor deposition (CVD) to grow layered MoS_2 using molybdenum trioxide (MoO_3) and sulfur powder as the precursors.[144] They deposited the material on a sapphire substrate, forming interdigitated electrodes with a separation of 100 μm (see Fig. 3a). The transient resistance responses of the sensor were investigated in two analytes gases, i.e., NO_2 and NH_3, at concentrations in the range of 1.2 to 50 ppm. In the NO_2 gas mode, the resistance increased at room temperature and 100 °C (positive sensitivity). In this case, NO_2 acted as an electron acceptor, bringing the Fermi level closer to the valence-band edge and resulting in p-doping. Meanwhile, NH_3 served as an electron donor (i.e., n-doping), shifting the Fermi level of MoS_2 to the conduction-band edge; therefore, it exhibited negative sensitivity at both temperature regimens (see Fig. 3b). The surface of the material was saturated at approximately 20 ppm, regardless of the operating temperature, as observed in Fig. 3c. Finally, the authors also confirmed by DFT the charge-transfer mechanism between the gas molecules and MoS_2, together with its most probable position in the mechanism proposed (see Fig. 3d).
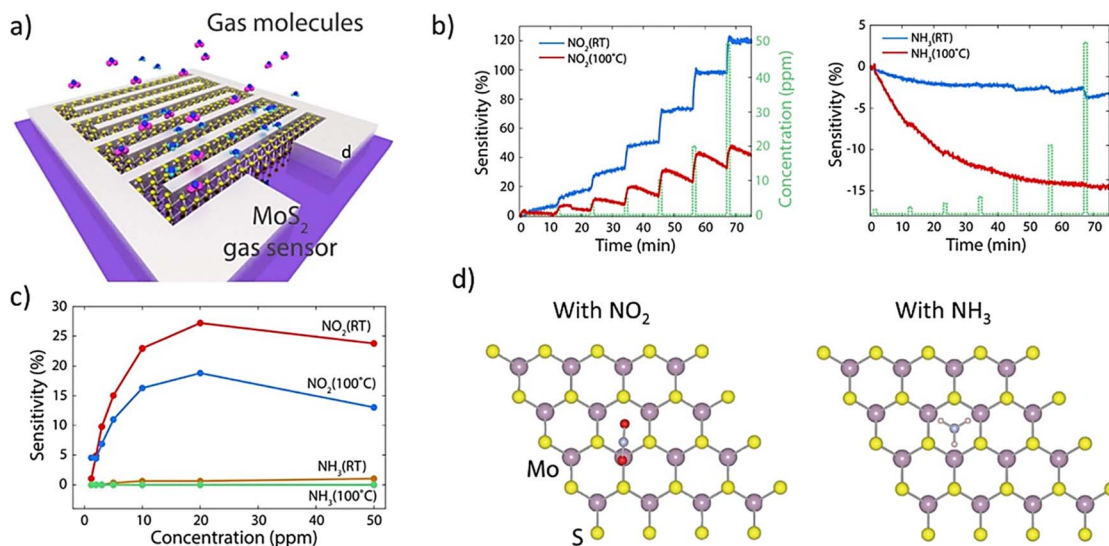
This journal is © The Royal Society of Chemistry 2023

J. Mater. Chem. A, 2023, 11, 6016–6063 | **6023**

Fig. 3 (a) 3D schematic of the interdigitated electrode of MoS$_2$ on sapphire. (b) Transient cure for NO$_2$ (left) and NH$_3$ (right) gas response from 1.5 to 50 ppm gas, operating at room temperature and 100 °C. In the NO$_2$ gas mode, the resistance increased (positive sensitivity). (c) Sensitivity comparison of NO$_2$ and NH$_3$ gases at different gas concentrations and operating temperatures and (d) top views of the most favorable configurations for NO$_2$ (left) and NH$_3$ (right) on MoS$_2$. Adapted with permission from ref. 144 Copyright 2015, Nature Publishing Group.

3.1.2. Surface acoustic wave sensors. Surface acoustic wave (SAW) devices are an innovative class of sensors, which are mainly used as gas sensors because of their small size, low cost, exceptional sensitivity, robustness, and capability to detect an extensive array of gases.[145,146] The velocity or attenuation of the acoustic wave is affected by the fluctuation of the physico-chemical characteristics of the surface of the SAW sensor.[147,148] Most SAW gas sensors detect gas molecules through the fluctuating conductive properties of sensing materials and by mass loading.[149] The selectivity and response modulation of SAW sensors are determined by tuning the properties of the sensing materials and by modifying them with chemically selective substances.[145,150] Various schemes of ZnO-piezoelectric thin film-based SAW sensors are shown in Fig. 4, where an improved performance was obtained *via* GO by incorporating a sensing layer on a glass substrate.[151] The sensitivity of SAW sensors has an inverse relation with thickness, resonance (R_f), and enclosed surface area of GO layers.

3.1.3 Conductometric sensors. Conductometric gas sensors are another type of gas sensor commonly used to detect
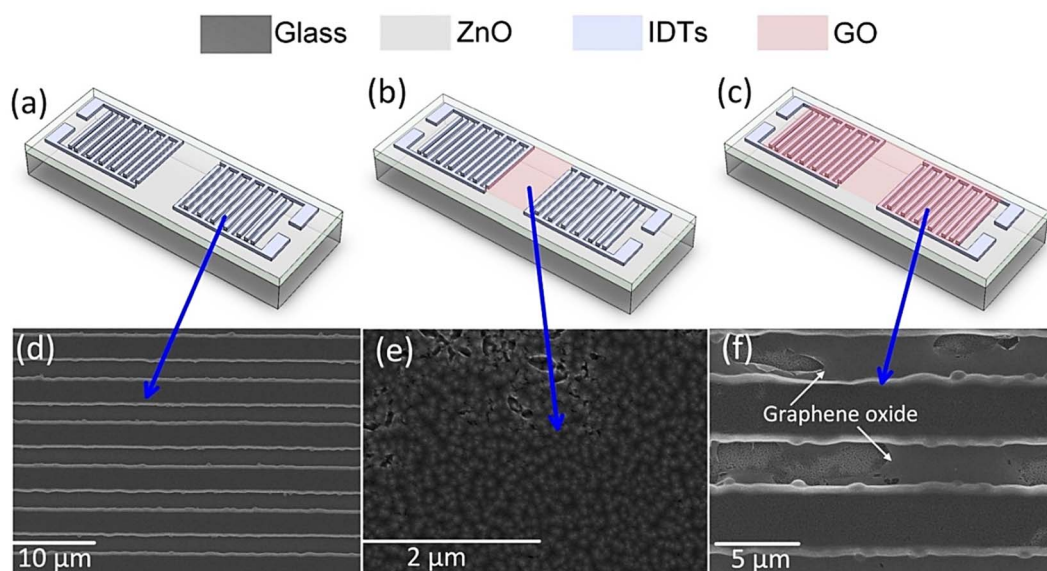

Fig. 4 Schematic of the fabrication of SAW devices: (a) GO layer-coated clean surface, (b) GO layer in the center, and (c) completely covered with GO. SEM micrographs of interdigitated transducers (IDTs): (d) GO layer coated clean surface, (e) GO layer in the center, and (f) completely covered with GO. Adapted with permission from ref. 151 Copyright 2014, Nature Publishing Group.

6024 | *J. Mater. Chem. A*, 2023, **11**, 6016–6063

This journal is © The Royal Society of Chemistry 2023

specific gases,[152–154] particularly under typical atmospheric conditions, owing to their manufacturing flexibility and practicality. Conductometric gas sensors function based on the principle of reversible interaction between the surface of the sensing material and gas molecules.[155] This interaction is influenced by numerous factors, including the physical nature of the sensing material, *e.g.*, surface area and surface additives, and certain external parameters such as temperature and humidity. Subsequently, variations in the conductivity, capacitance, work function, mass, optical properties, and/or reaction kinetics can be used to identify the interaction rate.[156] The sensitivity of conductometric semiconducting gas sensors is critical and can be modified and improved by these surface interactions. Fig. 5a and b show a planar conductometric gas sensor composed of a monolayer MoS_2 channel on an SiO_2/Si wafer. The proposed device demonstrated high selectivity towards various gases/vapors due to the interaction between the MoS_2 monolayer and the physisorbed gases acting as either electron donors or acceptors.[29] The sensing kinetics could be examined by analyzing the variations in the conductance of the channels during a range of analytes. The conductance varied considerably between gases, for example, it increased rapidly in electron donor gases, *e.g.*, triethylamine, but insensitive to electron acceptors, including dichlorobenzene, dichloromethane, nitromethane, nitrotoluene, and water vapor.

3.1.4 Schottky diodes. Schottky devices can be fabricated using layered semiconductor heterojunctions *via* the techniques used to fabricate electronic devices. For instance, a three-terminal active device, graphene variable-barrier "barristor"[157] was fabricated using a layered material, which exhibited a sharp interface between the atomically thin graphene and substrate (*e.g.*, hydrogenated silicon).[158] Modulation of the Fermi energy and Schottky barrier heights (SBH) of these heterojunctions could be achieved *via* gas molecule adsorption over the surface of the sensor material. The density of adsorbed gas molecules is the primary factor affecting the SBH, a variation in which causes reverse currents. Therefore, these features lead to the easy fabrication of Schottky diode gas sensors with high selectivity.[159] A schematic illustration and an optical micrograph of a graphene/Si heterojunction-based Schottky diode sensor are presented in Fig. 5c and d, respectively.[158] Given that reverse biasing determines the work function of SBHs and graphene, it is easy to understand and adjust the degree of sensitivity of the devices. Therefore, Schottky diodes have less power and higher sensitivity rates towards NH_3 and NO_2 detection than graphene-based chemiresistor sensors under similar bias voltage and environmental conditions. Table 3 presents a concise summary of different gas sensing systems based on 2D materials.

3.2 Electrochemical sensors

The evolution of sensor devices has witnessed tremendous growth, leading to the development of numerous sensors exhibiting different sensing mechanisms. Among them, electrochemical sensors, which are sensors in which an electrode acts as a transducer element in the presence of an analyte, are popular preferences because of their documented inherent accuracies. Further, considering their high device sensitivity, instantaneous response, and easy-to-use set-up, these sensor devices are an attractive choice as analytic platforms.[185] The
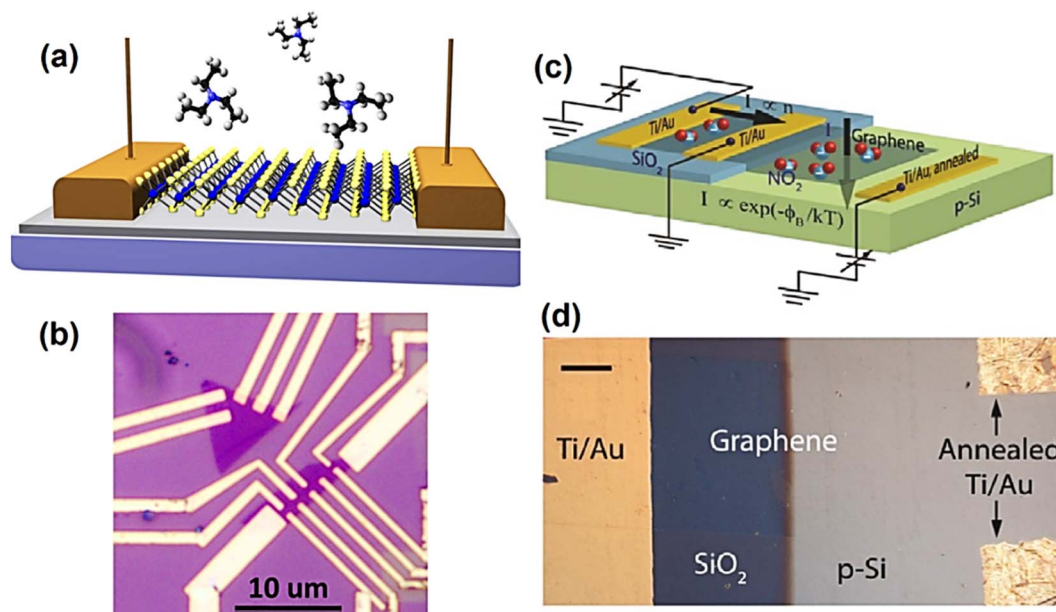

Fig. 5 (a) Schematic of a conductometric sensor and (b) optical image of MoS_2 monolayer–based conductometric sensor translated on SiO_2/Si substrate. Adapted with permission from ref. 29 Copyright 2013, the American Chemical Society. (c) Schematic of the graphene/Si Schottky device fabricated on the same chip. (d) Optical image of graphene/p-Si Schottky diode. This illustrates that graphene is transported over SiO_2 substrate with Ti/Au contacts and p-Si with annealed Ti/Au contact. (Note: scale bar = 200 μm). Adapted with permission from ref. 158 Copyright 2014, John Wiley & Son.

This journal is © The Royal Society of Chemistry 2023

J. Mater. Chem. A, 2023, **11**, 6016–6063 | **6025**

Table 3 2D material-based gas sensing devices

Materials	Synthesis route	Sensing platform	Gases	LOD	Sensitivity	Response time	Ref.
MoS_2	CVD	MoS_2 FET	NO_2 NH_3	20 ppb (NO_2) 1 ppm (NH_3)	>40%	5–9 min	160
	CVD	MoS_2	CO CO_2	500 ppm (CO) 5000 (CO_2)	—	—	161
	CVD	MoS_2	NO_2	0.1 ppb	3.3/ppb (3300/ppm)	—	162
	Solvothermal & in situ polymerization	PANI/MoS_2/SnO_2	NH_3	200 ppb	—	10.9 s (100 ppm)	163
	Hydrothermal	Co-MoS_2	NO_2	100 ppm	—	10 s (100 ppm)	164
	Intercalation-assisted exfoliation	MoS_2 TFT	NO_2	2 ppb	—	>30 min	165
	Micromechanical exfoliation	MoS_2	NO_2 NH_3	—	NO_2 – 1372% NH_3 – 86% (1000 ppm)	30 min	166
	Mechanical exfoliation	MoS_2/GaSe	NO_2	20 ppb	6.3% (20 ppb)	23 s —	167
	Hydrothermal	MoS_2@SnO_2 nanocomposite	NO_2	10 ppm	—	2.2 s	168
	Drop-casting	MoS_2/ZnO nanohybrid	NO_2	0.2 ppb	0.135 ppb	132 s	169
WS_2	Drop coated and	Au-SnO_2-co-decorated WS_2 NS	CO	—	—	3.687 (50 ppm)	170
	Wet-chemical precipitation	WS_2/PbS	NO_2	~20 ppb	—	8.8%	171
	Hydrothermal	WS_2/MWCNTs	TMA	76 ppb	—	—	172
	Liquid exfoliation	WS_2 nanosheets	NO_2	10 ppm 8 ppm	—	45 s (10 ppm) 11 s (8 ppm)	173
	Hydrothermal	WS_2/CuO	NH_3	5 ppm	—	40.5% (5 ppm)	174
g-C_3N_4	Electron beam evaporation.	g-C_3N_4/GaN NRs	NO_2	—	—	42.24% (5 ppm)	175
	Poly condensation	g-C_3N_4 – C/g-C_3N_4	NO_2	50 ppm	—	71.36% (50 ppm)	176
MXene	In situ growth	TiO_2/$Ti_3C_2T_x$	NH_3	30 ppm	—	5 ppb	177
	Ultrasonic spray pyrolysis	$Ti_3C_2T_x$/ZnO	NO_2	100 ppm NO_2	—	—	178
	Wet chemical precipitation	MXene/Co_3O_4	HCHO	0.01 ppm	—	9.2 (10 ppm)	179
	Hydrothermal	SnO_2/MXene	NO_2	30 ppb	—	146 s	180
	Hydrothermal	SnO–SnO_2/$Ti_3C_2T_x$	Acetone	100 ppm	—	12.1 s	181
	LiF + HCl	$Ti_3C_2T_x$/WO_3	NO_2	50 ppm	—	510% (50 ppm)	182
	Hydrothermal	Co_3O_4@PEI/$Ti_3C_2T_x$	NO_x	30 ppb	—	>2 s	183
	DMSO-treated Ti_3C_2 etched powder	$Ti_3C_2T_x$ MXene	NH_3	500 ppm	—	67 s	184

Abbreviations: ppm = parts per million, NRs = nanorings, PEI = polyethylenimine, DMSO = dimethyl sulfoxide, TFT = thin film transistor, HCHO = formaldehyde, and TMA = trimethylamine.

functioning mechanism of these types of sensors relies on detecting the electrochemical reactions between the electrode surface and analytes. Generally, they convert chemical concentrations into quantitative electric signals, the magnitude of which equals the chemical concentration levels. Typically, the measurements using these sensors are based on amperometry, potentiometry, and conductometric. However, not all analytes can induce redox reactions, and thus external mediators are necessary to generate electrochemical signals proportional to the analyte concentration.[186] Consequently, a specific working electrode design modified with 2D materials can improve the quantitative measurement of electrochemical signals during a particular analyte-antigen interaction.[187,188]

In electrochemical sensing devices, the primary detection mechanism involves the transfer of electrons from the active material deposited/coated on the working electrode in a tri-electrode functional structure immersed in an electrolytic-containing solution. In the case of gas sensors, the gases diffuse through a membrane, leading to their oxidation and/or

reduction on the electrode surface. In electrochemical sensors, three distinct types of signals can be obtained using three distinct methodologies, including cyclic voltammetry (CV), amperometry, and differential pulse voltammetry. A large effective surface area, exceptional electrical conductivity, and intrinsic redox potential are imperative parameters that determine the efficiency of electrode materials. Extensive investigations have been conducted on the use of nanomaterials as active sensing materials because of their significant advantages compared to their bulk counterparts. Their small size and large surface area make them ideal for mass transfer and their enhanced signal-to-noise ratio are the major characteristics of electrochemical sensors exploited thus far.[189,190] Also, 2D materials are widely employed as sensing electrodes in electrochemical sensors because of their inherent electrical conductivity, outstanding electrochemical characteristics, and substantial surface-to-volume ratios.[191,192] Recently, 2D graphene and its derivatives, such as rGO (reduced graphene oxide) have emerged as commonly used forms of graphene in

electrochemical sensors. Realizing the impact of using graphene in electrochemical sensors,[193] in this part, we focus on introducing other 2D materials besides derivates of graphene for electrochemical sensing. A wide variety of 2D materials besides graphene has been reported thus far. Among them, MoS_2, WS_2, SnS_2, FeS_2, and Ni_3S_2 have been recently utilized as sensing electrodes to determine various analytes.[194] Zhang *et al.* reported the use of a monolayer MoS_2 nanosheet as an electrochemical electrode for glucose detection. MoS_2 exhibited good redox activity and electrochemically reduced MoS_2 (r-MoS_2), providing efficient electron transport and better conductivity in different electrolytes, *e.g.*, [[Ru(NH$_3$)$_6$]$^{2+/3+}$ and Fe[(CN)$_6$]$^{3-/4-}$] redox system. The proposed sensor was employed to detect dopamine (DA) and showed good selectivity for DA in a mixture of uric acid and ascorbic acid as interfering agents.[195] Here, it is important to emphasize that pristine TMDC nanosheets do not often exhibit superior sensing properties due to their poor electrical conductivity. Thus, one of the approaches to increase their sensitivity is synthesizing hybrid nanosheets with rare-earth metal NPs (Au, Ag, Pt, and Pd). The synergistic effects between the surface of TMDCs and NPs can improve their electrocatalytic behavior and sensitivity compared with pure TMDC nanosheets.[194,196] Similarly, this can be applied to various 2D materials that lack the required electrical conductivity for sensitive and selective electrochemical sensing. The quest to develop state-of-the-art electrochemical sensing materials has also witnessed the application of MXenes as electrode materials for chemical signal transduction. Metal-like electrical conductivity, intrinsic surface terminations, redox-active sites, ample surface termination that allows copious mass loading, and large surface area enable the rapid transduction of chemical signals. Zhu *et al.* fabricated a hemoglobin (Hb)-immobilized mediator-free Ti_3C_2-MXene-based electrochemical sensor,[197] which showed excellent capability towards nitrite detection with an LOD as low as 0.12 μM and a wide linear range (0.5–1800 μM). Besides 2D inorganic materials, Zhang *et al.* described the application of 2D MOF nanosheet-based electrodes for H_2O_2 detection.[198] Using the Langmuir–Schafer method, 2D M-TCPP (Fe) nanosheets (M = Co, Cu, and Zn) were produced in the form of thin films on electrodes (Fig. 6a). It is important to mention that the electrode composed of Co-TCPP(Fe) nanosheet showed the best electrocatalytic activities among the structures, together with a low LOD of 0.15×10^6 M (Fig. 6b). Furthermore, the proposed electrochemical sensor could be used to real-time monitor H_2O_2 production by live cells (Fig. 6c). A 2D bimetallic organo-metal-framework was successfully synthesized with a bio-inspired design of organic ligands and metallic nodes and used as sophisticated 2D biomimetic nanomaterials (Fig. 6d).[198] More electrochemical sensors based on novel 2D materials are expected to be fabricated in the future. In addition, Table 4 presents the application of various 2D materials as efficient sensing platforms. However, despite the remarkable success of 2D material-based electrochemical sensors, they have certain limitations. Firstly, given that several 2D materials have been employed thus far, their poor electrical conductivity often results in a low detection limit. The growth of rare earth metal

NPs on the surfaces of 2D materials can enhance electrical conductivity and redox activity, resulting in improved sensing performances. Contrarily, the application of noble metal NPs is not cost-efficient and can increase the fabrication costs. In this case, modification of the crystalline phases is an alternative approach to address the poor electrical conductivity associated with 2D TMDC materials. For example, 1T phase TMDC metal nanosheets have higher electrical conductivity than 2H phase nanosheets, and thus a phase transformation can comprehensively overcome this limitation. A further shortcoming of electrochemical sensors that utilize 2D materials as electrode materials is their limited long-term stability, which needs to be carefully addressed.

3.3 Wearable sensors

In recent years, wearable electrochemical sensors have gained a lot of interest due to their ability to real-time human health monitoring. Several biomarkers in sweat can provide information to monitor the physiological health of an individual. Meng *et al.* reported the fabrication of an electrochemical sensor for real-time sweat analysis using a highly integrated sensing paper.[233] The device was fabricated by following a simple printing procedure, including highly integrating sensing paper with a hydrophobic protective wax and a conductive electrode array and incorporating MXene/methylene blue ($Ti_3C_2T_x$/MB) as the active material. For the fabrication of the sensor, an aqueous dispersion of $Ti_3C_2T_x$-MXene was drop-casted on screen-printed carbon electrodes followed by the immobilization of chitosan-contained glucose oxidase (GO_x) solution. The proposed sensor showed good sensitivity and selectivity towards the simultaneous determination of lactate and glucose with an LOD of 0.49 μA mM^{-1} and 4 nA μM^{-1}, respectively. $Ti_3C_2T_x$ exhibited excellent adsorption capability due to its large surface area and methylene blue modification synergistically increased the electrochemical response of the device.[234–236] The proposed highly integrated sensing paper-based sensor has enormous potential in wearable bioelectronic products and can be employed to develop innovative smart technologies. Recently, Lu *et al.* reported the fabrication of a flexible pressure sensor (MoS_2/CSilk) using vertically aligned MoS_2 nanosheets on carbonized silk (CSilk) fabric.[237] After a pyrolytic reaction, carbonized fibers with highly conductive sp^2 hybrid graphite structures were produced from the commercially available silk fiber. The MoS_2/CSilk hierarchical structure was obtained after a two-step solvothermal reaction. In the first step, for the *in situ* production of MoS_2 on the fibers, urea, MoO_3, and thioacetamide were added as precursors with a concentration of 0.3 g, 60 mg, and 70 mg, respectively, in a mixture of ethanol (25 mL) and deionized water (15 mL) and stirred vigorously for one hour. In the second step, the ultra-sonicated carbonized silk fiber was soaked in the above-mentioned mixture and the whole solution was hydrothermally treated for 24 h at 220 °C. The prepared MoS_2/CSilk fiber was repeatedly rinsed with water, and then ethanol and left overnight to dry at 60 °C.[237] The pressure sensor was made up of two MoS_2/CSilk thin films arranged face to face and packed using 3 M VHB 9469 (double-sided adhesive

This journal is © The Royal Society of Chemistry 2023

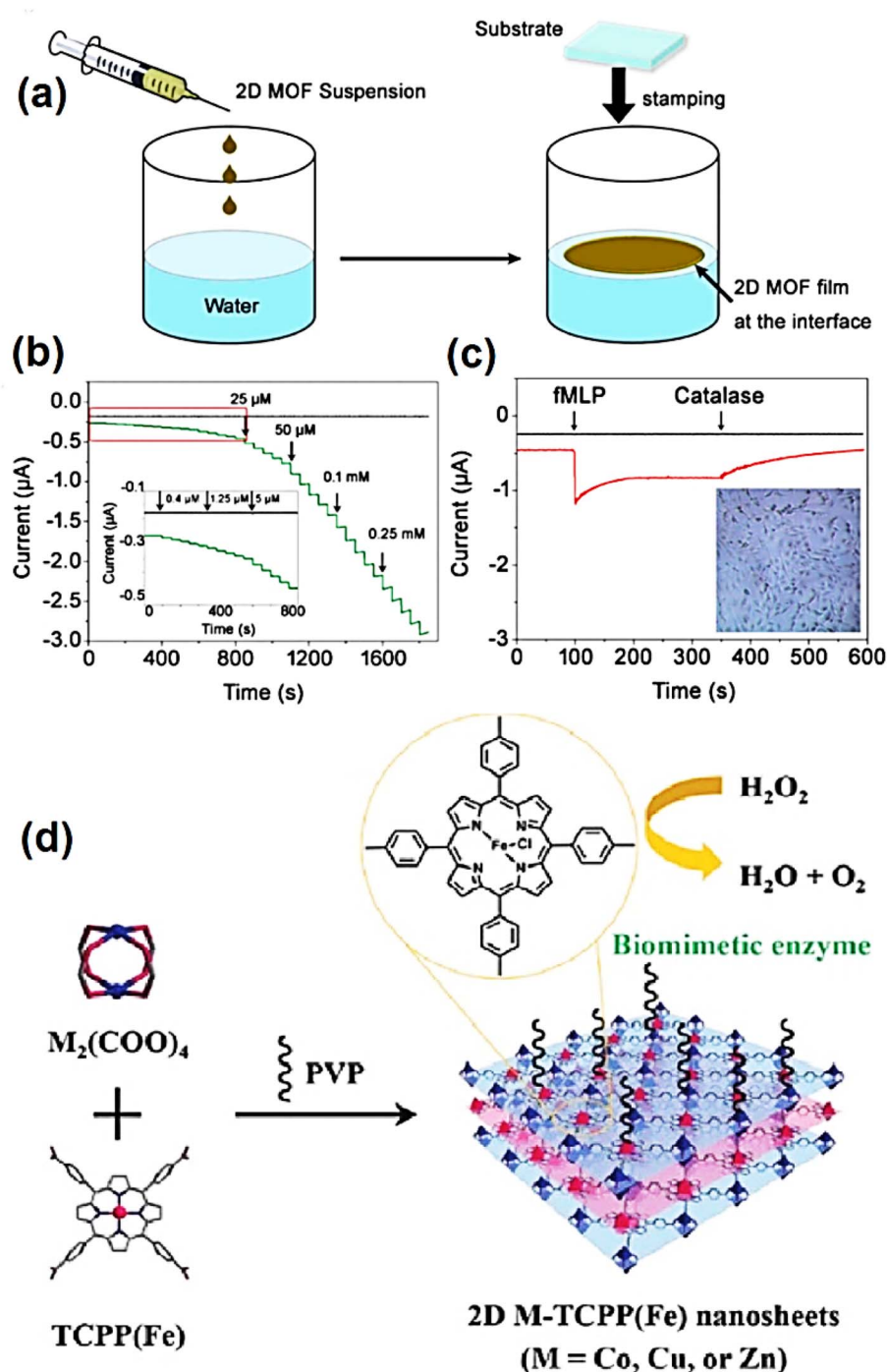*J. Mater. Chem. A*, 2023, **11**, 6016–6063 | **6027**

Fig. 6 (a) Illustration of 2D MOF nanosheet electrode growth *via* the assembly route, (b) amperometric (I–T) response of the electrodes composed of 2D Co-TCPP (Fe) nanosheet and pristine GCE with different H_2O_2 concentrations, and (c) I–T response of electrodes composed of 2D Co-TCPP (Fe) nanosheet with 300 U mL^{-1} catalase and 10 μM fMLP with (asymmetrical red curve) and without (linear black curve) MDA-MB-231 cells. (Inset corresponds to the micrograph of MDA cells using bright-field microscopy.) (d) Schematic of the bio-inspired design of metallic nodes and organic ligands. Adapted with permission from ref. 198 Copyright 2016, John Wiley & Sons.

tape model).[237] The contact area between the two MoS$_2$/CSilk thin films varied upon the application of pressure, resulting in variations in the contact resistance. Thus, the loading pressure could be determined by monitoring the variations in electrical signals (Fig. 7). This sensor can be combined with wearable systems or self-powered appliances. Owing to its exceptional performance, the pressure sensor composed of MoS$_2$/CSilk can be utilized for real-time physiology monitoring and possibly clinical diagnostics.

6028 | *J. Mater. Chem. A*, 2023, **11**, 6016–6063

This journal is © The Royal Society of Chemistry 2023

Table 4 Various 2D material-based electrochemical sensors

Material	Synthesis route	Sensing platform	Analyte	LOD	Linear range	Sensitivity	Ref.
MoS_2	Hydrothermal	AuNPs/MoS$_2$/graphene	NO$_2^-$	1.0 μM	5.0 μM to 5.0 mM	—	199
	Hydrothermal	MoS$_2$/TiO$_2$	TPT	9.8 nM	0.01–18.57 μM	—	200
	Hydrothermal	AuNps-MoS$_2$/graphene	Rutin	0.01–45.0 μmol L^{-1}	0.004 μmol L^{-1}	—	201
	Chemical exfoliation	MIP/MoS$_2$/NH$_2$-MWCNT@COF/GCE	Sulfamerazine	1.1×10^{-7} mol L^{-1}	—	—	202
	Chemical exfoliation	Ag nanoprism@MoS$_2$	TCAA	0.17 μM	0.5–10 μM & 10–80 μM	—	203
	—	MoS$_2$-AuPt	Pb^{2+} ions	38 fg mL^{-1}	0.1 pg mL^{-1} to 1000 ng mL^{-1}	—	204
WS_2	Chemical exfoliation	WS$_2$/CNTs	Isoniazid	0.24 μM	10–80 μM	—	205
	Li intercalation	WS$_2$-MIPs/GO-SWCNTs/GCE	Vitamin B$_2$	0.0007 μM	0.002–0.9 μM	12.539 μA μM^{-1}	206
	Hydrothermal and seed-mediated growth	Pt-Ag/WS$_2$	DA	0.2 μM	0.6 μM to 1 mM	348.8 μA mM^{-1} cm^{-2}	207
	Hydrothermal	WS$_2$/GdCoO$_3$	Quercetin	0.003 μM	0.001–329 μM	6.922 μA μM^{-1} cm^{-2}	208
	Sonochemical	MP-WS$_2$ NRs/SPCE	Clonazepam	2.37 nM	10–551 μM	24.32 μA μM^{-1} cm^{-2}	209
	Pyrolysis technique	g-C$_3$N$_4$/CuO	DA	1.00×10^{-10} mol L^{-1}	2.00×10^{-9} to 7.11×10^{-5} mol L^{-1}	0.316 μA cm^{-2} μmol L^{-1}	210
$g\text{-}C_3N_4$	Calcination	ZIF-8/g-C$_3$N$_4$/Co	D&C red 33 Patent Blue V	0.034 μM	0.08–10 μM to 10–900 μM	—	211
	Sol-Gel	g-C$_3$N$_4$	H$_2$O$_2$	26.48 μM	150 nM to 1.8 μM	27 μA cm^{-2} μM^{-1}	212
	—	C$_3$N$_4$ NTs/ionic liquid	Ractopamine	1.0×10^{-13} M	1.0×10^{-9} to 1.0×10^{-12} M	—	213
	Pyrolyzing thiourea	HP5@AuNPs@g-C$_3$N$_4$	PSA	0.12 pg mL^{-1}	0.0005–10.00 ng mL^{-1}	—	214
	Solvothermal	g-C$_3$N$_4$ and Ru@MOFs	Amyloid-β	3.9 fg mL^{-1}	10^{-5} to 500 ng mL^{-1}	—	215
	Sonochemical	g-C$_3$N$_4$/NiO	Quercetin	0.002 μM	0.010–250 μM	—	216
MOF	Hydrothermal	Au@Cu-MOF/N-GQDs/GCE	Patulin	0.0007 ng mL^{-1}	0.001–70.0 ng mL^{-1}	—	217
	Hydrothermal	Cu-MOF/rGO/CuO/α-MnO$_2$	Resorcinol	0.2 μM	0.2–22 μM	6262.6 mM cm^2	218
	Hydrothermal	NiO@Ni-MOF	Luteolin	3 pM	0.01–1 nM & 1 nM to 50 μM	—	219
	In situ preparation	Ni-MOF@CNTs hybrid	BPA	0.35 nM	1–1000 nM	284.64 μA μM^{-1} cm^{-2}	220
	Chemical exfoliation	Hemin@MOF	H$_2$O$_2$	0.07 μmol·L^{-1}	0.1–2200 μmol·L^{-1}	—	221
	Hydrothermal	GO/MOF	As(iii)	0.06 ppb	0.2–25 ppb	—	222
	Hydrothermal	SnS@Co N-C microrod	L-Tyrosine	3.1 nmol L^{-1}	0.01–250.0 μmol L^{-1}	—	223
	Electrospun	Mn MoO$_4$-MXene	Hydroquinone Catechol	0.26 nM / 0.30 nM	5–65 nM f	7.437 μA nM^{-1} cm^{-2}, 6.471 μA nM^{-1} cm^{-2}	224
MXenes	Hydrothermal	Fe-MOF/MXene	As(iii)	0.58 ngL^{-1}	10 ∼ 100 ngL^{-1}	8.94 μA/ng L^{-1} cm^{-2}	225
	HF etching and others	Ti$_3$C$_2$/G-MWCNTs/ZnO	DA	3.3 nM	0.01–30 μM	16 A/M	226
	HF etching	AuNPs@Ti$_3$C$_2$	5-Hydroxymethylcytosine	0.632 pM	0.632 to 63.2 pM	—	227
	LiF + HCL	Ti$_3$C$_2$@N-C	Cd^{2+} / Pb^{2+}	2.55 nM / 1.10 nM	0.1–4 μM / 0.05–2 μM	49.8500 μA nM^{-1} cm^{-2} / 177.3327 μA nM^{-1} cm^{-2}	228
	—	MIP/Cu-MOF/Ti$_3$C$_2$T$_x$/GCE	Hygromycin-B	1.92 nM	5 nM to 5 μM	—	229
	Electropolymerization	MIP/CNT/Cu$_2$O NPs/Ti$_3$C$_2$T$_x$	Diethylstilbestrol	6 nM	0.01–70 μM	—	230
	Wet precipitation	Ti$_3$C$_2$T$_x$-Cu$_2$O	Glucose	2.83 μM	0.01–30 mM	11.061 μA nM^{-1} cm^{-2}	231
		Ce-MOF/Ti$_3$C$_2$T$_x$	L-Tryptophan	0.19 μM	0.2–139 μM	0.1556 μA nM^{-1} cm^{-2}	232

Abbreviations: TPT = topotecan, TCAA = trichloroacetic acid, DA = dopamine, PSA = prostate-specific antigen, BPA = bisphenol A, As(iii) = arsenic(iii), MIP = molecularly imprinted polymers, and SPCE = screen-printed carbon electrode.

This journal is © The Royal Society of Chemistry 2023

J. Mater. Chem. A, 2023, **11**, 6016–6063 | **6029**

Further, Shin *et al.* proposed a sensor based on MoS_2 sandwiched between two Au-layers (Au/MoS_2/Au) on polyethylene terephthalate (PET) for the detection of HIV-1 surface proteins, *e.g.*, glycoprotein GP120.[238] The surface of HIV consists of non-covalently bonded envelope glycoproteins GP120 (gp120) and GP41 (gp41). Thus, the early detection of Gp120 is crucial given that it binds to the cluster and plays a significant role in HIV infection. To realize this type of biosensor, PET substrate was coated with Au monolayers through sputtering (Au/PET), and then MoS_2 NPs were spin-coated on the Au-coated PET substrate (MoS_2/Au/PET). In the final step, the substrate was again coated with Au *via* sputtering (Au/MoS_2/Au/PET).[238] GP120 antibody was immobilized on the electrode *via* the cysteamine-modified Au/MoS_2/Au surface. Spectroscopic analysis and SEM, AFM, and CV measurements were performed to confirm the fabrication of the sensor. Analyte detection was performed through square wave voltammetry, and the proposed flexible sensor showed great sensitivity and selectivity with an LOD of 0.1 pg mL^{-1}.[238] Wang *et al.* reported the fabrication of an electrochemical sweat platform based on freestanding graphene paper (GP) decorated with MoS_2 nanocrystal monolayers and submicron Cu-buds for the bifunctional detection of lactate and glucose.[239] The sensing electrode was fabricated *via* the sequential growth of 0D-MoS_2-nanocrystals on 2D freestanding GP employing the hydrothermal process, followed by the electrodeposition of 3D Cu submicron-buds. The GP ensured effective charge transfer towards the working electrode, while the triple component (Cu-MoS_2-GP) structure was coated with

lactate oxidase, which offered a favorable microenvironment for enzyme immobilization, and also facilitated the charge transfer. The fabricated electrodes (lactate oxidase-Cu-MoS_2-GP) exhibited bifunctional sensing with high electrocatalytic activity, long stability, and reproducibility. The proposed electrochemical sensor showed a broad linear range, with values varying in the range of 0.01–18.4 mM for lactate and 5–1775 μM for glucose, with detection limits of 0.1 μM and 500 nM. In contrast, the sensitivity for lactate and glucose was reported to be 83 mA cm^{-2} $μM^{-1}$ and 3.38 mA cm^{-2} $μM^{-1}$, respectively. Certainly, this sensor device fabricated by integrating 0D-transition metal sulfide, 2D-graphene, and 3D-transition metal can provide a new pathway to fabricate sensors to monitor glucose and lactate in sweat.[239] Wang *et al.* also proposed a non-enzymatic flexible MOF electrode-based sensor by effectively integrating self-assembled and oriented $Cu_3(btc)_2$ nanocubes with amino-functionalized free-standing GP ($Cu_3(btc)_2$-NH_2-GP).[240]

Compared to similar enzyme-based sensors for lactate and glucose monitoring in sweat, the proposed sensors provided a wide dynamic range (0.05 mM to 22.6 mM for lactate and 0.05–1775.5 μM for glucose) with a considerably low lactate oxidase (5 μM for lactate and 30 nM for glucose). However, it is essential to note that the proposed sensors exhibited greater sensitivity with a value of 0.029 mA cm^{-2} $μM^{-1}$ for lactate and 5.36 mA cm^{-2} $μM^{-1}$ for glucose, respectively.[239] This increase in sensitivity can be attributed to the proximity effect between the closely packed $Cu_3(btc)_2$ nanocubes and functionalized graphene nanosheets, resulting in conductive pathways. In addition, coupled with the
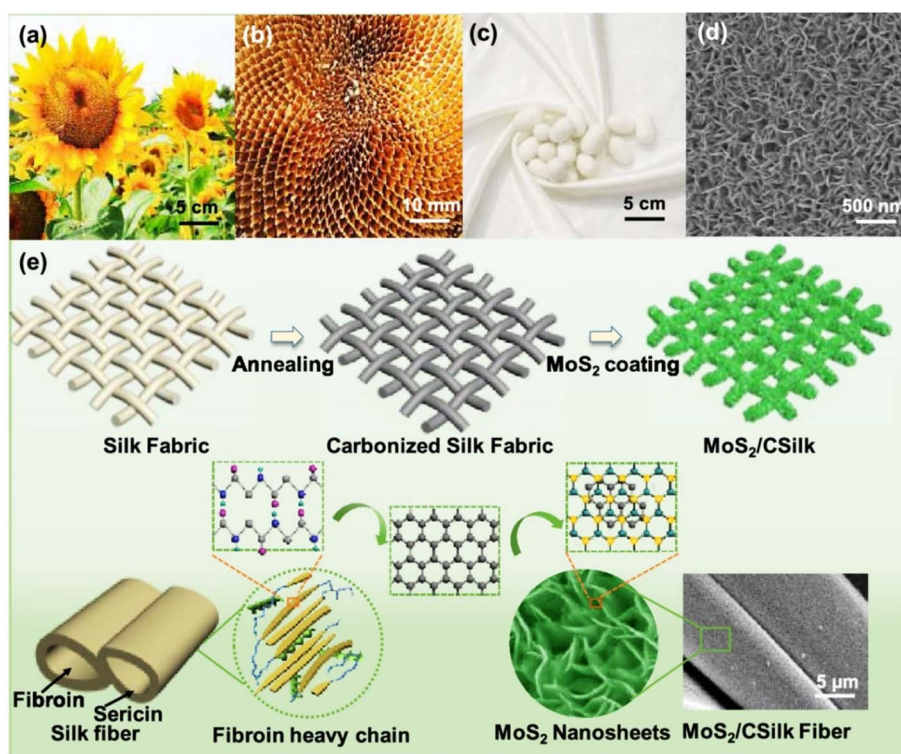

Fig. 7 Architecture, fabrication process, and structural variations of MoS_2/C Silk. (a and b) Digital photographs of a sunflower faceplate, (c) commercially available silk fabric, (d) SEM images of MoS_2/CSilk and (e) demonstration of synthesis strategy and structural alterations. Adapted with permission from ref. 237 Copyright 2020, the American Chemical Society.

6030 | *J. Mater. Chem. A*, 2023, **11**, 6016–6063

This journal is © The Royal Society of Chemistry 2023

ideal microenvironment created by graphene sheets, the small-size $Cu_3(btc)_2$ nanocubes enabled the effective transmission of ions towards the transducer by reducing the ion-diffusion length, thus increasing the overall electron transfer kinetics. For the electrochemical detection of glucose, another similar technique has been utilized in the case of a GO_x-immobilized polymer electrode (Kapton® polyimide film) with gold, MoS_2, and gold nanofilm ($Au/MoS_2/Au$-nanofilm).[241] This sensor was fabricated by coating the pre-treated polymer substrate with Au *via* the Au-sputtering technique, followed by the spin coating of MoS_2 NPs (MoS_2/Au-nanofilm). Subsequently, a layer of Au was coated again to fabricate $Au/MoS_2/Au$-nanofilm polymer electrodes. A chemical linker (6-MHA) was deposited utilizing Au–thiol binding feature to immobilize GO_x on the electrode surface ($GO_x/Au/MoS_2/Au$-nanofilm) (Fig. 8). Amperometric (I–T) measurements were performed for the quantitative determination of glucose, which showed an LOD of 10 nM with a linear range of 500 nM to 10 nM. The proposed sensors showed good selectivity towards glucose sensing in a mixture of uric acid and ascorbic acid as interfering agents. The synergistic effects imparted by Au and MoS_2 NPs caused enhanced electrocatalytic activity and increased flexibility could be derived from the polymer.

3.4 Electronic and optical sensors

3.4.1 Humidity sensing.
Humidity sensors can detect and track the amount of water vapor in the surrounding air.[242] These sensors are used widely in semiconductors, microelectronics fabrication, textiles, food inspection, meteorology, agriculture, environmental monitoring, biomedical research, and the pharmaceutical industry. The materials used to fabricate humidity sensors include metal oxides, polymers, hydrogels, NPs, and carbon nanotubes.[242,243] In recent years, researchers have devoted considerable effort to building humidity sensing devices based on graphene, TMDCs, and MXenes (see Table 5). Considering that they exhibit large surface-to-volume ratios, 2D

material-based sensors display excellent sensitivity toward humidity variations. A broad spectrum of sensing techniques, including electrical (resistance and capacitance), thermal conductivity, gravimetric response, and optical processes, are currently accessible for measuring humidity levels. However, the demand for humidity sensors based on optical techniques is mainly driven by their many benefits, *e.g.*, small size, light weight, low cost, the ability to identify moisture in real-time in unsafe situations, and remote monitoring capability.[244] Luo *et al.* reported the fabrication of a novel all-fiber-optic device based on 2D WS_2 material coated on a side-polished fiber (WS_2 CSPF) and utilized it as a susceptible and quick response humidity sensor, as shown in Fig. 9.[244] The two-step method for the fabrication of the sensors, as presented in Fig. 9a, involved the fabrication of side polished fiber (SPF) in the first step, and subsequent deposition of WS_2 on the polished area in the second step. Fig. 9b shows that the length of the polished area is 15 mm with a residual fiber thickness (RFT) of ~70 μm in the polished region. For the humidity sensing experiments, the temperature inside the chamber was adjusted to 25 °C, and the relative humidity (RH) inside the chamber was adjusted to complete a cycle (increasing from 35–85% RH and decreasing from 85–35% RH) with a gradual increment of 5% RH. Fig. 9c illustrates the relative optical output power of the WS_2CSPF sensor, which represents two prominent features, *i.e.*, the significant variation (~6 dB) and comparatively smooth laddering in the output optical power in the case of WS_2CSPF.

Furthermore, Fig. 9c and d demonstrate a comparison of the humidity response between the bare SPF and WS_2SPF humidity sensors. It is evident that the sensitivity of WS_2SPF (0.1213 dB/% RH for descending and 0.1056 dB/% RH for ascending) was 15-fold greater than that of the bare SPF (0.0051 dB/% RH for descending and 0.0070 dB/% RH for ascending). The fundamental method for humidity detection based on the WS_2CSPF optical sensor is as follows: whenever the chamber humidity increases, the concentration of H_2O molecules in the air also rises. Air molecules get physically adsorbed on the WS_2 surface,
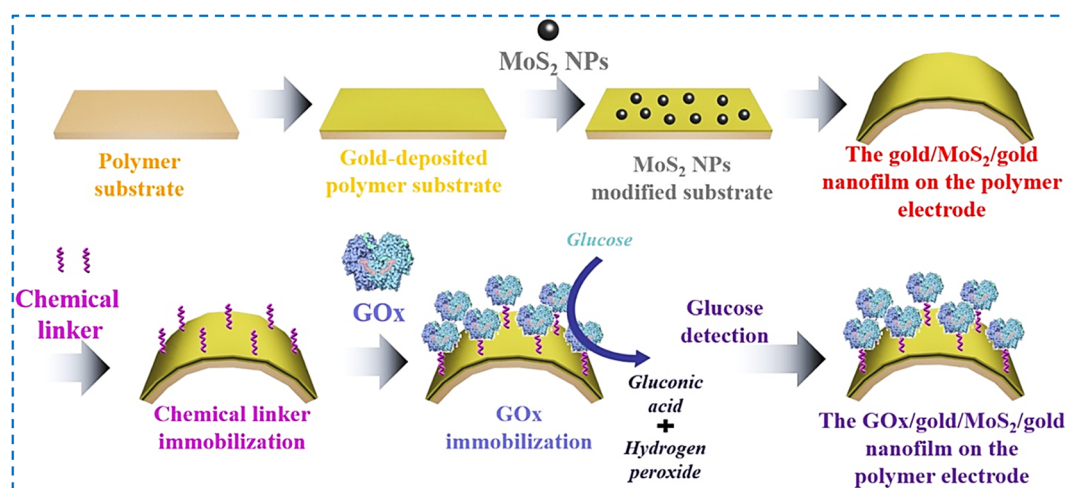

Fig. 8 Illustration of protocol for the fabrication of an electrochemical biosensor for glucose determination. Adapted with permission from ref. 241 Copyright 2019, Elsevier B.V.

This journal is © The Royal Society of Chemistry 2023

J. Mater. Chem. A, 2023, **11**, 6016–6063 | **6031**

Table 5 2D materials employed for fabrication of humidity sensing devices

Materials	Synthesis route	Sensing platform	Analyte	LOD	RH range	Sensing response/sensitivity	Ref.
MoS_2	Ultrasonicated exfoliation	MoS_2 NS	Soil moisture	—	11–96%	43 684%	247
	Probe assisted sonication	MoS_2 NS	NO_2	27 ppb	—	88% (~8 times)	248
	Ultrasonicated exfoliation	MoS_2 QDs@NMP	Humidity	—	10–95%	2.21 MΩ/% RH	249
	Ultrasonicated exfoliation	MoS_2 QDs	Humidity	—	10–95%	2.78 MΩ/% RH	
	Hydrothermal	SnO_2@MoS_2 NS	NH_3	—	—	2083%/200 ppm	250
	Hydrothermal	SVE MoS_2	NO_2	0.1 ppb	—	226% to 200 ppb	251
	Commercial MoS_2 dispersion	MoS_2/Nafion/QCM	Humidity	—	11.3–97.3%	138.1 Hz/% RH	252
	Hydrothermal	Cu_2O/MoS_2 NS	NH_3	—	—	~872%/100 ppm	253
	Liquid phase exfoliation	MoS_2	Formic acid	50 ppm	—	0.114 pm/ppm	254
	Mechanical exfoliation	FL MoS_2	NO_2	5 ppm	—	4.4 s/5 ppm	255
	Ultra-sonication	MoS_2	NH_3	—	—	15.2%	256
		PMMA-MoS_2	NH_3	500 ppm	—	54%	256
	Liquid phase exfoliation	MoS_2-PEO	Humidity	10% RH	10% RH 70% RH	~25% at 10% RH	257
	Liquid phase exfoliation	MoS_2/ZnO	NO_2	5 ppm	—	3050%/5 ppm	258
WS_2	Probe sonication	ZnO NRs/WS_2 NS	Humidity	—	18–85%	101.71 fF/% RH	259
	Wet chemical	WS_2 NS	Humidity	—	25–75%	44.3%/RH%	260
	Wet chemical	Au@WS_2 NS	Humidity	—	55–75%	3007.9%/RH%	260
	Exfoliation	WS_2 NS	Humidity	—	30–70%	50%/RH%	261
	Sulfurization	WS_2 NS	NO_2	0.5 ppm	—	NO_2 41%/0.5 ppm	262
	Precipitation	Au-SNO_2@WS_2 NS	CO	50 ppm	—	3.687%/50 ppm	170
	Hydrothermal	WS_2-modified SNO_2 hybrid	Humidity	—	11–95%		263
MXene	LiF + HCl	MXene NS/QCM	Humidity	1.2% RH	1–16% RH	12.8 Hz/% RH	264
	LbL assembly	MXene/PEI-ML	Humidity	—	10–70% RH	—	265
	Etching/Mixing	rGO/N-$Ti_3C_2T_x$/PEI	CO_2	8 ppm	<62%	—	266

Abbreviations: NS = nanosheets, NH = nanohybrid, ML = multilayers, FL = few layers, QDs = quantum dots, SVE = sulfur-vacancy-enriched, QCM = quartz crystal microbalance, NMP = N-methyl-pyrrolidone, PEI = polyethyleneimine, PMMA = polymethyl-methacrylate, PEO = polyethylene oxide, PE = polyelectrolyte, and LbL = layer-by-layer.
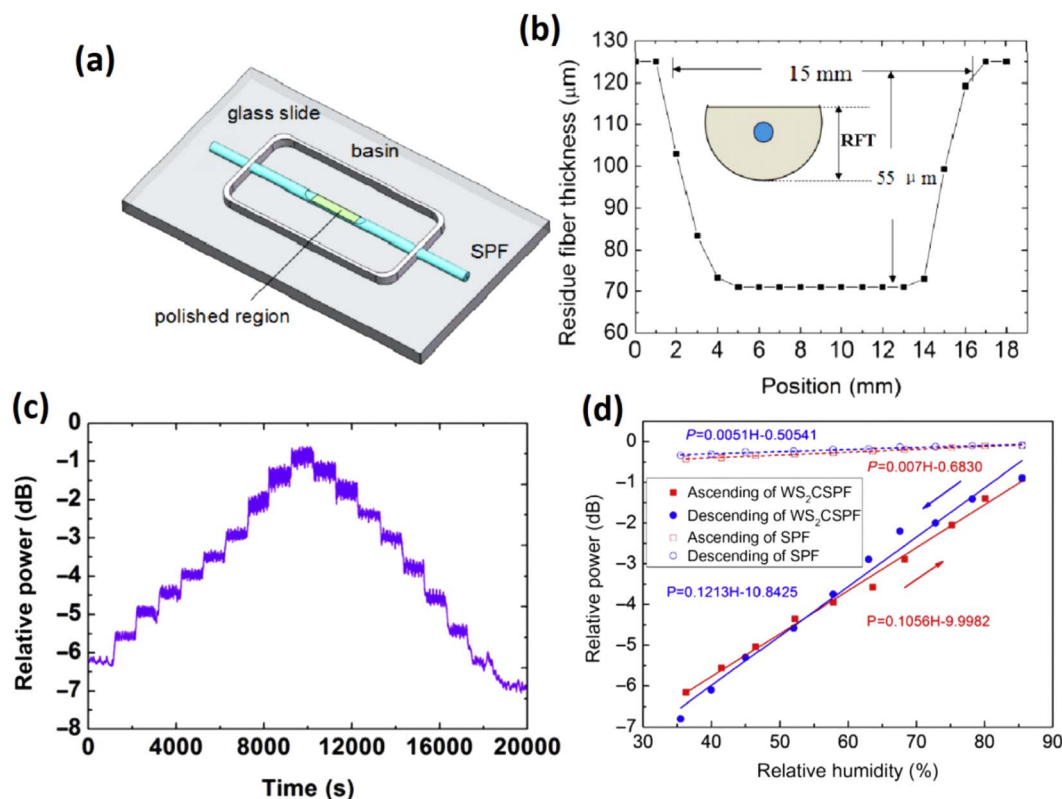

Fig. 9 (a) Illustration of experimental arrangement to fabricate WS_2 CSPF sensor for humidity sensing, (b) length of the polished area (15 mm) with RFT of ~70 μm in the polished region, (c) trend of relative power as a function of time through WS_2CSPF, and (d) comparison between relative power of WS_2CSPF and SPF in comparison with RH. Adapted with permission from ref. 244 Copyright 2016, Optica Publishing Group.

6032 | J. Mater. Chem. A, 2023, **11**, 6016–6063

This journal is © The Royal Society of Chemistry 2023

which leads to a small amount of charge transfer from WS_2 to H_2O. Following the orbital mixing theory,[245] the conductivity drops because of the reduction in conducting electrons following a rise in humidity, resulting in a decrease in light absorption. In this case, the transmitted optical output power of an SPF coated with WS_2 film increases, followed by a decrease in the transmitted loss of the SPF.

The 2D WS_2 coating significantly increased the sensitivity and stability of the optical SPF humidity sensing device. Consequently, the application of WS_2 increased the stability and sensitivity of the proposed humidity sensor with a significant figure of merit. The proposed sensors showed (i) an optical power output variation of ~ 6 dB in 35–85% RH, sensitivity values of (ii) 0.1056 dB/% RH for ascending humidity, (iii) 0.1213 dB/% RH for descending humidity, (iv) humidity resolution of 0.475% RH and (v) fast response speed of 0.13% RH per s. Moreover, this sensor showed a linear response with correlation coefficients of 98.27% (descending) and 99.39% (ascending) with good repeatability in the range of 35–85% RH. In contrast, the $MoSe_2$-coated SPF showed better sensitivity (0.321 dB/% RH) in a broader working RH range of 32% RH to 73% RH. Furthermore, the proposed $MoSe_2$CSPF sensor demonstrated a fast response time of 1 s and recovery time of 4 s, thus making it suitable for monitoring human breath.[246]

3.4.2 Heavy metal ion sensing. Heavy metals are a broad class of metallic chemical elements with an extremely high density, which are considered toxic and carcinogenic, including mercury, arsenic, thallium, chromium, cadmium, and lead. Heavy metals are found in large concentrations in the environment and used in industrial processes. They are natural elements in the Earth's crust and cannot be removed or degraded. These components may enter our bodies mainly through the air, water, and/or food. A high concentration of these heavy metals (*e.g.*, lead) in drinking water can produce harmful biochemical reactions in humans, causing various acute and chronic effects. These effects include kidney dysfunction, increased risk of heart disease and stroke, nervous system disorders, gastrointestinal tract infection, skin lesions, joint pain and fatigue, immune system dysfunction, and reproductive disorders.[267,268] Additionally, they may disrupt cellular processes, such as hemoglobin formation, causing severe health risks. According to the World Health Organization, the allowed limit of lead particles in drinking water is 10 ppb, where concentrations exceeding this level will be detrimental to human health. Consequently, the detection of the presence of heavy metal ions in drinking water is crucial. Liu *et al.* reported the fabrication of a tilted fiber grating (TFG) optical sensor (BP-TFG) integrated with 2D black phosphorus for the detection of Pb ions, which showed an LOD of 0.25 ppb.[269]

Concerning the stability of black phosphorus, currently more work is required to scale up the top-down processing of bulk black phosphorus crystals to produce few-layer black phosphorus, which is a typical fabrication method. Given that various 2D materials can be exfoliated by liquid-phase exfoliation,[54] Brent *et al.* developed a technique to produce few-layer flakes by exfoliating bulk phosphorus in *N*-methyl-2-

pyrrolidone (NMP) as an exfoliating medium under bath ultra-sonication.[270] Subsequently, large-scale exfoliation into sheets or even quantum dots that can be evenly dispersed in the solvent is possible. However, this approach is limited by the intrinsic limitation of phosphorene being stable in ordinary solvents, including water. Among the phosphorus allotropes, although bulk black phosphorus is the most stable, it rapidly reacts with oxygen and moisture when it is exfoliated into layers, disrupting its crystal structure.[271] Thus, the primary disadvantage of black phosphorus is its instability, which prevents its use in practical applications. Various methods can produce layered samples of varying sizes and properties, which can be utilized for multiple purposes.[272,273] In some studies, it has been suggested that ionic liquids can be used to exfoliate phosphorene at or slightly above room temperature. In addition to their flexibility and stability, ionic liquids are highly stable to heat, exhibit ionic solid conductivity, and have high solubility in water.[272] To improve the stability of nanosheets, Abellan *et al.* used 7,7,8,8-tetracyano-*p*-quinodi-methane and perylene bisi-mide.[274] Zhao *et al.* examined the stability of phosphorene using titanium sulfonate ligands (TiL_4) to generate TiL_4BP.[275] As a result of the P-Ti coordination, which occupies the lone-pair electrons of phosphorus, XPS, Raman spectroscopy, absorption spectroscopy, and photothermal performance measurements showed that the TiL_4@BP nanosheets exhibit good stability when dispersed in water and exposed to air for an extended period. In addition to increasing the stability of black phosphorus, surface passivation approaches also introduce defects to some extent. Also, by employing the epitaxial vdW growth approach, Lui *et al.* improved the stability of nanosheets by depositing dioctylbenzothienobenzothiophene thin films.[276] In 2018, Wu *et al.* successfully developed a surface lanthanide coordination method to improve the stability of nanosheets and quantum dots and introduced new activities.[277] Lastly, we discuss the various chemical modification methods that can be used to enhance the stability of low-layer phosphorene, including molecular modification and ion modification.

The experimental setup designed for the proposed sensor consisted of a broadband light source with transverse magnetic polarized resonances directed at the sensor and an optical signal analyzer to analyze the output signal (Fig. 10a).[269] The solutions containing varying concentrations of Pb^{2+} (ranging from $0.1–1.5 \times 10^7$ ppb) were used. To perform sensing measurement, BP-TFG was submerged in the Pb^{2+}-containing solutions for 120 s, followed by pipetting out the solution, and subsequent exposure to air for 180 s. An optical signal analyzer was used to obtain the transmission spectra for Pb^{2+} concentrations. The sensors were carefully cleaned with ethanol to remove the deposited Pb^{2+} ions before using the optical sensor for each successive measurement (at different concentrations). The shift in transmission spectrum at different Pb^{2+} concentrations is presented in Fig. 10b. As the concentration of Pb^{2+} ions increased, it is evident that the intensity of the transmission peak decreased and the wavelength was red-shifted, indicating the significant optical absorption of Pb^{2+} ions and variations in the effective refractive index of the cladding. Fig. 10c depicts the variation in the transmission intensity of

This journal is © The Royal Society of Chemistry 2023

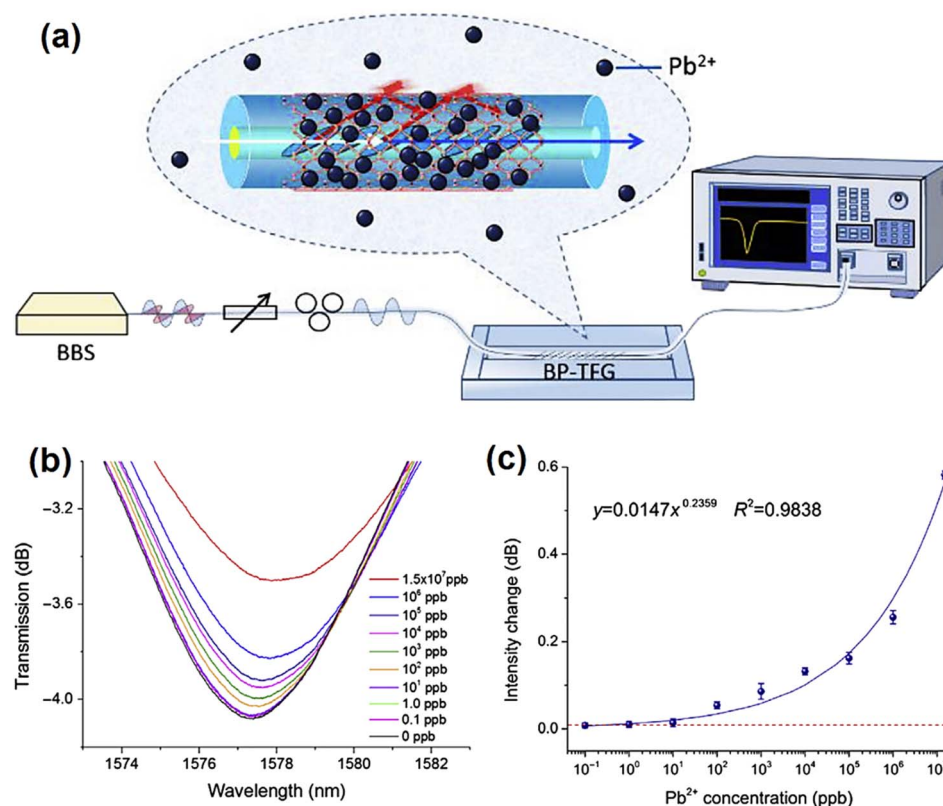*J. Mater. Chem. A*, 2023, **11**, 6016–6063 | **6033**

Fig. 10 (a) Demonstration of the experimental arrangement for the detection of heavy metals, (b) transmission spectra of BP-TFG, showing a strong upshift with an increase in the concentration of Pb^{2+} ions, and (c) display of resonant intensity change *versus* Pb^{2+} concentration. Adapted with permission from ref. 269 Copyright 2018, Elsevier B.V.

the sensor with different concentrations of Pb^{2+}, which reveals a nonlinear relation. These findings demonstrate that the BP-TFG optical sensor has the potential to detect Pb^{2+} at ultrasensitive levels over an extensive concentration range (0.1 ppb to 1.5×10^7 ppb; 4-fold better than BP-FET sensors for lead sensing[278]) and a low LOD of 0.25 ppb with greater sensitivity than electrically-based lead sensors (with 4-fold improved performance compared to carbon nanotube-based heavy metal ions sensors[279]).

3.4.3 Various electronic sensors. In chemiresistors or FET devices, the interactions between the target analytes and channels change the resistance of the channel material.[60] In classic FET-based devices, a semiconducting channel is present between the drain and source electrodes, whose conductivity can be controlled by changing the gate-to-source voltage. Chemiresistors have a simpler device structure than FETs, with a channel sandwiched between two electrodes (without a gate electrode). When the channel material is exposed to foreign species, their interaction changes the conductance of FETs and/or chemiresistors, thus making them attractive platforms for sensing applications.[60] In electronic sensors, two primary sensing mechanisms are used, namely electrostatic gating and doping. Both processes may contribute to the sensing impact in real-world applications when combined with additional complex mechanisms.[60] During the detection mechanism, 2D materials, particularly atomic-thick single-layer effectively

expose their surface to the analytes. This is promising in multiple perspectives (*e.g.*, sensitivity), which is impossible with nanomaterials and/or their parent or bulk counterparts. Graphene and its variants have evolved as the most commonly utilized channel materials among the 2D materials for electrical sensing. However, considering that Zhang and co-workers previously reviewed graphene-based electronic sensors,[60] herein, we emphasize the utilization of other 2D materials besides graphene to fabricate devices for various sensing applications.

In the past few years, several 2D materials, including TMDCs, black phosphorus, and metal oxides, have been developed and utilized as channel materials to fabricate electrical sensors for the detection of various analytes. Accordingly, Zhang and colleagues presented the application of mechanically exfoliated MoS_2 nanosheets as a channel material for the fabrication of FET devices for the detection of nitric oxide (NO).[280] The absorption of NO on the n-type MoS_2 surface resulting from p-type doping of the channel led to a decrease in current. The FET sensors based on multilayer MoS_2 demonstrated a steady response compared to the unstable single-layer MoS_2-based FET sensors and showed a detection limit of 0.8 ppm. Besides mechanically exfoliated MoS_2, Zhang and colleagues demonstrated that MoS_2 nanosheets exfoliated *via* Li intercalation-assisted method (solution-dispersed exfoliation technique) can be utilized as a channel for electronic sensors.[165] The NO detection chemiresistor based

6034 | *J. Mater. Chem. A*, 2023, **11**, 6016–6063

This journal is © The Royal Society of Chemistry 2023

on thin films of exfoliated MoS_2 nanosheets showed an LOD of 190 ppt (parts per trillion).

Moreover, flexible NO_2 gas sensors can also be fabricated by coating thin films of MoS_2 nanosheets on flexible PET substrates, while rGO thin films can be utilized as flexible electrodes. Decorating the surface of the MoS_2 thin films with Pt-NPs increased the sensitivity of the device and resulted in a lower LOD of 2 ppb toward NO_2 detection. Jian Zhen et al. described a sensor for NO_2 detection based on SnS_2 flakes.[281] The excellent selectivity of the proposed sensor towards NO_2 arises from the robust affinity, appropriate position of partially occupied NO_2 molecular orbitals, and Fermi-level of SnS_2. This novel method can pave the way for the development of ultra-sensitive and selective sensors for gas molecules based on 2D materials. Currently, various gas sensors have been developed using many 2D materials, including WS_2,[282,283] $MoSe_2$,[284] black phosphorus,[285,286] WO_3,[287] ZnO,[288,289] and NiO.[290]

Besides gas detection, MoS_2-based sensors have also been developed to detect bio-analytes. Sarkar et al.[291] reported the

fabrication of MoS_2-based biosensors, as presented in Fig. 11a and b. The device was fabricated on an SiO_2/Si substrate (270 nm) with Ti/Au (60 nm/100 nm) as the metal contacts of the source and drain and the high-k dielectric (30–35 nm) HfO_2 as the gate (Fig. 11d). In this method, the MoS_2 flakes were obtained via a micromechanical exfoliation scheme (Fig. 11c); hence, the scalable synthesis of MoS_2 can enable the scalable production of the proposed biosensing devices.

Previous studies indicated that the direct contact of metal electrodes (source/drain) with electrolyte initiates the adsorption of biomolecules on electrodes, resulting in variations in work function of the metal and the contact resistance. In the study described above, a dielectric layer was used to passivate the source and drain contacts, overcoming the challenges faced in the previous study. The fabrication of fluidic channels for the storage of electrolytes was carried out via an acrylic sheet. For this purpose, an Ag/AgCl reference electrode (i.e., electrolyte gate) was utilized to apply a bias to the electrolyte, which is an
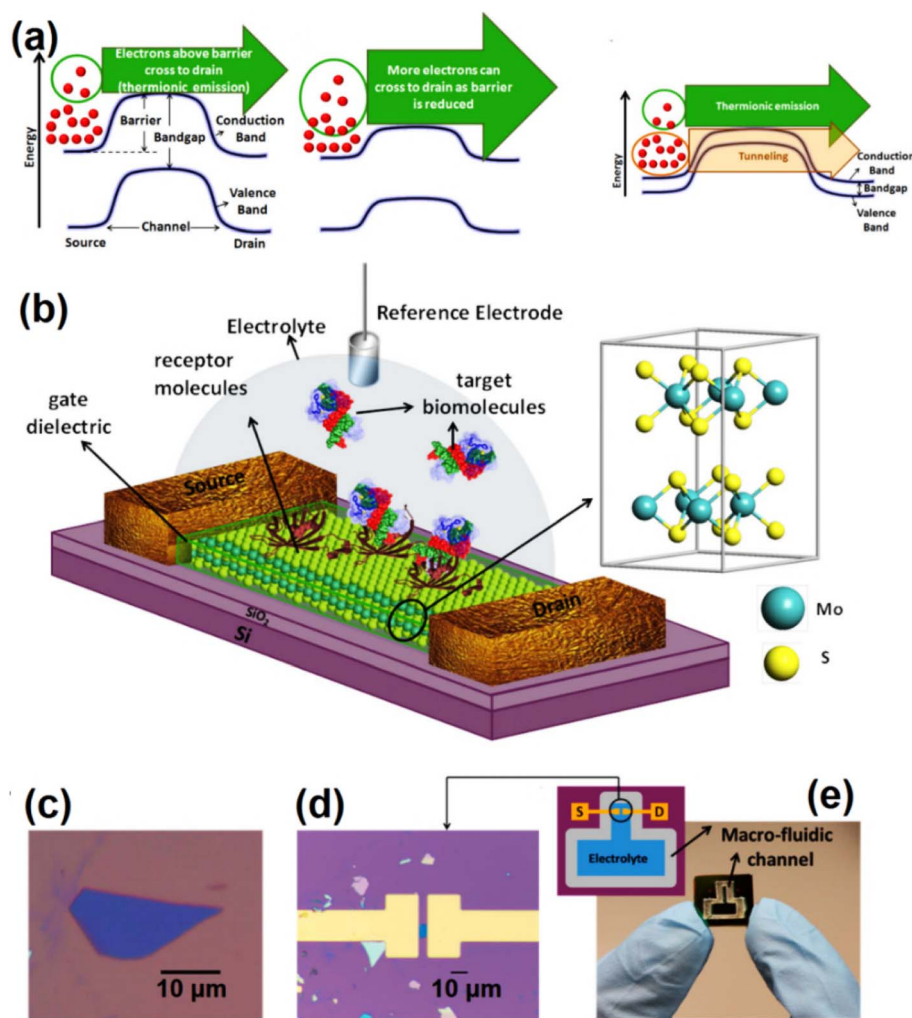

Fig. 11 (a) Illustration of bandgap effects of graphene FET biosensor, (b) illustration of FET biosensors based on MoS_2, (c) optical micrograph of MoS_2 flake on SiO_2/Si substrate and (d) optical micrograph for FET biosensor based on MoS_2. (e) Image of a developed chip (inset represents its scheme). Adapted with permission from ref. 291 Copyright 2014, the American Chemical Society.

essential factor in monitoring the working regime and achieving the stable operation of biosensors.[291]

Compared to graphene-based biosensors, semiconductor FETs work as a channel, where only electrons that possess energy greater than the source-to-channel barrier can pass from the source to drain (Fig. 11a). Therefore, lowering the barrier potential results in the larger movement of electrons to the drain. At the source, the energy occupied by the electronic levels is accessed by the Boltzmann distribution, and a final lower surface area is acquired at room temperature (60 mV dec^{-1}). The small bandgap energy of the semiconducting material provides a considerably thin barrier, where the movement of electrons *via* direct tunneling can be attained even for low-energy electrons compared to barrier height (Fig. 11a).[291] The FET sensor described above demonstrated outstanding sensitivity to both pH readings and biomolecule detection. In addition, MoS_2-based FET detection devices can detect prostate-specific antigens, a potential biomarker for cancer.[292,293] Moreover, the synthesis of new 2D materials is on an upward trajectory.[194] Thus, it can be anticipated that additional electronic sensor devices can be constructed soon by exploiting novel 2D materials as channel materials to detect more target analytes. However, it is worth noting that although significant sensitivities have been achieved by utilizing 2D materials, they still have drawbacks. The low selectivity for specific target analytes arises from their great sensitivity to exogenous stimuli. In this case, altering the surface of channel 2D materials or sieving a thin layer covering has been mainly implemented to overcome this challenge. Specifically, due to their capacity to filter various gas molecules, which is selectively facilitated by their precise pore widths, MOFs are broadly employed as useful materials in gas separation.

Consequently, without compromising their sensitivity, it is expected that the sensitivity of FET sensors towards gas molecules can be improved significantly by depositing a thin MOF layer on the channel 2D material. The MOF layer can selectively sieve gas molecules with a diameter less than its pore size. A further method to increase the selectivity is modifying the surface of the channel with specific functional groups that enhance the interaction between the channel materials and the analyte, thus increasing the selectivity. Due to the surface oxidation and moisture absorption by these materials, electronic sensor devices based on 2D materials face drawbacks in terms of their short-term stabilities. Thus, to resolve this limitation, covering the channel with a stable thin layer material (*e.g.*, metal oxides and polymers) has been proposed to shield the 2D materials from ambient conditions, resulting in increased stabilities.

3.4.4 Fluorescent sensors. The fluorescence responses or the increase or decrease in the fluorescent signals due to the interactions between the target analyte and the fluorescent probes determine the detection capability of fluorescent sensors. The majority of existing 2D materials, including graphene and its derivates, TMDC, h-BN, and layered double hydroxides, emit little or no fluorescence, making them ineffective as fluorescent probes for applications in sensing. However, these 2D materials work well as fluorescent dye quenchers. In particular, they have a higher quenching efficiency than other morphologies or their bulk equivalents due to their wide effective surface area and ultra-low dimension, offering a broader contact area to achieve close contact with the dye molecules. Owing to their notable potential to quench fluorescent signals and good selectivity, atomically thin 2D materials such as MOFs, graphene and its derivatives, TMDCs, and MXenes are extensively employed to fabricate "turn-on" fluorescent probes for the ultra-sensitive sensitive detection of a variety of analytes (Table 6). For example, Yang and colleagues developed GO-based fluorescence sensing probes to detect biomolecules such as DNA and proteins.[294] Subsequently, the dye-labeled single-stranded DNA (ssDNA) was bonded to the GO surface by mixing it with water-soluble GO nanosheets. Non-covalent bonding of the dye-labeled ssDNA with GO nanosheet resulted in the quenching of its fluorescent signal. Subsequently, the target DNA, when immobilized, attracted ssDNA due to its high affinity with the labeled ssDNA. This hybridization dissociated the dye-labeled ssDNA from the GO nanosheet, hence restoring the fluorescence of the dye molecules. The fluorescence enhancement technique can also be used to quantify specific DNA. This design is focused on probe liberation as a result of target hybridization, and the resultant fluorescent sensor shows higher selectivity and sensitivity. An analogous approach was utilized to realize a fluorescent protein sensor with a low LOD of 2 nM, which exhibited high selectivity.

However, Shijiang *et al.* significantly modified the architecture of GO-based fluorescence sensors.[295] Considering the ability of GO to differentiate ssDNA and dsDNA, dye-labeled ssDNA-hybridized GO sheets were immobilized with target DNA. Compared to previous studies, the sensor showed great selectivity and sensitivity for the detection of DNA with an LOD of 100 pM. This work also demonstrated the feasibility of the multiplex detection of DNA against different DNA targets as interfering agents. Subsequently, fluorescence sensors were developed using GO nanosheets as a detection platform to detect a variety of analytes, such as proteins, small molecules, nucleic acids, and metallic ions, with enhanced selectivity and sensitivity.[296,297] Due to the exceptional performance of GO-based fluorescence sensors and based on the ability of MoS_2 to distinguish ssDNA and dsDNA (double-stranded DNA), sensors were fabricated based on various fundamental ideas similar to that presented by Fan and coworkers.[295] The resulting sensor demonstrated excellent DNA detection selectivity and sensitivity with an LOD as low as 500 pM (Fig. 12).[25] Subsequently, Zhang and colleagues published a comprehensive review and compared monolayer MoS_2, TaS_2, and TiS_2 fluorescence sensing platforms for DNA recognition.[298] They showed that under similar conditions, TaS_2-based sensors have better performance with enhanced sensitivity and lower LOD (0.05 nM) compared to that composed of MoS_2 (0.1 nM) and TiS_2 (0.2 nM). In addition, a monolayer-based TaS_2 fluorescence sensor has been proposed for the multiplex detection of DNA.

Furthermore, many fluorescent sensors have been produced based on extremely thin 2D materials, including MoS_2,[299,300] WS_2,[301,302] Ta_2NiS_5,[303] $g-C_3N_4$,[304,305] and MnO[53,306] for targeted and accurate detection towards a range of target species, *e.g.*,

6036 | *J. Mater. Chem. A*, 2023, **11**, 6016–6063

This journal is © The Royal Society of Chemistry 2023

Table 6 2D material-based fluorescent sensors

Material	Synthesis route	Sensing platform	Function	Analyte	LOD	Linear range	Ref.
MoS_2	Hydrothermal	Apt-modified QDs & MoS_2	NSs as an energy acceptor	DA	45 pM	0.1–1000 nM	319
	Hydrothermal	MoS_2 MS/DNA/Si-Dot NA	FRET acceptor	Hg^{2+}	0.86 nM	Up to 1000 nM	320
	Hydrothermal	MoS_2 quantum dots	Fluorescent probe	Pb^{2+}	50 μM	33 μM to 8.0 mM	321
	Hydrothermal	MoS_2 QDs	Fluorescent probe	Fe^{3+}	0.4 μmol L^{-1}	5–50 μmol L^{-1}	322
	Hydrothermal	MoS_2 NS/DNA	Fluorescent probe	Aβ-o	3.1 nM	0.01–20 μM	323
	Hydrothermal	MoS_2/COOH	Fluorescent probe	Co^{2+}	54.5 nM	Up to 1 μM	324
		MoS_2/NH_2		Cd^{2+}	99.6 nM	Up to 500 nM	
		MoS_2/SH QDs		Pb^{2+}	0.84 nM	Up to 10 nM	
	Hydrothermal	MoS_2 QDs	Fluorescent probe	FOX-7	0.19 μM	0.5–100 μM	325
	Solvothermal	MoS_2 NS	DNA tagged MoS_2 NS	miRNA-210	0.3 fM	1 fM to 100 pM	326
	Li-intercalation	2D-MoS_2-GFP	Bioreceptor and quencher	Proteins	1 nM	0.5–50 nM	327
	Liquid phase exfoliation	CQDs/MoS_2	Fluorescent probe	Bisphenol S	2 nM	0.05–2 μM	328
	ULS Li-intercalation	MoS_2@PDA-PEG-peptide	MoS_2 NS as acceptor	Saspase-3	0.33 ng mL^{-1}	2–360 ng mL^{-1}	329
	—	QD-MB@MoS_2	Fluorescent probe	miRNA-155	7.19 fM	1 nm to 10 fm	330
				miRNA-150	5.84 fM		
	—	MoS_2 NS	MoS_2 – fluorescent quencher (FAM-CS) – fluorescent probe	AFM_1	0.5 nM	0.7–10 nM	331
WS_2	Hydrothermal	WS_2 QDs	"Turn-on" fluorescent sensor	LA	0.59 μM	1–10 μM	332
	Hydrothermal	Blue fluorescent WS_2-QDs	Stable fluorescence	Fe^{3+}	1.32 μM	0–55 nM	333
	—	WS_2-Pt-Fe_2O_3	Strong adsorption / Encapsulation of micromotors	Lipopolysaccharide	0.12 nM	4–1 000 000 ng mL^{-1}	334
	—	WS_2 NS	Fluorescent probe	Hg^{2+}	0.1 nM	0.5–20 nM	335
	—	WS_2 NS	Fluorescence probe	Hg^{2+}	3.3 nm	5–500.0 nM	336
				Ag^+	1.2 nM		
Graphene	Hydrothermal	S,N-GQDs	Photostability	AA	1.2 μM	10–500 μM	337
	Hydrothermal	N-GQDs	Photostability	Hg^{2+}	23 nM	0–4.31 μM	338
	—	N-GQDs/Hg^{2+}	Tuneable luminescence	Paraquat	19 μg L^{-1}	0.05–2.0 μg mL^{-1}	339
	Hydrothermal	B, N-GQDs	Photostability	Hg^{2+}	6.4 nM	0.2–1 μM	
MXenes	Hydrothermal	N-doped Ti_3C_2 QDs	Enhanced fluorescence of MQDs	Fe^{3+}	0.17 μM	0.5–500 μM	340
				Cu^{2+}	0.15 μM		
	Hydrothermal	Ti_3C_2 NS	Up-conversion luminescence of Ti_3C_2	L-Tryptophan	91 nM	0–5 μM	341
	Solvothermal	N-Ti_3C_2 MQDs	Fluorescent probe	Cr(vi)	0.012–0.02 μM	0.1–500.0 μM	342
				AA			
	Hydrothermal	N,B-Ti_3C_2 MQDs	Wavelength-dependent blue PL	TC	20 nM	—	343
	Hydrothermal	N-Ti_3C_2 MQDs	Fluorescent probe	Glutathione	0.17 μM	0.5–100 μM	344
	Microwave-assisted	N,P-Ti_3C_2 MQDs	Fluorescent probe	NO_2^{-}	0.71 μM	0–80 μM	345
	Hydrothermal	N-doped Ta_4C_3 MQDs	Fluorescent probe	Fe^{3+}	2 μmol L^{-1}	—	346
	Hydrothermal	Ti_3C_2 MQDs	Fluorescent probe	Fe^{3+}	1.4 μM	1.4 μM to 0.8 mM	347

Abbreviations: ULS = ultra sonication, NS = nano sheets, NA = nano assembly, MQDs = MXene quantum dots, GQDs = graphene quantum dots, CQDs = carbon quantum dots PEG = polyethylene glycol, PDA = polydopamine, QD-MB = quantum dot-molecular beacon, Aβ-o = amyloid-β oligomers, FOX-7 = 1,1-diamino-2,2-dinitroethylene, LA = lipoic acid, GFP = green fluorescent protein, GFP = green fluorescent protein, TC = tetracycline, and AA = ascorbic Acid.

This journal is © The Royal Society of Chemistry 2023

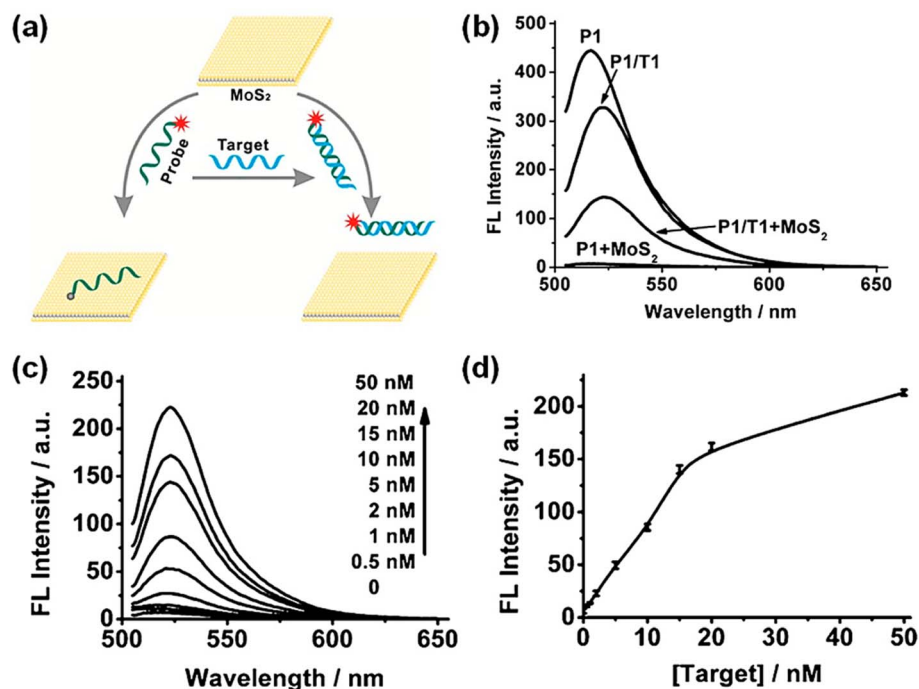*J. Mater. Chem. A*, 2023, **11**, 6016–6063 | **6037**

Fig. 12 (a) Graphical illustration of fluorescent DNA sensor based on MoS_2 (single-layer), (b) fluorescence spectra of (i) FAM-labeled ssDNA probe (P1) and P1/T1 duplex (ii) without MoS_2 (iii) with MoS_2, (c) fluorescence spectra of P1 using different T1 concentrations and (d) calibration curve for DNA sensing. Adapted with permission from ref. 25 Copyright 2013, the American Chemical Society.

DNA, proteins, metal ions, and tiny molecules. Besides 2D inorganic materials, Peng *et al.* extended the notion of fluorescence sensor fabrication using organic–inorganic 2D MOF nanosheets.[307] Similar to graphene and TMDCs, it has been shown that 2D MOF nanosheets have good quenching capability for probing DNA and can be utilized for the fabrication of fluorescence platforms for DNA sensing. 2D MOF-based sensors (2D Cu-TCPP nanosheet-based) demonstrated superior selectivity and sensitivity with an LOD of 20 pM. In contrast, fluorescent sensors can be expanded to other novel 2D materials, *e.g.*, COFs, MXenes, black phosphorus, and polymers. Specifically, fluorescence sensors based on 2D materials provide several benefits. Firstly, all the fluorescence sensors described above rely on solution-processed 2D materials, which are cost-effective and offer scalable production. In addition, fluorescence sensors provide a relatively quick and straightforward detection method, with a response that only takes a few minutes. The same solution can also be employed to detect a wide range of target analytes. Lastly, 2D material-based fluorescent sensors tend to be more sensitive compared to various other types of fluorescent sensors due to the greater fluorescence quenching efficiency conferred by their 2D structural features. Conversely, fluorescence sensors have several shortcomings. In particular, due to the complicated production of dye-labeled ssDNAs and/or probe DNAs, the resultant fluorescence sensors are extremely expensive. Moreover, the limited stability of fluorescent dyes attached to DNA further limits the life of fluorescent sensors.[66]

3.4.5 Surface-enhanced Raman spectroscopy-related sensors. Because of its distinctive characteristics, surface-enhanced Raman spectroscopy (SERS) has become an ultra-sensitive method for trace molecule detection. However, the production of SERS platforms with a large enhancement factor, greater stability, and outstanding reproducibility is still a big challenge for industrial applications. In this case, due to their novel structures and qualities, 2D materials play a vital role in SERS-based sensors. Flexible SERS sensors can be employed for detection using the swab-sampling method or even *in situ* detection technique, which are different from the old rigid substrate-based SERS detection methods.[308–310] Accordingly, 2D materials can be coupled with flexible SERS sensors to serve as multifunctional layers due to their significant optical transparency, flexibility, chemical inertness to external conditions, and molecule enrichment.

For example, a 3D hybrid MoS_2/AgNPs/inverted pyramid polymethyl methacrylate (IPPMMA) flexible SERS sensor,[311] mounted at the edge of an optical fiber (Fig. 13a and b), could achieve the remote detection of complex analytes. Each analyte molecule could be easily distinguished based on their specific Raman peaks (Fig. 13c). MoS_2 can be used as a protective layer through liquid and atmospheric conditions, indicating its benefits for real-life biosensing applications. Compared to lab research, flexible SERS substrate sensitivity with outstanding performance is still a significant problem for real-world applications. AgNPs@MoS_2/pyramidal polymer (polymethyl methacrylate), a 3D flexible plasmonic structure, has a large surface area and can produce dense 3D plasmonic hot spots (Fig. 13d).[312] A standard melamine solution (Fig. 13e) and melamine and milk mixed solution (Fig. 13e) with a concentration of 10^{-10} to 10^{-4} M and 10^{-6} to 10^{-3} M, respectively, are
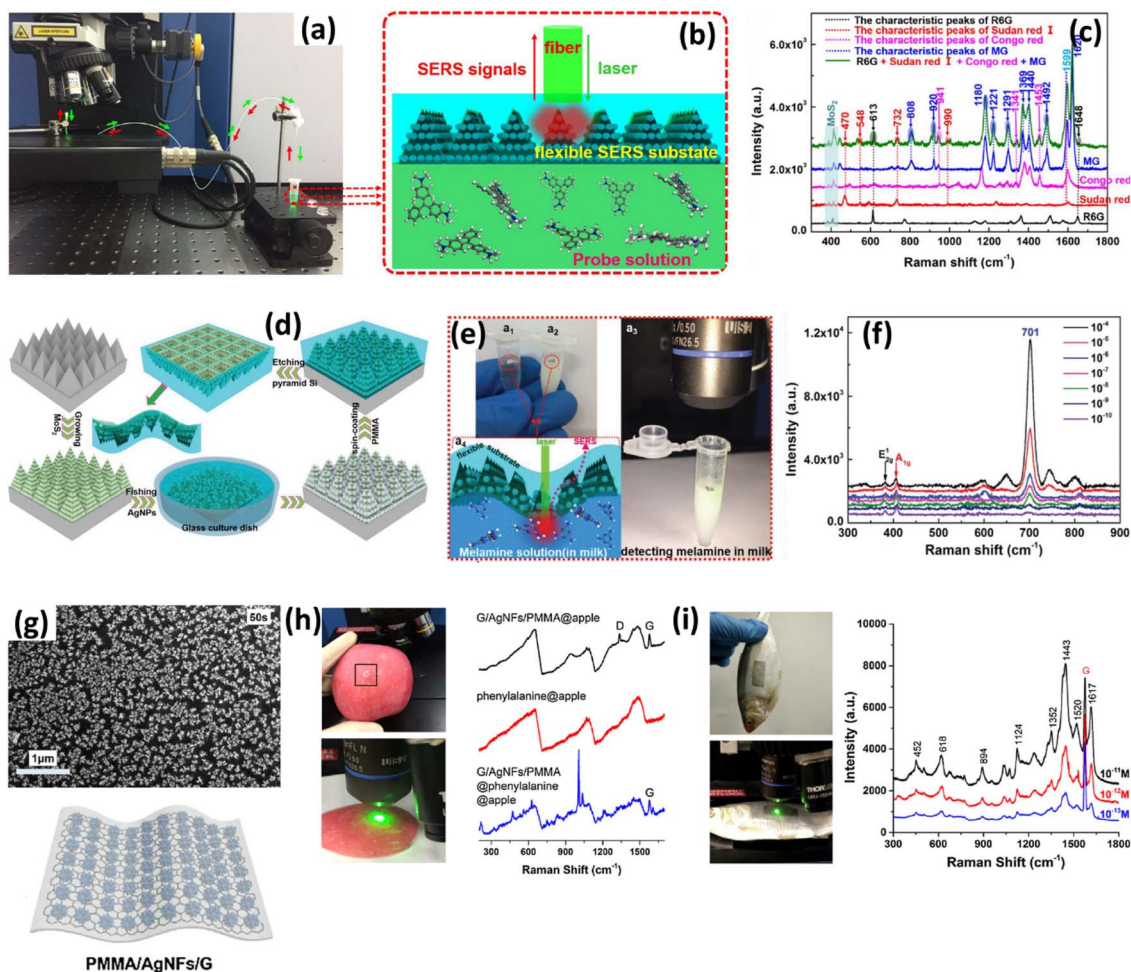
Fig. 13 (a) Photograph of remote detecting mixed molecules. (b) Schematic of the partially enlarged detail on the interface between the MoS_2/AgNPs/iPPMMA flexible SERS substrate and the probe solution. (c) SERS spectra of R6G (10^{-10} M, black line), Sudan red I (10^{-6} M, red line), Congo red (10^{-6} M, pink line), malachite green (10^{-7} M, blue line) and their mixtures (green line). Adapted with permission from ref. 315 Copyright 2018, Elsevier B.V. (d) Schematic of the 3D flexible AgNPs@MoS_2/pyramidal polymer substrate preparation process. (e) Standard melamine solution and (f) SERS spectra of the standard melamine solution with a concentration ranging from 10^{-10} to 10^{-4} M. Adapted with permission from ref. 312 Copyright 2018, John Wiley & Sons, Ltd. (g) SEM images and schematic of the G/AgNFs/PMMA flexible SERS substrate. (h) SERS detection on an apple surface with adsorbed phenylalanine molecules. (i) SERS detection on a fish surface with adsorbed methylene–blue molecules. Adapted with permission from ref. 313 Copyright 2017, Elsevier B.V.

utilized to corroborate the SERS efficiency of the flexible substrate. The 3D AgNs@MoS_2 activated surface was housed on the prepared solution surface solution (Fig. 13e) for *in situ* detection. The characteristic peaks of MoS_2 and melamine could be examined with an ultralow LOD of 10^{-10} M (Fig. 13f). Furthermore, one of the unique advantages of flexible SERS sensors is their ability to couple precisely with arbitrary surfaces, realizing *in situ* on-site sensing. For instance, using a micro-current-assisted chemical reduction procedure and an easy etching process, Qiu *et al.* described the use of PMMA-supported monolayer graphene with sandwiched Ag-nanoflowers (G/AgNFs/PMMA) as a flexible SERS substrate (Fig. 13g). Coating the substrate on the surfaces of real-world materials, such as phenylalanine@apple (Fig. 13h), methylene-blue@fish (Fig. 13i), and aqueous adenosine solution, produced distinct Raman signals. Therefore, it is suitable for the detection of arbitrary morphological or aqueous solution

surfaces.[313] Furthermore, controlling LSPRs to produce high-density local hot spots and significant SERS amplification requires certain nanogaps. Nevertheless, creating 3D ultra-narrow nanogaps for practical applications is a considerable impediment. Li and coworkers described a gyrus-inspired Ag nanostructure designed on graphene/Au films for SERS.[314] The 3D ultra-narrow nano-gaps (~3 nm) were obtained between Ag-gyrus using the width of ~22 nm. This flexible SERS substrate was applied to detect malachite green residue (10–11 M) on prawn skin for *in situ* application. Convincingly, SERS platforms with flexible 2D materials can be perceptually integrated into point-of-care diagnostics using handheld Raman spectroscopy and smartphone expertise.[308]

3.4.5.1 Fine structure characterization. Compared to their 3D counterparts, 2D materials possess a variety of exceptional electrical, optical, physical, and chemical properties due to their fine architectures, including the number of layers, edge

This journal is © The Royal Society of Chemistry 2023

J. Mater. Chem. A, 2023, **11**, 6016–6063 | **6039**

structure, and defects. Consequently, studying these essential structural differences is crucial for modifying 2D materials and their future applications. Raman spectroscopy is an effective tool for probing the microstructure of 2D materials.[316,317] However, the Raman signals from graphene are typically weak, given that they contain a low fraction of scattered radiation, making it challenging to distinguish fine structural properties such as low defect concentration, functional groups, and edge structures. In this case, using the interference-enhanced Raman scattering (IERS) technique,[318] an enhancement ratio of 30 was obtained for graphene. SERS is another spectroscopic technique with high spatial resolution, ultrasensitive detection limits, and great structural selectivity. Therefore, the surface and interference co-enhanced Raman scattering (SICERS) method can achieve a 10 to 10^2 times greater enhancement ratio than IERS or SERS alone using a specially designed substrate of active metal layer/Si oxide/SERS. Furthermore, surface variations and small structural changes in graphene can also be detected. Moreover, some fragments or ribbons on the irregular surface of graphene can be observed through AFM imaging of the material on the IERS and SICERS substrates. In the Raman spectra of graphene on an SICERS substrate obtained with low laser power, two additional peaks can be correctly identified due to the vibrations of the fragments or ribbons on the surface of graphene. This method makes SERS a more effective tool for characterizing ultra-sensitive structures in 2D material-based nanoelectronics.

3.5 Human chemical signal monitoring

The human body produces chemical signals, another type of information vital for personalized healthcare, illness detection, and evaluation. Typically, chemical sensors are composed of two components, $i.e.$, a receptor and type of physicochemical signal transducer. The role of the receptor is to offer better selectivity towards specific biomarkers, whereas the function of the transducer is to turn the chemical information into a quantifiable signal that can be analyzed. By virtue of their large surface area and ease of surface modification, 2D materials exhibit incredible potential to detect human chemical information. Furthermore, chemical sensors based on 2D materials are commonly employed for the non-invasive, cost-effective, and continuous evaluation of different analytical concentrations.[39] They can further be categorized depending on the site where chemical signals are generated, $e.g.$, it can be employed for breath monitoring, sweat, and saliva detection.
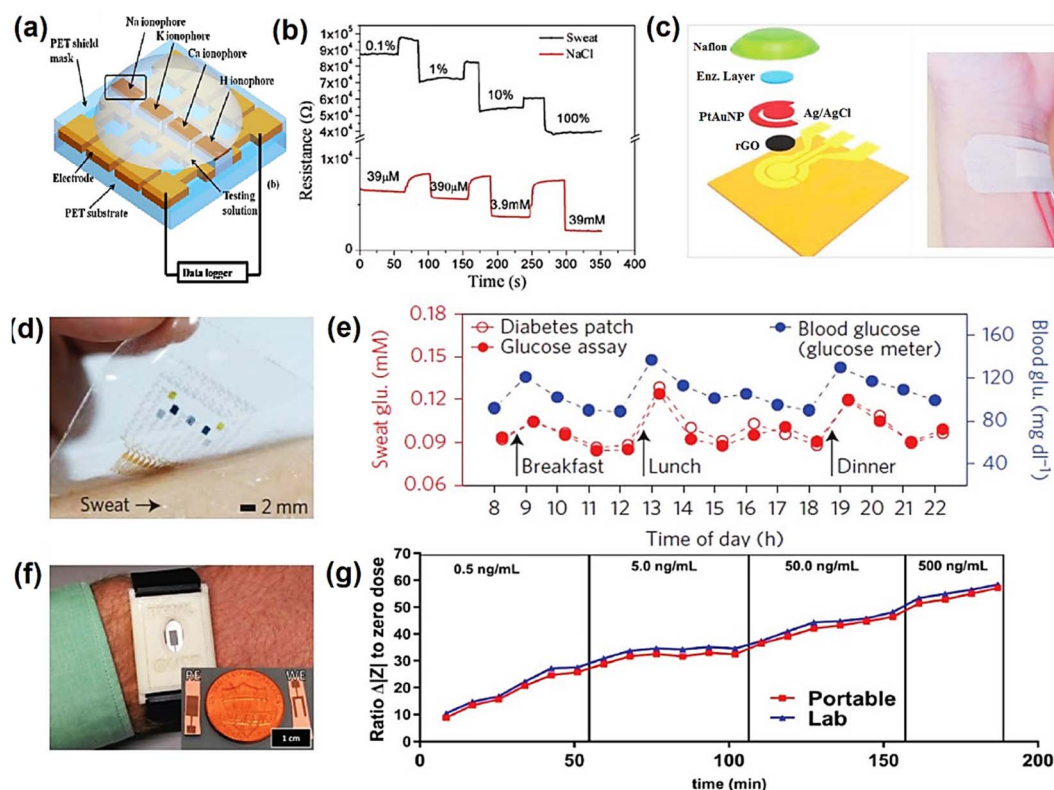

Fig. 14 (a) Representation of ion-sensitive sensor constructed on self-assembled graphene for ion collection and (b) variations in the sensor resistance at various concentrations ($i.e.$, NaCl, and human sweat). Adapted with permission from ref. 355 Copyright 2012, Elsevier B.V. (c) Illustration of rGO-based wearable sweat glucose biosensor with a digital photograph of glucose biosensor on the wrist. Adapted with permission from ref. 356 Copyright 2018, Elsevier B.V. (d) Application of graphene-hybrid based electrochemical prototype on the human skin and (e) analysis of glucose levels in human sweat and blood over a day. Adapted with permission from ref. 357 Copyright 2016, Nature Publishing Group. (f) Digital photographs of transdermal observation of cortisol using MoS_2-based biosensor in human sweat. (g) Lab potentiostat and portable assessment of |Z| cortisol reaction in sweat for 3 h observation. Adapted with permission from ref. 360 Copyright 2017, Nature Publishing Group.

6040 | $J. Mater. Chem. A$, 2023, **11**, 6016–6063

This journal is © The Royal Society of Chemistry 2023

3.5.1 Sweat analysis. When humans exercise, they produce sweat, which is acidic, rich in electrolytes, and produced with metabolite secretion, such as lactate, glucose, and uric acid, as well as many electrolytes (K^+, Na^+, and Cl^-). Sweat is amongst the most readily available body fluids, exhibiting the additional benefit of non-invasive sampling. Given that sweat formation is osmotically coupled to blood formation, sweat can be composed in an acceptable way to provide human health care information for medical diagnosis.[348] For instance, electrolyte imbalance[349] and cystic fibrosis[350] are both indicated by elevated sodium and lactate levels in the sweat. Thus, the continuous detection of the above-mentioned analytes is highly desirable to maintain the optimal physiological balance. Consequently, wearable, non-invasive, and sensitive biosensing platforms are required for continuous sweat analysis.[351] 2D material-based flexible and epidermal biosensors for healthcare management are intriguing alternatives because of their robust mechanical features, large effective surface, thickness, and exceptional redox characteristics.[352–354] When electrolyte ions are out of equilibrium, they can generate severe symptoms, *e.g.*, heart failure, high blood pressure, and renal damage.

Zhang *et al.* examined different concentrations of Ca^{2+}, K^+, and Na^+ ions using self-assembled graphene-based ion-sensitive sensor arrays (Fig. 14a).[355] To ensure the interaction of compatible ions with the active materials, various ionophores were decorated on each sensing region; hence, the conductance of the graphene layer was altered with each ion absorption array. It is worth noting that the graphene sensor exhibited a considerably lower detection limit than the carbon nanotube sensor. Besides, the observation of a small $\frac{1}{f}$ noise in the samples based on graphene was unexpected. This sensor responded quickly and had a minimal LOD for diluted human perspiration in the range of 0.1–100% (Fig. 14b); consequently, the ion sensor array was proven to be beneficial for evaluating sweat ions in human healthcare. This is different from conventional sweat testing, which has the drawbacks of being time-consuming and requiring a significant sample size. Xu *et al.* demonstrated the chromogenic response of a graphene-coupled inverse opal cellulose film to measure the sodium chloride content in sweat as an alternative.[352] It is possible to utilize the reflection spectra of the biosensor to measure body dryness during exercise given that its reflection spectrum redshifted with an increase in the concentration of the sample. As a result of the dramatic color change and diffraction-peak shift, it was quite easy to differentiate the NaCl content in this solution. Due to the strong relationship between the glucose content in sweat and the corresponding level in the blood, glucose is a diabetic biomarker that can be determined through sweat.[348] In the case of diabetes control, glucose concentration is critical. Accordingly, wearable glucose sensors with non-invasive, convenient, and real-time detection capabilities must be urgently developed. Based on rGO nanocomposite electrodes, wearable electrochemical glucose sensors were developed by Xuan *et al.* to measure the blood glucose levels.[356] The working electrode as composed of Au/rGO/AuPt NPs and its surface was coated with Nafion, and subsequently immobilized

with GO_x (Fig. 14c). The redox ability of GO_x catalyzed/oxidized glucose to gluconolactone and hydrogen peroxide. During this event, the current is related to the glucose content and *via* amperometric measurements (*i vs. t*), the redox potential was used to quantify the generation of H_2O_2 on the working electrode surface.

In addition, a waterproof band was used to laminate the sensor to the surface of the skin to support sweat collection. The sensor demonstrated good efficiency and showed a tendency for glucose detection in human perspiration with a short reaction time of 12 s and sensitivity of 82 A mM^{-1} cm^{-2} in the concentration range of 0.1–2.3 10^{-3} M.[39] Recently, Lee *et al.* reported the fabrication of graphene-based multifunctional devices for the continuous assessment and treatment of diabetes.[357] Graphene doped with gold offers excellent conductivity, mechanical robustness, and optical luminosity to provide constant electrical signal transfer. This is useful for electrochemical activity and biological sensitivity and selectivity. Using the diabetes route in human sweat, researchers could perform *in vivo* glucose monitoring (Fig. 14d and e). The detected glucose concentration was consistent when compared with a commercial blood glucose sensor. Upon heating phase-change substances, the formed microneedles can be used as a medication container to release active pharmaceutical ingredients. A potential method for the treatment of the chronic diabetes mellitus is using a conformal integrated device. However, for large-scale applications, complex fabrication techniques are not suitable. Researchers have also worked on the development of graphene-based disposable glucose biosensors.[358,359] Direct laser engraved graphene sensors, which can be manufactured using three easy procedures and utilized for scalable production (see Fig. 14f and g), are particularly suitable for these applications.[360] The charge distribution on the surface of the MoS_2 semiconductor may be altered by the target molecules bound to it, resulting in a change in capacitive reactance and/or impedance. Kinnamon *et al.* employed MoS_2 nanosheets modified with cortisol antibodies in human perspiration for cortisol monitoring based on a similar concept.[360] Through impedance measurements, the sensor showed an LOD of 1 ng mL^{-1} with a dynamic range of 1–500 ng mL^{-1}. A portable device to detect cortisol concentrations in sweat has also been produced, demonstrating a performance equivalent to that of a laboratory potentiometer. It is possible to use graphene and MoS_2 together to create a composite that can be utilized for glucose and lactate sensing.[239] Fast reaction, strong selectivity, excellent repeatability, and flexibility make it a promising candidate for glucose and lactate determination in sweat. Besides TMDCs, MXenes offer enormous potential in various applications for glucose monitoring. Rakhi *et al.* prepared gold nanocluster-decorated $Ti_3C_2T_x$ sheets (Au@$Ti_3C_2T_x$-MXene nanocomposites) and immobilized them with GO_x for glucose detection.[361] The proposed sensor (GCE/Nafion-u@$Ti_3C_2T_x$/GO_x) showed an LOD of 5.9×10^6 M with a concentration range of 0.1–18 mM and exhibited a sensitivity of 4.2 μA mM^{-1} cm^{-2}. Therefore, it is possible to use MXenes and the proposed sensors for the electrochemical measurement of glucose in human sweat, as well as for other applications.

This journal is © The Royal Society of Chemistry 2023

J. Mater. Chem. A, 2023, **11**, 6016–6063 | **6041**

3.5.2 Breath gas detection.

Asthma, smoking-induced diseases, and cystic fibrosis are a few examples of human respiratory disorders that can be assessed using air humidity and volatile organic compounds (VOCs).[362,363] In this case, the respiratory profile of the patient can be constantly monitored and recorded. Furthermore, wearable humidity sensors can also be utilized to detect the dehydration level of patients.[364] There is increasing evidence that asthma symptoms can be affected by differences in air humidity.[365] However, the ultra-trace (as low as ppb) determination of VOCs is essential for contamination studies, therapeutic breath analysis, and identifying hazardous gases, which is essential in the initial diagnosis of several diseases.[366] For example, the presence of acetone in respiratory gas indicates the presence of a diabetic symptom at the
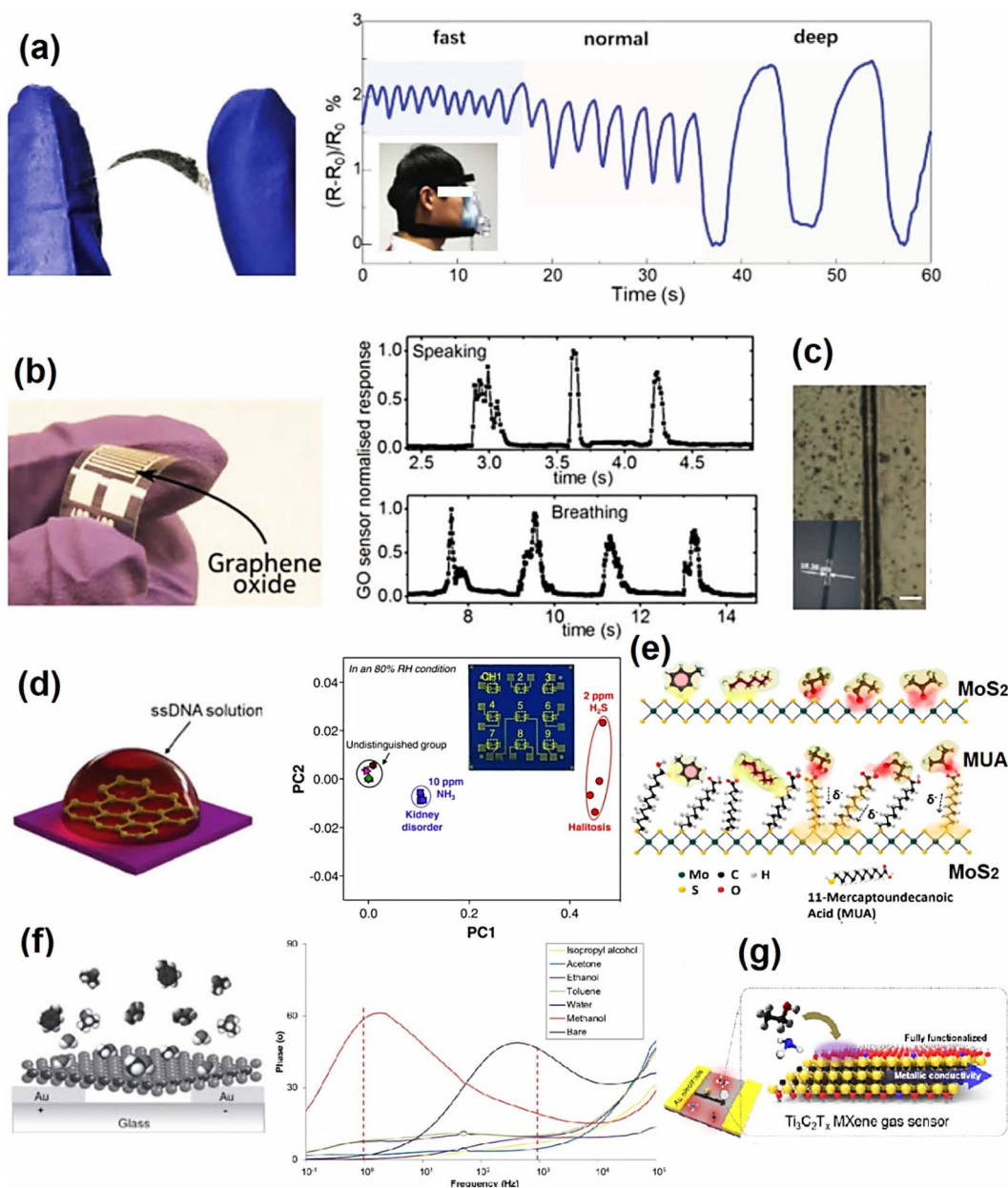
Fig. 15 (a) Illustration of breathing humidity observation using flexible biosensor at different breathing frequencies. Adapted with permission from ref. 364 Copyright 2018, Elsevier B.V. (b) Image of GO-based humidity sensor with signals recorded from breathing and speaking, Adapted with permission from ref. 362 Copyright 2013, the American Chemical Society. (c) SEM micrograph of a fiber humidity sensor based on MoS_2. Adapted with permission from ref. 371 Copyright 2017, Elsevier B.V. (d) Illustration of ssDNA-functionalized graphene-based sensor and PCA. Adapted with permission from ref. 366 Copyright 2017, John Wiley & Sons. (e) Pictorial representation of MoS_2-based detecting mechanism with target VOC molecules. Adapted with permission from ref. 379 Copyright 2014, the American Chemical Society. (f) Representation of 1T-WS_2 nanosheet-based biosensor together with its selectivity behavior (for H_2O and methanol sensing). Adapted with permission from ref. 380 Copyright 2015, John Wiley & Sons Copyright 2015. (g) Demonstration of $Ti_3C_2T_x$-based gas sensor. Adapted with permission from ref. 388 Copyright 2018, the American Chemical Society.

6042 | J. Mater. Chem. A, 2023, 11, 6016–6063

This journal is © The Royal Society of Chemistry 2023

beginning of the course of the disease.[367] Currently, human breathing is the least invasive and most intuitive approach available for analyzing humidity and VOCs for medical diagnosis. Because wearable biosensors are not submerged in human fluids, they can provide continuous measurements of specific biomarkers such as water, NH_3, sulfur dioxide, and other VOCs. Exhaled gas sensors can be realized with 2D materials due to their high surface/volume ratio, providing superior sensitivity, good selectivity, and short reaction and recovery times. Due to their ability to sense humidity, large effective surface area, and substantial flexibility, materials based on graphene, i.e., pure graphene,[368] GO,[369] and rGO,[370] are attractive candidates for the fabrication of wearable electronics for respiration monitoring.[364] When tested on the curved skin surface, the as-constructed sensors demonstrated great flexibility and bending capability (Fig. 15a). This indicates that these sensors have outstanding conformal ability. In the case of humidity sensors, their important performance parameters are linearity, sensitivity, and response/recovery time. However, to increase the sensing profile, porous graphene was modified with GO, Ag colloids, and PEDOT:PSS (poly(3,4-ethylene dioxythiophene)–poly(styrene sulfonate)). The porous graphene/Ag colloids demonstrated the best linearity (0.985 s) with a sensitivity of 0.0321 s. Among them, porous graphene with PEDOT:PSS had the best response time of 31 s and recovery time of 72 s.

It is possible to monitor changes in humidity during breathing when sensors are mounted on a medical mask. Together with the symptoms of apnea and blocked breathing rhythm, they can also distinguish between rapid, regular, and deep breathing. Moreover, humidity sensors can document dehydration before and after water intake, which can benefit patients with speech impairments. GO layers provide hydrophilic properties, which allow water molecules to adhere to the surface and change the electrical characteristics of the humidity sensor. Borini et al. demonstrated a rapid response to moisture by using an ultra-thin GO film on an interdigital electrode.[362] Due to its flexibility, transparency, and large-scale production capacity, GO can be effectively used in a humid environment (Fig. 15b). The response and recovery time were affected by thickness, e.g., a 15 nm-thick film had an average response time of 30 milliseconds. It was used successfully to record subtle notes of human speech and respiration in real time. Various whistled tunes could be classified and distinguished with greater than 90% accuracy using principal component analysis (PCA) and fast Fourier transform, suggesting that this approach is a valuable validation method. A similar non-contact technique was used by the rGO-based humidity sensor, which could acquire information on humidity fluctuations in real time and analyze psychological symbols in the human body.[370] Du et al. prepared an etched single-mode fiber (ESMF) humidity sensor with MoS_2 coating, possessing a diameter of 18 μm and length of ~15 mm (Fig. 15c).[371] The optical frequency conductivity of the MoS_2 sheets varied in response to changes in RH due to the synergistic effects between the MoS_2 and the evanescent field, which resulted in variations in the power of transmitting light.

Regarding the human breath, the MoS_2-coated ESMF showed a considerable rise in transmitting light power up to 14 times compared to the naked ESMF, together with a rapid response (0.066 s) and rapid recovery rate of 2.395 s. The hybridization of MoS_2 with Ag NPs,[372] SnO_2,[373] Cu_2S,[374] and graphene[375] has been extensively investigated to improve the sensitivity, detection limit, and response time. When Ag NPs were used to modify the surface of MoS_2, all the essential parameters showed a significant improvement compared to the pristine MoS_2.[372] It is probable to detect variations in humidity during respiration at various breathing frequencies and during speech. A disposable cellulose-paper-based humidity sensor was developed to measure humidity, temperature, breath quality, and ethanol adulteration, which was also equipped with a portable circuit.[374] The MoS_2/Cu_2S hybrid worked as the active sensing material when used in the flexible and wearable multifunctional system. Several researchers, including Muckley et al., recently investigated the humidity performance of Ti_3C_2 films, a member of the MXene family.[376] MXenes can also be used for respiration monitoring due to their reversible response in the RH range of 0.1% to 95% with an LOD of 20 mTorr H_2O partial pressure with <0.1% RH. Because exhaled breath contains more than 1000 volatile organic chemicals and is strongly humidified (>80%), including carbon monoxide, acetone, hydrogen sulfide, and ammonia, it is imperative to realize a high-efficiency analyzer with substantial selectivity and a detection limit down to the ppb level in complicated gas mixtures.[377,378] Jung et al. proposed sensors in which ssDNA solution was utilized to make the graphene layers more suitable to improve the selectivity and sensitivity (Fig. 15d).[366] Graphene modified by ssDNA also served as an additional sensing channel, which increased the signal processing under intense humidity conditions by increasing the carrier density. A response intensity of 98.5% was observed towards 2 ppm H_2S vapor with an exceptionally low LOD of 0.0053% in RH of 80%. PCA analysis demonstrated that the ssDNA-graphene sensor array can discriminate halitosis and kidney-disordered cancer-related biomarkers, H_2S, NH_3 biomarkers, and other VOCs such as CO, CH_3COCH_3, C_2H_5OH, and $C_7H_{14}O$. Thus, this demonstrates a valid detection network that is inexpensive and a non-invasive diagnosis method to monitor exhaled gases. Wang et al. studied diabetes-related acetone detection in high humidity (85%).[367] For the detection of NO_2, it is possible to obtain rapid reaction and recovery time by including a heater inside the gas sensor made of graphene.[377] This is particularly interesting because multiple functionalized rGO can monitor physiological signals and VOCs simultaneously without interfering with the transmission of signals,[378] which can broaden the scope of its application in preventative medicine. For example, TMDCs such as MoS_2,[379] WS_2,[380] and their hybrids[381,382] display extraordinary semiconducting characteristics, with bandgaps that are adjustable based on thickness and doping molecules used in their fabrication. Thus, TMDCs have the potential to be used in the manufacture of gas sensors. The theoretical analysis results indicated that NO can significantly alter the bandgap and electron transmission of MoS_2,[383] which was also corroborated by the experimental findings.[55]

This journal is © The Royal Society of Chemistry 2023

J. Mater. Chem. A, 2023, 11, 6016–6063 | 6043

In addition, the MUA (mercaptoundecanoic acid)-conjugated MoS$_2$ films produced by Kim et al. were used as tunable VOC sensors with variable response times.[379] VOC molecules were physisorbed on sensing channels due to dipole-induced scattering (Fig. 15e) and were responsible for rapid reactions with toluene and hexane vapors (Fig. 15a and b). In addition to providing high-energy binding sites for VOCs, the MUA-MoS$_2$ coating prevented them from attaching directly to the surface of MoS$_2$. Therefore, it showed greater resistance fluctuation compared to MoS$_2$. Further, the sensor showed a high sensitivity and a lower LOD of 1 ppm, which suggest the use of breath analysis in lung cancer diagnosis in the near future. Mayorga Martinez et al. investigated the selective gas performance of 1T-WS$_2$ in their study.[380] Methanol and water could be separated using impedance spectroscopy because of the impedance phase difference between them (Fig. 15f). This device has potential to be employed as a dependable, sensitive, and repeatable instrument for onsite gas sensing applications, particularly in the case of inhaling complex gas mixtures that are present in the environment. Besides graphene and the family of TMDCs, the exceptional surface chemistry of MXenes and their excellent conducting nature and biocompatibility make them an extremely appropriate matrix for improved biological sensing systems, together with other applications.[384–386] MXene materials utilized in solid-state gas sensors presented minimal electrical noise, excellent signal efficiency, adaptable fabrication, and portability. They have been proven to be successful in detecting various gas molecules with good signal strength, versatility, and accessibility. Yu et al. reported first-principle calculations to theoretically anticipate the potential use of MXenes in the field of gas sensing.[384] They observed that the oxygen-terminated Ti$_2$C single layer (Ti$_3$C$_2$O$_x$) is incredibly selective to ammonia compared with other gas molecules, including NO$_2$, CH$_4$, O$_2$, and N$_2$. Lee[387] and Yuan et al.[385] further confirmed that Ti$_3$C$_2$ gas has excellent resistance towards ethanol (C$_2$H$_6$O), methanol (CH$_3$OH), acetone (CH$_3$)$_2$CO, and ammonia (NH$_3$). Ti$_3$C$_2$T$_x$ displays both minimal signal noise and robust signal processing for VOCs, as proven recently by Kim et al.[388] Filtration of a diluted colloidal Ti$_3$C$_2$T$_x$ MXene layer AAO membrane resulted in the formation of an MXene film, which was subsequently transferred to an SiO$_2$ wafer printed with gold-sensing electrodes (Fig. 15g). Acetone, ethanol, ammonia, and propanol were detected with strong response signals from MXene-based gas sensors, but NO$_2$, SO$_2$, and CO$_2$ were detected with a considerably lower response, suggesting superior selective detection for VOCs in the gas sensor. Furthermore, MXenes have great potential in gas sensing with ultrahigh signal/noise ratio in contrast with their 2D counterparts such as MoS$_2$, black phosphorus, and rGO.

3.5.3 Saliva detection. Besides being one of the most prevalent chemical samples, saliva, together with sweat and tears, contains a broad range of biomarkers that are the same as that in the blood. Furthermore, the high volume of saliva fluid and big mouth cavity are both favorable for sample collection
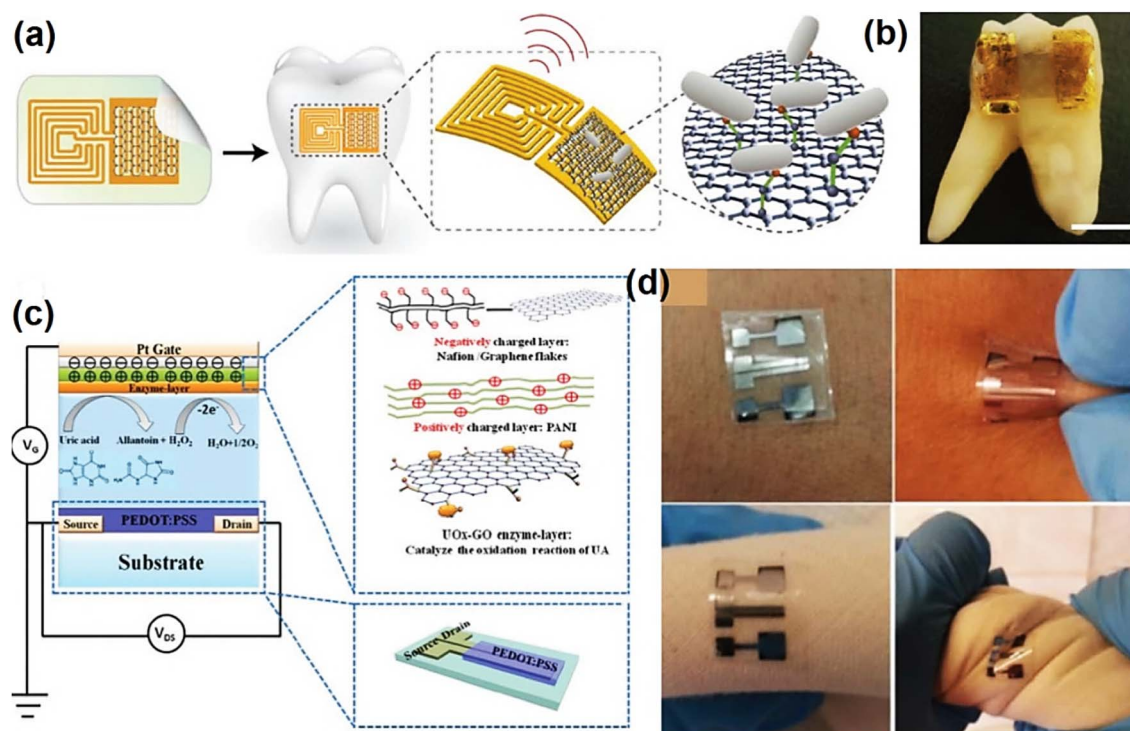

Fig. 16 (a) Graphical representation of graphene/silk-based wireless biosensor (mounted on a tooth) for sensing bacteria. (b) Digital photograph of the developed sensor (over tooth surface). Adapted with permission from ref. 392 Copyright 2012, Nature Publishing Group. (c) Schematic of the working mechanism and organic electrochemical transistor with Pt-gate/Nafion-graphene/PANI/UO$_x$-GO employed for saliva analysis. (d) Application of proposed sensors on various surfaces. Adapted with permission from ref. 393 Copyright 2015, John Wiley & Sons.

6044 | J. Mater. Chem. A, 2023, **11**, 6016–6063

This journal is © The Royal Society of Chemistry 2023

and sensor localization. However, although there have been some studies on saliva sensors to detect glucose[389] and lactate,[390] the application of 2D materials in saliva inspection remains rare.[391] Using a live saliva sample, Mannoor *et al.*[392] introduced a wireless sensor composed of elastic graphene and silk, which was sufficiently flexible to be worn on the finger and employed to detect bacteria in dental enamel. Antimicrobial peptides were added to the surface of graphene to enable the detection of harmful bacteria over a vast range and time on the material surface. The signals generated by the bacterium concentration could be sent to an external device without requiring an external power source by combining a sensing area of graphene using an inductive coil antenna (Fig. 16a and b). Also, it was possible to connect it to tissues or tooth enamel because of the water-soluble and biocompatible silk substrate. The results indicate that monitoring bacteria in the mouth is effective because there is a linear correlation between the logarithm of bacteria content and the variation in resistance. Recently, Liao *et al.* developed flexible organic electrochemical transistors for the determination of glucose and uric acid in saliva,[393] which was capable of withstanding considerable deformation (Fig. 16c and d). Immobilization of the enzyme uricase (UO_x) on the surface of graphene was performed for the selective detection of uric acid. The positively and negatively charged double layer of Pt-gate/Nafion-graphene/PANI/UO_x-GO could prevent the interaction between uric acid and glucose. According to the results, the proposed device exhibited a detection limit of $\sim 1 \times 10^{-8}$ M, which is nearly three times the magnitude and superior to the detection limit of traditional electrochemical techniques.

Furthermore, biosensors have been successfully used for the instantaneous monitoring of glucose and uric acid concentrations in saliva, implying that they represent potential technology for the non-invasive detection of saliva biomarkers. From an application point of view, wearable electronics made from 2D materials are designed to detect sweat, saliva, and breathing gases. Based on this, the graphene family is the most often utilized active material in both applications. However, due to their limited selectivity, the detection of some VOCs during respiration remains a significant obstacle, despite various demonstrations for their practical use, such as sensing the moisture in respiration, detecting electrolytes in sweat, and determining glucose in sweat. Another critical problem that requires attention is the low levels of specific biomarkers in VOCs. For practical applications, the LOD and selectivity of chemical sensors based on 2D materials need to be enhanced. Their efficacy can be optimized by considering their rich chemical environment and signal processing efficiency.

3.6 Biomedical and health care sensors

3.6.1 Single-cell detection.
Single sick cell detection, which distinguishes unhealthy from healthy cells, provides details about the ailment and plays a significant part in diagnosis.[394] Consequently, the reliable identification of single cells is needed amongst healthy cells. Currently, optofluidic technologies and flow cytometry are the most widely used approaches for on-site single-cell detection.[394] However, these systems have difficulty detecting single cells and require a laser source (high-energy source), which can destroy the cells. Xing *et al.* created a graphene-coupled surface plasmon resonance (SPR) sensor that offers an elevated resolution (1.7×10^{-8}) and high sensitivity (4.3×10^7 mV per RIU), and further used for single cell identification of cancer cells in a group of healthy cells.[394] As the input source, a helium-neon (He–Ne) laser ($\lambda = 632.8$ nm, $P = 80$ mW) was utilized, which was then converted into circularly polarized light by a polarizer and quarter-wave plate. A schematic illustration of the graphene-based optical prism sensor (GOPS) is displayed in Fig. 17a (inset), possessing a sandwiched structure of quartz over prism, thick h-rGO (8.1 nm), microfluidic chip of polydimethylsiloxane, and cell flow. The optical microfluidic channel possessed a width of ~ 20 μm and height of ~ 12.5 μm. An improvement in the detection range was achieved *via* a diaphragm using a polarized light (reflected) beam spotted over 1 μm. Subsequently, the obtained beam was allowed to pass *via* a polarization beam splitter (PBS) to isolate the transverse magnetic and electric modes, which were identified through a stable photo-detector.[394] In single-cell detection *via* this experiment, the normal lymphocytes and Jurkat cancer cells (JCCs) (1%) present in the blood could be perceived through the modification of the voltage through a microfluidic device called GOPS.

Further, the size and refractive index of JCCs are considerably higher compared to ordinary lymphocyte cells. Discrete fluctuations in voltage signal (considering amplitude) with time were observed, as displayed in Fig. 17b, which revealed the flow of normal lymphocytes and JCCs at a 7 μL h^{-1} approximate rate *via* the h-rGO-based optical microfluidic channel. Additionally, the high and low-voltage signals, as presented in Fig. 17c, agree with the presence of JCCs and normal lymphocyte, signifying superior sensitivity and resolution of GOPS. Consequently, even a single cancer cell could be identified from the neighboring healthy cells. The microscopy images are shown in Fig. 17d and e, where the JCCs (Fig. 17d) are typically bigger compared to normal lymphocyte cells (Fig. 17e). The average refractive index of cells refers to the average size of normal and cancerous cells, which can be precisely identified through an optical refractive index sensor based on graphene.[394]

3.6.2 DNA sensing.
DNA detection is extremely significant in diagnostics. Genetic treatment, disease diagnosis, biological applications, point-of-care clinical analysis, food, and environmental monitoring all depend on the rapid detection of selective DNA molecules at ultra-low concentrations. Polymerase chain reaction, well-known as PCR, is a signal amplification technique and has been extensively employed for the detection of DNA.[395] It has been shown that surface-enhanced Raman scattering and silicon nanowire sensor-based FETs can directly detect DNA at low concentrations.[395] Recently, the use of 2D materials in DNA sensing applications has been investigated because of their large effective surface and distinctive optoelectronic characteristics. It is well known that graphene and its derivatives (such as GO) have highly sensitive DNA hybridization capabilities at concentration levels down to a few hundred micromolar. Based on optical PL, a graphene stacked MoS$_2$
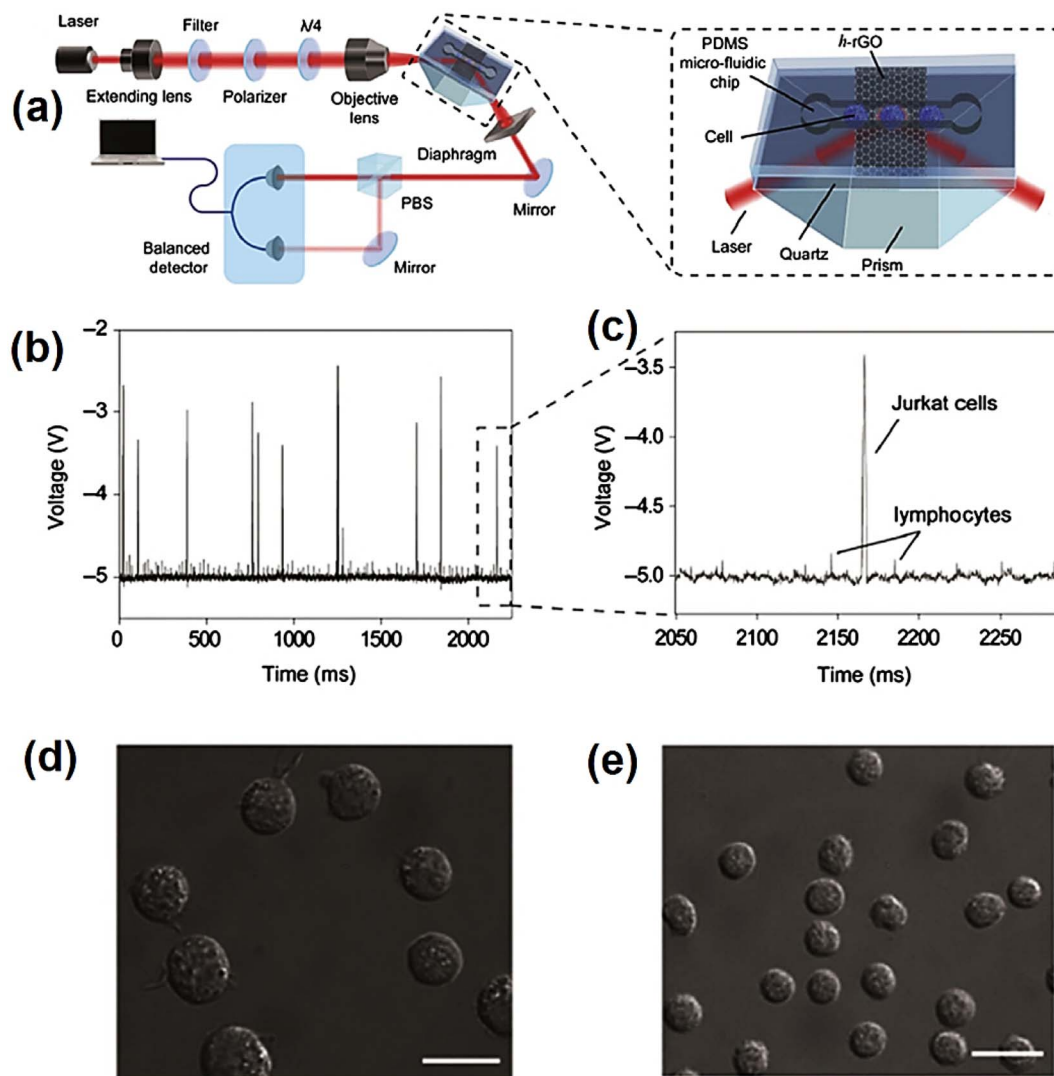
This journal is © The Royal Society of Chemistry 2023

J. Mater. Chem. A, 2023, **11**, 6016–6063 | **6045**

Fig. 17 Schematic of optical prism coated with graphene for the ultra-sensitive low detection of distinct cells (a typical SPR system): (a) flow-detecting structure for a single-cell setup, and the inset corresponds to optical sensor platform with graphene-coated for single cell detection, (b) distinct voltage change (time-dependent) agreeing with mixed Jurkat cells and lymphocytes due to their rolling through h-rGO sensing frame and (c) enlarged image of certain positions of the panel (voltage signals are clearly described). Microscopic image (15 μm scale bar) of (d) Jurkat cells and (e) lymphocytes. Adapted with permission from ref. 394 Copyright 2014, the American Chemical Society.

(graphene/MoS₂) heterostructure as a sensing substrate reported by Loan *et al.* showed sensitive detection towards DNA hybridization down to the attomolar (aM) level.[395] When used in PL, monolayer MoS_2 offers fluorescence-quenching solid capability. Graphene is a single-layer material that works as a barrier between MoS_2 and its surrounding environment, preventing material degradation.

It also operates as a biocompatible interface layer, allowing DNA molecules to be hosted on its surface. Fig. 18a depicts a schematic layout of the PL experiment that was employed for ultrasensitive DNA detection hybridization *via* the proposed hetero-structure device. The PL spectrum obtained following the interaction of DNA molecules was investigated *via* confocal microscopy. The spatial PL area mapping for the DNA solution immobilized on the proposed hetero-structural sensing substrate (40 L; 10 M) is shown in Fig. 18b. Furthermore, the

sensing substrate was hybridized with the corresponding DNA solutions (different dilutions from 1 to 100 aM). As more target DNA was immobilized on the substrate, the PL mapping intensity increased proportionally. The sensing substrate was rinsed with ultra-pure water and dried after each incubation of probe and target DNA, and PL measurements were carried out under dry conditions. The integrated PL peak area was corelated with the target DNA in the concentration range of 1 aM to 1 fM, as depicted in Fig. 18c, recorded in the range of 1.7–1.95 eV for each condition. The results of the PL color mapping show that the graphene/MoS₂ heterostructure sensing substrate determined the target DNA in a low concentration down to the aM level.

3.6.3 Protein sensing. The biomedical industry requires sensitive, ultra-fast, and small biosensors to for the detection of proteins in real time. The various protein detection methods
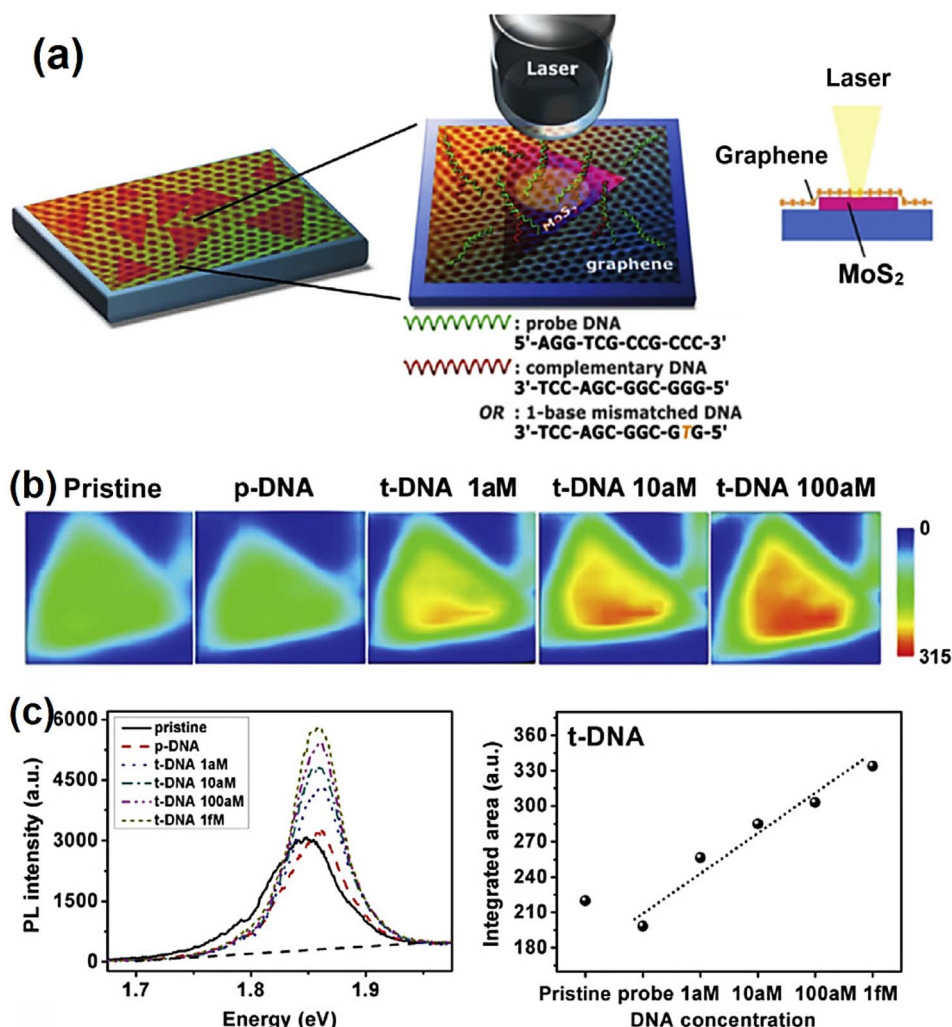
6046 | *J. Mater. Chem. A*, 2023, **11**, 6016–6063

This journal is © The Royal Society of Chemistry 2023

Fig. 18 (a) Representation of DNA sensing strategy using graphene/MoS$_2$ heterostructure sensor and an optical microscope, (b) mappings of PL peaks of target DNA-hybridized heterostructure sensing substrate, and (c) PL spectra and integrated PL peak of target DNA-hybridized heterostructure sensing substrate. Adapted with permission from ref. 395 Copyright 2014, John Wiley & Sons.

include enzyme-linked immunosorbent assays (ELISAs), mass spectrometry, radial immunodiffusion, and western blotting. Alternatively, the development of optical fiber-based labeled-free platforms for protein sensing/detection is currently gaining great attention. An optical fiber sensor towards C-reactive protein (CRP) determination was realized by coating an etched fiber Bragg grating (eFBG) with aCRP-GO (anti-CRP antibody), as shown in Fig. 19a.[396] CRP is a biomarker for cardiovascular illness and chronic inflammation and can be helpful for doctors for the diagnosis of diseases. Currently, different methods are employed to identify CRP, including the conventional ELISA, quartz crystal microbalance, electrochemistry, and SPR with a linear range of (0.3–10 mg L^{-1}), (0.13–5.01 mg L^{-1}), (0.1–50 mg L^{-1}), and (2–5 mg L^{-1}), respectively.[396] The Bragg's wavelength (λ_B) of eFBG sensors coated with aCRP and aCRP-GO complex changed linearly with CRP concentration, as shown in Fig. 19b, respectively. In contrast to the eFBG sensors coated only with aCRP, the difference in Bragg's wavelength ($\Delta\lambda_B$) for the eFBG sensors coated with the aCRP-GO

complex (6.3 pm for unit order increase in the concentration of CRP) was double (1.2 pm for unit order increase in the concentration of CRP). The low LOD (0.01 mg L^{-1}) of the aCRP-GO complex-coated eFBG sensors further demonstrated the role of GO in enhancing the sensitivity of the eFBG sensors compared to the aCRP-coated eFBG sensors, which had an LOD of 1 mg L^{-1}. The urea, glucose, and creatinine concentrations in aqueous solutions are shown in the inset of Fig. 19b together with the $\Delta\lambda_B$ values for each concentration. After the incubation of urea (2000 mg L^{-1}), glucose (4000 mg L^{-1}), and creatinine (6000 mg L^{-1}), it was observed that $\Delta\lambda_B$ in the case of the aCRP-GO-coated eFBG sensors was smaller than 2 pm.[396] It was observed that the sensitivity of the coated eFBG sensors in the presence of urea remained unaffected. As seen in Fig. 19c, $\Delta\lambda_B$ varied proportionally to various CRP values in the presence of urea, glucose, and creatinine. This is illustrated in Fig. 19c, where it can be seen that the proposed eFBG devices had the same sensitivity towards CRP detection and showed good selectivity when subjected to interfering agents.[396] The
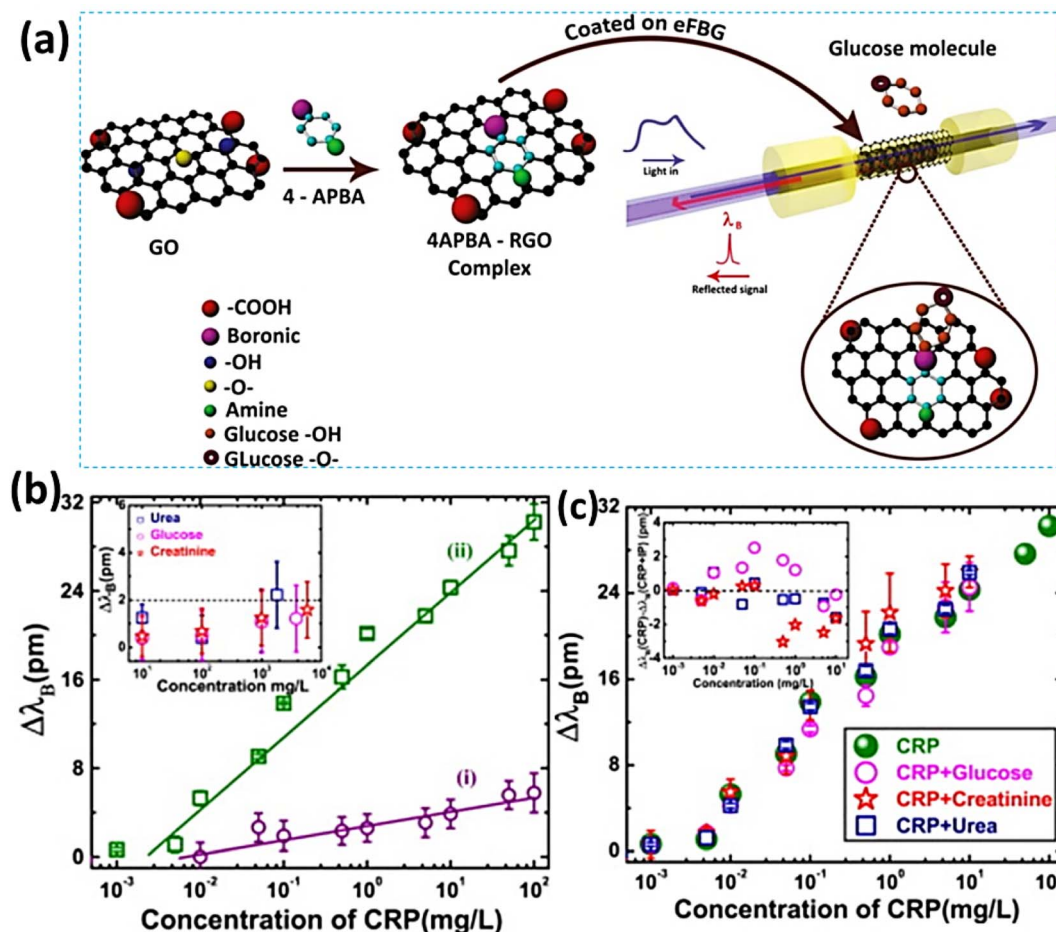
Fig. 19 (a) Graphical representation of eFBG sensor layered through aminophenyl boronic acid-rGO complex for glucose detecting mechanism. Adapted with permission from ref. 397 Copyright 2016, John Wiley & Sons. (b) Shifted Bragg's wavelength for different CRP concentrations in the case of (i) aCRP and (ii) aCRP-GO complex-coated eFBG sensors (inset corresponds to shifted Bragg's wavelength concerning interfering concentration, for example, magenta color for glucose, blue for urea and red for creatinine), and (c) shifted Bragg's wavelength for a concentration of CRP in the presence of creatinine (5800 mg L^{-1}), glucose (3800 mg L^{-1}), and urea (1800 mg L^{-1}) (inset represents modification in $\Delta\lambda_B$ aimed at different concentrations of CRP with respect to various concentrations of CRP in the presence of contrast agent, *e.g.*, creatinine, glucose, and urea). Adapted with permission from ref. 396 Copyright 2015, Elsevier B.V.

comparable values for CRP when subjected to interfering compounds were in the range of 0.2–3 pm, which is notable compared to the corresponding values for CRP determination without any interfering compounds. Using this device, this variation in $\Delta\lambda_B$ is quite similar when calculating the base values of the Bragg's wavelength. The specificity of the aCRP-GO-coated eFBG sensors was demonstrated by analyzing the slight change in $\Delta\lambda_B$ for CRP when CRP was determined in the presence of interfering agents, *e.g.*, urea, glucose, and creatinine.

3.6.4 Cancer diagnosis and treatment (photothermal and chemotherapy). Currently, cancer is considered to be one of the most fatal diseases. Carcinoma cells multiply, leading to the formation of tumors in a specific section of the body, which also spread to various other parts. These tumors can adhere and kill the strong tissues/organs in the surrounding area, eventually leading to death. When cancer spreads from one organ to another, it is known as metastasis. In this case, the site where

cancer cells begin to proliferate enables different forms of cancer to be distinguished,[398,399] each of which requires a different strategy for diagnosis and therapy. For instance, breast, lung, kidney, and liver cancer all begin in various places. In addition to optics-based imaging techniques, *e.g.*, fluorescent and Raman spectroscopy, cancer biopsy is also commonly used to diagnose the disease, which can provide information on the onset, growth, and spread of the cancerous tumor. Some treatment options include stem cell transplant, radiation therapy, chemotherapy, biological and hormone therapies, and/ or surgery. However, most techniques for diagnosing and treating cancer are expensive, invasive, and ineffective.

Consequently, it is critical to develop precise and cost-efficient cancer detection methods, and subsequent treatment techniques. Recently, graphene and its derivatives, as well as other nanomaterials, have made new techniques conceivable in the field of biosensors.[398] The various properties of graphene and graphene-quantum dots make them attractive candidates

6048 | *J. Mater. Chem. A*, 2023, **11**, 6016–6063

This journal is © The Royal Society of Chemistry 2023

for use as fluorescence probes in phase contrast imaging (PL imaging). Fluorescence-based biosensors should be biocompatible, photostable, non-toxic, and chemically inert, and hence these factors must be considered during the fabrication of these devices. Graphene-based fluorescent probes for PL have two critical functions, as follow: (i) they can identify cancer cells with high specificity and (ii) they can also be used to deliver therapeutic drugs. Cancer tumors have been successfully treated and cured with light-induced thermal treatment in clinical trials. During photothermal treatment, near-infrared (NIR) light penetrates only a limited depth in the target human tissues, allowing medications to be delivered safely. Alternatively, the use of phototherapy alone may result in the partial destruction of cancer cells.

In this case, photothermal therapy combined with chemotherapy is a more effective therapeutic option than either treatment alone. When combined with photothermal therapy, chemotherapy can increase the effectiveness of the cancer treatment by targeting cells and blocking the regeneration of impaired (tumor-affected) blood vessels. Recent developments include the development of light-illuminated NPs, which discharge their payload in response to light activation, resulting in increased bioavailability, while maintaining high efficiency.[398,399] Recently, Liu et al. achieved excellent drug delivery to cancer cells by combining photothermal and chemotherapeutic targeting of cancer cells using PEGylated 2D MoS_2 nanosheets.[398] The IR absorption of 2D MoS_2-PEG (polyethylene glycol) nanosheets is extremely strong, making them suitable for photothermal treatment. Nanosheets possess a high surface/mass ratio, which allows an active loading of medicinal compounds, i.e., chemotherapeutic medications doxorubicin (DOX) and photodynamic agent chlorine e6 (Ce6). Fig. 20a illustrates the detailed fabrication of MoS_2/PEG used for drug loading, as follows: MoS_2 nanosheets were functionalized with lipoic acid-modified PEG (LA-PEG) using a thiol method to enhance their physiological stability and biocompatibility. For the in vivo treatment of cancer, the combination of photothermal and chemotherapy techniques can be used with DOX-loaded MoS_2-PEG nanosheets, as shown in Fig. 20b–f. Female Balb/C mice had their backs vaccinated with 1×10^6 murine
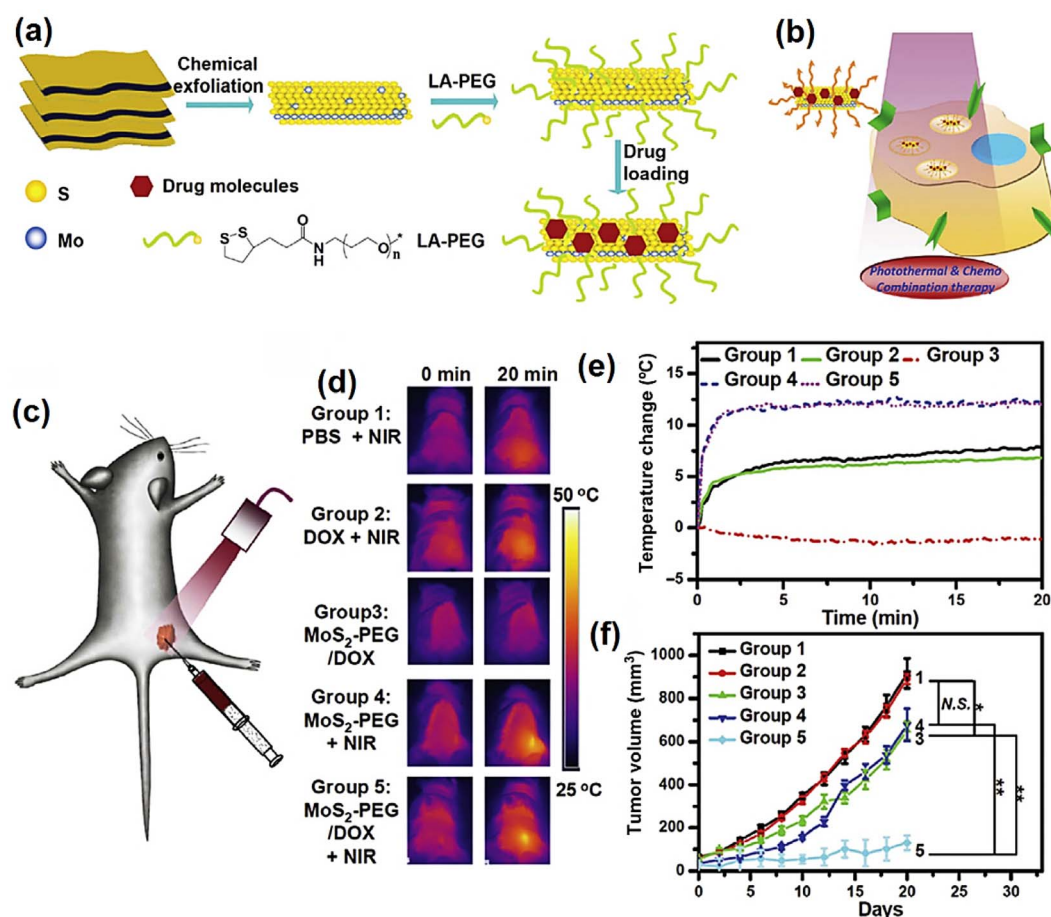

Fig. 20 (a) Systematic illustration of the development route of PEG-MoS_2 and corresponding drug loading scheme. (b) Depiction of targeted in vitro therapy employing the MoS_2/PEG/FA/DOX complex, (c) demonstration for a group of therapy centered on intratumorally introduced complex of MoS_2-PEG/DOX, (d) display of 4T1 tumor-bearing mice via IR thermal photograph using an IR camera, (e) monitoring of IR thermal camera for a change in temperature of tumors aimed at different groups in the course of laser treatment as directed in (c), and (f) curves representing the tumor volume progress in different groups of mice when subjected to several treatments. Adapted with permission from ref. 398 Copyright 2014, John Wiley & Sons.

This journal is © The Royal Society of Chemistry 2023

J. Mater. Chem. A, 2023, **11**, 6016–6063 | **6049**

breast cancer 4T1 cells (in 40 μL PBS). Subsequently, the mice divided into 5 clusters, and 20 μL of PBS, DOX, MoS_2/PEG, and MoS_2/PEG/DOX was inoculated intravenously, respectively. The comparison of the temperatures of the mice inoculated with the above-mentioned therapeutic molecules, as shown in Fig. 20d, showed the significant increase from room temperature to 44 °C and 45 °C when the tumor volume reached ~50 mm³. The animals injected with MoS_2/PEG/DOX intratumorally but not subjected to laser treatment served as the control group in this study. In the following 21 days after completing the various therapies, the tumor length and width were measured every two days with a digital caliper. Within only 21 days after injection, the tumors injected with PBS or free DOX had grown rapidly, indicating that a low dose of DOX was not effective in preventing tumor development. In contrast, the growth of tumors in the group injected with MoS_2-PEG/DOX and subjected to NIR activation was significantly suppressed following the combination of photothermal treatment and chemotherapy. This suggests that the MoS_2/PEG nanosheets loaded with DOX could reduce tumor development synergistically with photothermal and chemotherapy.[398]

3.6.5 Optogenetic sensing. Neurologists are trained in various disciplines, with a particular emphasis on anatomy and nerve function or the brain system. In optogenetics, specific neuronal circuits within the brain are controlled through light.[400,401] It is also indicated in animal modules that these circuits are associated with many parts of human behavior and personality (Fig. 21a). Optogenetic technologies are crucial for the treatment of some of the most severe neurological diseases, including autism, Parkinson's disease, depression, anxiety, schizophrenia, substance abuse, strokes, and spinal cord injuries. Micro-electrocorticography (micro-ECoG) uses neural

interfaces to reach brain neurons for non-invasive analysis and recording of neuronal signals from a patient's brain suffering from various neurological disorders. At present, micro-ECoG arrays are made up of indium tin oxide (ITO). However, ITO has many drawbacks, making it unsuitable for use as a neural interface, including fragility, requiring processing at higher temperatures, non-compliance with the cortical surface, and refraction of light, which is a crucial factor in optogenetics, and neural imaging is significantly limited to UV and IR. These disadvantages can be solved using graphene-based micro-ECoG neural layers, which also have several advantages, including biocompatibility, adaptability, mechanical robustness, wide wavelength refraction, elevated electrical and thermal conductivity, and tunable photonic properties.[401] As shown in Fig. 21b, optogenetics and brain imaging devices on graphene-based carbon-layered electrode array (CLEAR) technology are extensively employed. The CLEAR device consisted of four layers of graphene with 76 Ω^{-2} resistance/unit-layer, which allowed it to retain a broad wavelength (300–1500 nm), while maintaining ~90 percent transmission with better mechanical strength compared to ITO and may other ultra-thin metals. Fig. 21c shows a digital photograph of the optogenetic studies performed on a mouse. A CLEAR device was placed on the cerebral cortex and a 200 μm optical fiber was used to stimulate neurons by radiating a blue laser ($\lambda = 473$ nm, $P = 100$ mW), while the electrical output signal was recorded simultaneously. As shown in Fig. 21d, the installed device indicated the application of blue light. When blue (473 nm) light was used to stimulate optogenetics, the following steps are taken: first, archaebacteria and algae channelrhodopsin-2 (a light-sensitive protein) is isolated and utilized, which creates an electric current by employing ions in response to radiating light (i.e., blue light). Thy1:ChR2
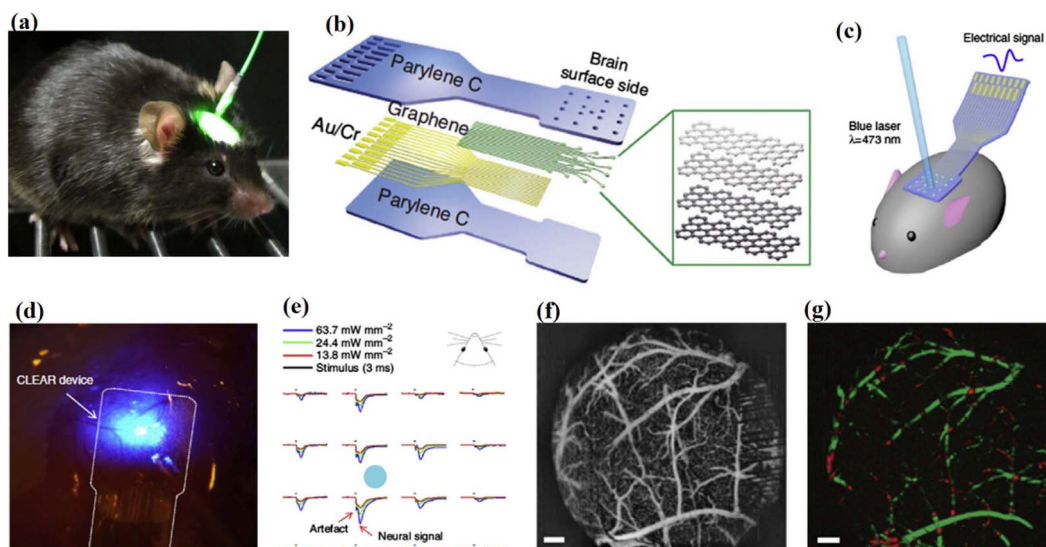

Fig. 21 Depiction of CLEAR device towards optogenetic applications as well as neural imaging: (a) implementation of optogenetics in an animal module. Adapted with permission from ref. 402 Copyright 2013, Proceedings of the National Academy of Sciences. (b) Development route for CLEAR device, (c) presentation of experimental arrangement, (d) blue light stimulus image using an optical fiber, (e) CLEAR device towards the recording of optical evoked potentials (scale bars: x-scale = 50 ms and y-scale = 100 μV), (f) demonstration of full intensity projection of OCT angiogram, and (g) doppler blood flow velocity image. Adapted with permission from ref. 401 Copyright 2014, Nature Publishing Group.

6050 | *J. Mater. Chem. A*, 2023, **11**, 6016–6063

This journal is © The Royal Society of Chemistry 2023

mouse brains include DNA taken from channelrhodopsin-2, which was subsequently implanted in specific neurons. These neurons transmit by "firing", that is, by opening and shutting ion channels to generate an electrical signal. Finally, the CLEAR device was used to record light-stimulated responses in the cerebral cortex of the mouse brain. Three distinct light intensities were used in conjunction with a stimulus period of three milliseconds (Fig. 21e). Additionally, the cerebral vascular 3D optical coherence tomography (OCT) angiography view of the mouse brain was visible due to the excellent transparency of the CLEAR device at wavelengths in the IR region (Fig. 21f). As seen in Fig. 21g, the usual velocity profile of the blood flow in the cerebral arteries is evident with the CLEAR instrument. This work demonstrates a simplistic implementation of a CLEAR device based on 2D materials and designed to be used in applications of neural imaging and optogenetics.[401]

3.6.6 Ophthalmology sensing. Recently, numerous wearable devices have been developed *via* stretchable and flexible nanomaterials, together with developments in intelligent electronics, micro/nano-manufacturing, and information technology. Currently, the demand for biomedical wearable devices and research interest in this field have grown significantly (*e.g.*, the fabrication of smart contact lenses).[403–405] To develop these wearable devices, electrodes for various sensing applications must be environmentally stable and biocompatible. Consequently, innovative 2D materials significantly contributed to the
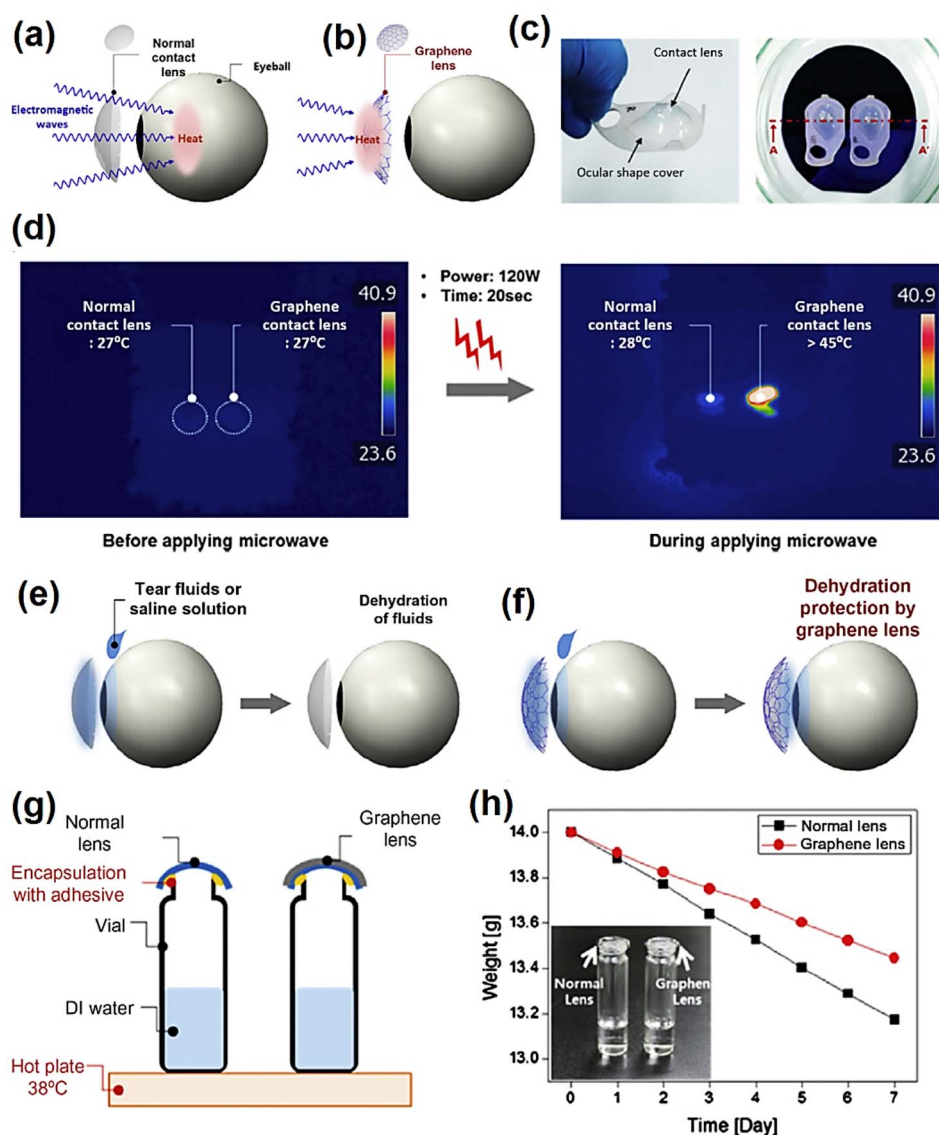

Fig. 22 Schematic of the working principle of contact lens coated with graphene: (a) interaction of EM wave and contact lens, which shows that the eye absorbs the EM wave (this may result in heat destruction inside), (b) absorption of EM energy through graphene in addition to heat dissipation before approaching the internal structure of the eye, (c) synthesis of sample aimed at microwave oven testing, (d) measurement of elevated temperature (for the interior of a microwave oven) for graphene-coated lens *via* displayed photograph using IR camera, (e and f) demonstration of gas-impermeability of graphene, which leads to a reduction in the dehydration of a contact lens, (g) trend of evaporation rate (for water) using the experimental arrangement shown, and (h) measurement of weight loss as a function of time on hot plate (38 °C). Adapted with permission from ref. 403 Copyright 2017, the American Chemical Society.

This journal is © The Royal Society of Chemistry 2023

J. Mater. Chem. A, 2023, **11**, 6016–6063 | **6051**

fabrication of wearable biomedical devices, such as graphene. Wearable contact lenses can also detect glaucoma and diabetes by measuring the glucose composition in tears and intraocular pressure.[403] Dry eye syndrome can also be caused by using contact lenses for a long period. Accordingly, it is necessary to shield the eyes from electromagnetic interference shielding (EMI) and retain their moisture through a diffusion barrier.[403] The fabrication of smart eye contact lenses was reported by Lee *et al.*, which is based on graphene grown *via* the CVD strategy, and thus serves as EMI and dehydration protection to avoid eye diseases (*i.e.*, cataracts).[403] The EMI shielding working principle of graphene-based eye contact lenses is schematically represented in Fig. 22a and b. In the absence of graphene protection, EM waves are directly absorbed by the eyeballs and moved *via* contact lens, which results in thermal damage to the eyeballs, thus producing cataracts. Alternatively, covering the contact lens with a graphene layer (Fig. 22b) caused moderate absorption of EM waves, therefore significantly avoiding thermal damage to the internal eyeballs. The experimental authentication of a resilient EM radiation contact lens (for normal and graphene coated) using the parameters of 120 W for 50 s is displayed in Fig. 22c. The results confirmed that the thermal denaturalization protected by the graphene-coated lenses was substantially lower compared to regular lenses.

Electrons in graphene produce oscillations when exposed to electromagnetic radiation, which absorb and discard the electromagnetic energy as heat energy. According to Fig. 22d, when a strong EM with a power of 120 W was illuminated on a graphene-coated contact lens (for 20 s), the temperature of the coated contact lens changed from room temperature (27 °C) to above 45 °C, and the temperature of the uncoated contact lens remained relatively constant.[403] Fig. 22e and f schematically illustrate that the application of lenses without the graphene coating causes the dehydration of eyeballs, which can result in xerophthalmia (Fig. 22e). In contrast, graphene lenses protect against dehydration (Fig. 22f). The dehydration protection of the graphene-coated contact lenses was validated by mounting the conventional and graphene lenses on water-filled vials. Subsequently, the vials were set on a heated plate at 38 °C (Fig. 22g). One week later, the weight of the vial with the graphene-coated lens decreased by 0.5535 g, while that with the conventional lens decreased by 0.8268 g. This indicates the suitability of graphene to be used as protective material against dehydration (Fig. 22h). Thus, graphene-coated lenses can screen electromagnetic interference and prevent dryness in the eyes. Also, they can be used as a bionic platform in smart technologies for biomedical and healthcare applications in the future.[406,407]

4   Challenges and prospects

4.1   Pertinent features and common limiting factors

2D materials offer a significant advantage for sensing applications due to their various characteristics. In addition to their outstanding physical and chemical characteristics, 2D materials have a high surface area-to-volume ratio, which is crucial for sensing applications. As a result of such surface- and volume-

free nature, high-performance sensing devices can be designed with maximum sensitivity by introducing various alterations 2D materials framework. Different 2D nanostructures undergo oxidation under ambient conditions, leading to structural changes and resulting in the decomposition of the material in some severe cases. Consequently, their application in functional devices is considerably limited. Thus, far out approaches are required to achieve substantial oxidative stability during the synthesis, storage, and practical applications of 2D materials. This can be realized by designing new 2D materials with improved oxidative and thermal stability. Correspondingly, the chemical tunability of 2D materials facilitates the fabrication of multi-component assemblies, which can enable multiplex or multi-analyte detection in a single device. In particular, the presence of free radicals (so-called dangling bonds) and better reactivity of 2D materials can elevate the sensing profile. Also, the non-selective binding of analytes ultimately results in poor selectivity, long response, or even incomplete recovery time. In this case, optical sensors (based on the variations in the PL characteristics of 2D materials following the antigen-analyte interactions with analytes) have been used successfully and extensively utilized for biological and metal-relevant molecules. Not least of all, Electrochemical sensors seem encouraging due to their feasible operations and rapid detection.

4.2   Role of defects

Pristine and/or defect-free sheets may not produce strong interactions with target analytes. Furthermore, defects play a critical role in 2D materials, where they enable bandgap engineering and offer modulation of optoelectronic/electronic characteristics. Moreover, defects increase the chemical reactivity of 2D materials, allowing the further chemical functionalization of their reactive sites, which results in higher sensitivity and a small LOD for target analytes. Conversely, the lack of control during defect engineering can produce enduring effects in 2D materials. The most important task to be initiated in the near future is the well-ordered incorporation of ad hoc defects in 2D materials with precise concentration and spatial resolution. Ideally, defect placement should be accompanied by chemical functionalization of reactive sites with a choice of analyte receptors. This can be achieved through a thorough understanding of the principles of molecular recognition. For example, this can be realized by modifying the supramolecular interactions that correspond to ultrasensitive 2D materials and improving the response time of sensors with higher selectivity, thus providing a clear path to industrial production.

4.3   Particular aspects of electrochemical sensing

Furthermore, it is essential to link the multi-dimensional aspects of 2D materials to electronic devices, *i.e.*, synergistically integrating multi-functionality. For example, the fabrication of porous conductive materials allows a synergistic connection with the surface, increased hydrophobicity, low resistance to charge transfer, and increased capacitance. These elements can enhance the operation of potentiometric devices.

6052 | *J. Mater. Chem. A*, 2023, **11**, 6016–6063

This journal is © The Royal Society of Chemistry 2023

Conversely, during antigen-analyte interactions, the coupling of magnetic exchange and electronic interactions in 2D materials can increase the charge transport perturbations. The evolution of these sensing technologies can lead to extraordinary advances in analytic modes, which include cost, simplicity, and superior sensing profile. The study of new 2D materials is still in its initial stages, and due to the exceptional diversity of these materials, it is possible to further consolidate their place in the field of electrical transduction sensors and nanoscience. Recently, the immense progress and development of 2D materials, including the graphene-based material family, MXene family, and TMDCs, are widely used in numerous devices, including strain and pressure sensors, flexible temperature sensors, and gas sensors (see Tables 1 and 2). Furthermore, industrial and commercial technologies may introduce these materials in the coming years. Generally, flexible electronics (Opto) with superior advances are considered attractive candidates for studying human physiological information, especially in wearable configurations for medical diagnosis and personalized health care. Similarly, some integrated electronics that can detect multiple signals to obtain detailed physiological information have also been examined.

4.4 Particular aspects of wearable systems

Graphene and other 2D materials offer outstanding electrical and mechanical properties (*e.g.*, flexibility and stiffness). Material-based 2D sensors can be supported on flexible sheets to fabricate smart wearable devices to monitor the environment/human interface. Furthermore, by integrating 2D materials with electrodes, van der Waals heterostructures from combining different 2D materials can improve the electrical contacts, material stability, and device performance. The fabrication of these heterostructure interfaces in sensing devices has the potential to improve the sensitivity, selectivity, and stability of sensors. Furthermore, developing multifunctional devices, physically and chemically integrated systems, will be a promising route toward accurately assessing physical conditions. Nevertheless, the simultaneous detection of chemical signals and large strain changes is a significant task due to their severe signal crosstalk. In addition, wearable chemical systems with a lower LOD, higher sensitivity, and exceptional selectivity for complex environments of the human body need to be addressed. Furthermore, combining two features, such as diagnosis and therapy, is an alternative operation path to extend their function and applications. Drug delivery and physical therapy (*i.e.*, electrical stimulation and hyperthermia) will be a favorable development as a medical treatment device. Although various research works verify the recovery of human physiological signals, the transition from fundamental research (from laboratories) to industrial products takes a long time. Signal processing with a flexible circuit board, low power consumption, and delicate and modest size should be approved through pragmatic cooperation with electronic engineers. Existing circuit technologies have been assembled using standard chips, which are unsuitable for some particular applications, for example, the chip introduced in a contact lens for intraocular pressure monitoring. In addition, small-scale loop devices with long standby life and working hours are crucial for the round-the-clock observation of human physiological information. To ensure the safety of wearable systems, medical professionals should evaluate the various signals detected by these devices. Additional valuable data can be identified by comparing the results to typical medical test results. Evaluations and long-term observation of human physiological signals will support data consistency, which is significant for impending personal health care. Furthermore, despite the substantial advances in assessing mechanical characteristics based on nanoindentation, the effect of unavoidable factors, such as sample damage during the laborious preparation and testing procedure are insignificant. Future research into 2D ultrathin nanomaterials still requires the development of new 2D materials, large-scale production of high-quality 2D crystals, and use of more accurate computational and experimental models for characterization and measurement. Recent evidence suggest 2D materials can work with "on-the-skin" applications paving the way for their application to detect clinically significant biomarkers. Consequently, these 2D material-based tattoos can be used as dry sensors on the skin with minimal sensitivity to motion artifacts, a significant shortcoming of conventional dry sensors and electrodes for point-of-care health monitoring.

4.5 Computational approaches for state-of-the-art sensor design

Computational evaluation coupled with curiosity-driven research can lead to numerous possibilities for the innovation in stimulus-sensitive 2D materials with significant functions in chemical sensing. The creation of computational models and their application in materials design and synthesis are the challenging long-term goals in this field. Consequently, we may see two critical methodologies in the future. Firstly, the open-loop design technique. The growth chamber design and synthesis settings are established by a series of simulations that reflect the experiment thermophysical circumstances, expected growth, and reaction kinetics. This method requires high model fidelity, and a thorough sensitivity analysis must be performed to produce a robust design. Secondly, the closed-loop design, where the models identify system states that are communicated to a controller that continuously changes the growing conditions in real-time. The effectiveness of the design in this technique critically depends on the computational capacity of the models. Future development of multianalyte detection can also be possible through chemical programmability by creating 2D material-based multi-component assemblies. However, current mathematical and numerical models are computationally expensive and often do not simultaneously capture all the physics involved in a 2D material growth process, thus limiting their general application in the active control of 2D material growth. The use of machine learning models trained using experimental and computational databases of 2D material structure and growth conditions, such as that accessible in the 2D Crystal Consortium-Materials Innovation Platform, is a promising technique to overcome this problem. Finally, the

This journal is © The Royal Society of Chemistry 2023

J. Mater. Chem. A, 2023, **11**, 6016–6063 | **6053**

models and methods used to understand the growth of 2D materials can be modified to understand the evolution of other materials using the same synthesis methods, such as thin-film CVD growth.

4.6 *In situ* and operando spectroscopic techniques for mechanism understanding

In situ and operando spectroscopic techniques are considered state-of-the-art tools for learning the operating principles and processes involved in gas sensing. A combination of ion-sorption, oxygen vacancy, and charge transfer models can provide insight into the sensing mechanisms of chemiresistive gases. Understanding the precise sensing processes of these types of sensor devices using spectroscopic methods in various modes of operation can aid in constructing high-performance intelligent sensor devices. Moreover, extensive theoretical studies are needed to validate the experimental results of operando spectroscopic studies. The benefits of different operando spectroscopic studies and theoretical analyses are thought to provide more information on sensing devices and aid in designing high-performance gas sensors. The use of luminous 2D materials has great potential in biological sensing and imaging applications. The large surface area of 2D materials can function as a platform for multiplex sensing, another potential untapped application. Furthermore, although sensors are performing well in research and development, a satisfactory result for sensor devices has not been achieved thus far. Future research should focus on solving some of these problems and creating reliable, cheap, and environmentally friendly chemical sensors with extremely high selectivity and sensitivity. Another expansion path is sensor technology with portable capabilities.

4.7 Concluding remarks, critical comments, and industrial aspects

Convincingly, 2D materials have significant properties in terms of sensing. However, multidisciplinary efforts and cutting-edge research are required to realize their full potential. Further development in this field can be achieved through innovations in the design of 2D materials. The roadmap for developing and discovering 2D materials is progressing rapidly; however, some 2D materials still have to be fully revealed as candidates for chemical sensing. New sensing platforms are revealed every year, and the industry is developing rapidly. Multiplatform sensing using a combination of different materials is the next frontier. Crosslinked heterostructures, which produce distinctive properties that their single 2D equivalents cannot achieve, can be formed not only for 2D-2D blocks but also with other low-dimensional materials. Compared to conventional materials, 2D materials have emerged as the most promising materials for technological applications due to their unique piezoelectric, photoelectric, and mechanical capabilities. In this case, understanding the active sensing physicochemical properties and interactions of the material is crucial to comprehend its sensing mechanisms. The detailed operating principles behind gas sensing devices should be evaluated through rigorous explanation of their physical and synthetic characteristics,

including the functionality of sensing materials and their interactions with analyte gas molecules. This can enable the development of optimal high-performance sensor systems. However, there is still a great deal of work to be done on defining the exact sensing mechanisms of these newly discovered materials. Several techniques have been proven to be effective in tuning the gas-sensing properties of 2D materials.

In addition, two-dimensional self-powered sensors are considered to have a wide range of applications in biomedicine, environmental sensing, motion tracking, energy harvesting, and smart wearables. Recently, self-powered nanosensors (TENG/PENG) have emerged as a new form of sensors. These devices use nano-effects to ensure continuous operation by harvesting and using energy from the environment. Recent advances in TENG/PENG as a new mechanical energy conversion technology have demonstrated their potential towards self-powered sensors/electronics and micro/nano power sources. They are ideal for portable electronic devices, self-driving micro-nano systems, and the next generation of IoT devices. These sensors offer a variety of benefits, including precision, energy harvesting, biomedical engineering, environmental monitoring, artificial intelligence, and neuromorphic computing. Because graphene has high thermal conductivity and a negative thermal expansion coefficient, studies on its thermal properties are becoming increasingly crucial for graphene-based self-powered sensors. The development of 2D material-based self-powered NG sensors is still in its early stages, and further studies are required to select and optimize 2D materials and design optimization. A growing number of 2D materials are being discovered, resulting in the greater use of 2D self-powered sensors for human monitoring, energy harvesting, biomedicine, and artificial intelligence.

The Internet of Things (IoT) is at the heart of the global information industry. Sensors have become common due to their high integration, simplicity, portability, and ease of commercialization. Together with its advancement, IoT also faces many technological challenges. One example is sensors, which have become the most significant obstacle in the growth of IoT. Although small-scale applications can reduce the power consumption to microwatts, large-scale applications can result in surprising power consumption, resulting in a shorter shelf life and environmental contamination.

Primarily, the study on 2D materials has lasted 19 years since their first report (*e.g.*, graphene). All the literature on this subject leads the way and ousts any doubts about their potential use in sensing applications. However, currently fewer products on the market that contain 2D materials. While challenging, the long-term goal of researchers is commercializing the sensing devices based on 2D materials. However, 2D material deposition and growth at the wafer scale may be appropriate. Nevertheless, contamination and defects still do not fully comply with industry standards for manufacturing. Accordingly, reliable product design, scalability, and low-cost manufacturing are essential features to consider from an industrial perspective and market competition. Due to the manufacturing limitation for effective 2D materials, various complicated procedures have been widely implemented, disrupting their subsequent

6054 | *J. Mater. Chem. A*, 2023, **11**, 6016–6063

This journal is © The Royal Society of Chemistry 2023

practical applications. Additionally, large-scale manufacturing techniques are needed for low-cost, scalable systems. By thoroughly analyzing 2D-based sensing devices and the challenges involved, this review paper aimed to provide readers with a better understanding of the fundamental research and academia-industry connections.

Conflicts of interest

The authors declare no conflict of interest.

Acknowledgements

References

1 K. S. Novoselov, A. K. Geim, S. V. Morozov, D. Jiang, M. I. Katsnelson, I. V. Grigorieva, S. V. Dubonos and A. A. Firsov, *Nature*, 2005, **438**, 197–200.

2 A. C. Ferrari, F. Bonaccorso, V. Fal'ko, K. S. Novoselov, S. Roche, P. Bøggild, S. Borini, F. H. L. Koppens, V. Palermo, N. Pugno, J. A. Garrido, R. Sordan, A. Bianco, L. Ballerini, M. Prato, E. Lidorikis, J. Kivioja, C. Marinelli, T. Ryhänen, A. Morpurgo, J. N. Coleman, V. Nicolosi, L. Colombo, A. Fert, M. Garcia-Hernandez, A. Bachtold, G. F. Schneider, F. Guinea, C. Dekker, M. Barbone, Z. Sun, C. Galiotis, A. N. Grigorenko, G. Konstantatos, A. Kis, M. Katsnelson, L. Vandersypen, A. Loiseau, V. Morandi, D. Neumaier, E. Treossi, V. Pellegrini, M. Polini, A. Tredicucci, G. M. Williams, B. Hee Hong, J.-H. Ahn, J. Min Kim, H. Zirath, B. J. van Wees, H. van der Zant, L. Occhipinti, A. Di Matteo, I. A. Kinloch, T. Seyller, E. Quesnel, X. Feng, K. Teo, N. Rupesinghe, P. Hakonen, S. R. T. Neil, Q. Tannock, T. Löfwander and J. Kinaret, *Nanoscale*, 2015, **7**, 4598–4810.

3 M. Chakraborty and M. S. J. Hashmi, *Adv. Mater. Process. Technol.*, 2018, **4**, 573–602.

4 M. J. Molaei, M. Younas and M. Rezakazemi, *ACS Appl. Electron. Mater.*, 2021, **3**, 5165–5187.

5 M. W. Barsoum, *Prog. Solid State Chem.*, 2000, **28**, 201–281.

6 Q. H. Wang, K. Kalantar-Zadeh, A. Kis, J. N. Coleman and M. S. Strano, *Nat. Nanotechnol.*, 2012, **7**, 699–712.

7 L. Li, Y. Yu, G. J. Ye, Q. Ge, X. Ou, H. Wu, D. Feng, X. H. Chen and Y. Zhang, *Nat. Nanotechnol.*, 2014, **9**, 372–377.

8 H. Liu, A. T. Neal, Z. Zhu, Z. Luo, X. Xu, D. Tománek and P. D. Ye, *ACS Nano*, 2014, **8**, 4033–4041.

9 A. Raza, U. Qumar, A. A. Rafi and M. Ikram, *Sustainable Mater. Technol.*, 2022, **33**, e00462.

10 A. Gupta, T. Sakthivel and S. Seal, *Prog. Mater. Sci.*, 2015, **73**, 44–126.

11 A. S. Mayorov, R. V. Gorbachev, S. V. Morozov, L. Britnell, R. Jalil, L. A. Ponomarenko, P. Blake, K. S. Novoselov, K. Watanabe, T. Taniguchi and A. K. Geim, *Nano Lett.*, 2011, **11**, 2396–2399.

12 C. Schneider, M. M. Glazov, T. Korn, S. Höfling and B. Urbaszek, *Nat. Commun.*, 2018, **9**, 2695.

13 N. Zibouche, P. Philipsen, A. Kuc and T. Heine, *Phys. Rev. B: Condens. Matter Mater. Phys.*, 2014, **90**, 125440.

14 J. Wang, I. Verzhbitskiy and G. Eda, *Adv. Mater.*, 2018, **30**, 1802687.

15 M. Long, P. Wang, H. Fang and W. Hu, *Adv. Funct. Mater.*, 2019, **29**, 1803807.

16 X. Cao, C. Ding, C. Zhang, W. Gu, Y. Yan, X. Shi and Y. Xian, *J. Mater. Chem. B*, 2018, **6**, 8011–8036.

17 A. Daus, S. Vaziri, V. Chen, Ç. Köroğlu, R. W. Grady, C. S. Bailey, H. R. Lee, K. Schauble, K. Brenner and E. Pop, *Nat. Electron.*, 2021, **4**, 495–501.

18 A. Shahin, K. Ibrahim, F. Ye, R. Karimi, J. Sanderson and K. P. Musselman, *Sens. Actuators, B*, 2022, **359**, 131576.

19 R. Kumar, N. Goel, M. Hojamberdiev and M. Kumar, *Sens. Actuators, A*, 2020, **303**, 111875.

20 Y. Hu, Y. Huang, C. Tan, X. Zhang, Q. Lu, M. Sindoro, X. Huang, W. Huang, L. Wang and H. Zhang, *Mater. Chem. Front.*, 2017, **1**, 24–36.

21 L.-x. Yu and R.-t. Lv, *New Carbon Mater.*, 2021, **36**, 995–1012.

22 M. Pumera and A. H. Loo, *TrAC, Trends Anal. Chem.*, 2014, **61**, 49–53.

23 U. Qumar, J. Z. Hassan, R. A. Bhatti, A. Raza, G. Nazir, W. Nabgan and M. Ikram, *J. Mater. Sci. Technol.*, 2022, **131**, 122–166.

24 C. Anichini, W. Czepa, D. Pakulski, A. Aliprandi, A. Ciesielski and P. Samorì, *Chem. Soc. Rev.*, 2018, **47**, 4860–4908.

25 C. Zhu, Z. Zeng, H. Li, F. Li, C. Fan and H. Zhang, *J. Am. Chem. Soc.*, 2013, **135**, 5998–6001.

26 D. Dinda, A. Gupta, B. K. Shaw, S. Sadhu and S. K. Saha, *ACS Appl. Mater. Interfaces*, 2014, **6**, 10722–10728.

27 A. Raza, Y. Zhang, A. Cassinese and G. Li, *Catalysts*, 2022, **12**, 1613.

28 J. Z. Hassan, A. Raza, U. Qumar and G. Li, *Sustainable Mater. Technol.*, 2022, **33**, e00478.

29 F. K. Perkins, A. L. Friedman, E. Cobas, P. M. Campbell, G. G. Jernigan and B. T. Jonker, *Nano Lett.*, 2013, **13**, 668–673.

30 C. Yim, K. Lee, N. McEvoy, M. O'Brien, S. Riazimehr, N. C. Berner, C. P. Cullen, J. Kotakoski, J. C. Meyer, M. C. Lemme and G. S. Duesberg, *ACS Nano*, 2016, **10**, 9550–9558.

31 Y. Liu, M. Pharr and G. A. Salvatore, *ACS Nano*, 2017, **11**, 9614–9635.

32 Y. Zang, F. Zhang, C.-a. Di and D. Zhu, *Mater. Horiz.*, 2015, **2**, 140–156.

33 S. Xu, Y. Zhang, L. Jia, E. Mathewson Kyle, K.-I. Jang, J. Kim, H. Fu, X. Huang, P. Chava, R. Wang, S. Bhole, L. Wang, J. Na Yoon, Y. Guan, M. Flavin, Z. Han, Y. Huang and A. Rogers John, *Science*, 2014, **344**, 70–74.

34 T. Yamada, Y. Hayamizu, Y. Yamamoto, Y. Yomogida, A. Izadi-Najafabadi, D. N. Futaba and K. Hata, *Nat. Nanotechnol.*, 2011, **6**, 296–301.

35 S. Chen, Y. Song, D. Ding, Z. Ling and F. Xu, *Adv. Funct. Mater.*, 2018, **28**, 1802547.

This journal is © The Royal Society of Chemistry 2023

J. Mater. Chem. A, 2023, **11**, 6016–6063 | **6055**

36 W. Gao, S. Emaminejad, H. Y. Y. Nyein, S. Challa, K. Chen, A. Peck, H. M. Fahad, H. Ota, H. Shiraki, D. Kiriya, D.-H. Lien, G. A. Brooks, R. W. Davis and A. Javey, *Nature*, 2016, **529**, 509–514.

37 A. J. Bandodkar, I. Jeerapan and J. Wang, *ACS Sens.*, 2016, **1**, 464–482.

38 Z. Meng, R. M. Stolz, L. Mendecki and K. A. Mirica, *Chem. Rev.*, 2019, **119**, 478–598.

39 Y. Pang, Z. Yang, Y. Yang and T.-L. Ren, *Small*, 2020, **16**, 1901124.

40 N. Rohaizad, C. C. Mayorga-Martinez, M. Fojtů, N. M. Latiff and M. Pumera, *Chem. Soc. Rev.*, 2021, **50**, 619–657.

41 K. Khan, A. K. Tareen, L. Wang, M. Aslam, C. Ma, N. Mahmood, Z. Ouyang, H. Zhang and Z. Guo, *Adv. Funct. Mater.*, 2021, **31**, 2005957.

42 A. Majed, M. Kothakonda, F. Wang, E. N. Tseng, K. Prenger, X. Zhang, P. O. Å. Persson, J. Wei, J. Sun and M. Naguib, *Adv. Mater.*, 2022, **34**, 2200574.

43 Z. Guo, J. Zhou and Z. Sun, *J. Mater. Chem. A*, 2017, **5**, 23530–23535.

44 H. Zhang, H. Xiang, F.-z. Dai, Z. Zhang and Y. Zhou, *J. Mater. Sci. Technol.*, 2018, **34**, 2022–2026.

45 M. Dahri, A. Miri Jahromi, A. Nikzad, M. Mohammadgholian, M. Rahmanian, S. S. Abolmaali and R. Maleki, *J. Biomol. Struct. Dyn.*, 2021, 1–9, DOI: 10.1080/07391102.2021.1969288.

46 M. Naguib, M. Kurtoglu, V. Presser, J. Lu, J. Niu, M. Heon, L. Hultman, Y. Gogotsi and M. W. Barsoum, *Adv. Mater.*, 2011, **23**, 4248–4253.

47 F. Wang, C. Yang, C. Duan, D. Xiao, Y. Tang and J. Zhu, *J. Electrochem. Soc.*, 2014, **162**, B16–B21.

48 H. Lin, X. Wang, L. Yu, Y. Chen and J. Shi, *Nano Lett.*, 2017, **17**, 384–391.

49 K. S. Novoselov, A. K. Geim, S. V. Morozov, D. Jiang, Y. Zhang, S. V. Dubonos, I. V. Grigorieva and A. A. Firsov, *Science*, 2004, **306**, 666–669.

50 N. Mohanty and V. Berry, *Nano Lett.*, 2008, **8**, 4469–4476.

51 Z. Liu, J. T. Robinson, X. Sun and H. Dai, *J. Am. Chem. Soc.*, 2008, **130**, 10876–10877.

52 Y. Hernandez, V. Nicolosi, M. Lotya, F. M. Blighe, Z. Sun, S. De, I. T. McGovern, B. Holland, M. Byrne, Y. K. Gun'Ko, J. J. Boland, P. Niraj, G. Duesberg, S. Krishnamurthy, R. Goodhue, J. Hutchison, V. Scardaci, A. C. Ferrari and J. N. Coleman, *Nat. Nanotechnol.*, 2008, **3**, 563–568.

53 P. Joensen, R. F. Frindt and S. R. Morrison, *Mater. Res. Bull.*, 1986, **21**, 457–461.

54 J. N. Coleman, M. Lotya, A. O'Neill, S. D. Bergin, P. J. King, U. Khan, K. Young, A. Gaucher, S. De, R. J. Smith, I. V. Shvets, S. K. Arora, G. Stanton, H.-Y. Kim, K. Lee, G. T. Kim, G. S. Duesberg, T. Hallam, J. J. Boland, J. J. Wang, J. F. Donegan, J. C. Grunlan, G. Moriarty, A. Shmeliov, R. J. Nicholls, J. M. Perkins, E. M. Grieveson, K. Theuwissen, D. W. McComb, P. D. Nellist and V. Nicolosi, *Science*, 2011, **331**, 568–571.

55 H. Li, Z. Yin, Q. He, H. Li, X. Huang, G. Lu, D. W. H. Fam, A. I. Y. Tok, Q. Zhang and H. Zhang, *Small*, 2012, **8**, 63–67.

56 S. S. Chou, B. Kaehr, J. Kim, B. M. Foley, M. De, P. E. Hopkins, J. Huang, C. J. Brinker and V. P. Dravid, *Angew. Chem., Int. Ed.*, 2013, **52**, 4160–4164.

57 J. Li, X.-Y. Wang, X.-R. Liu, Z. Jin, D. Wang and L.-J. Wan, *J. Mater. Chem. C*, 2015, **3**, 3530–3535.

58 I. V. Vlassiouk, Y. Stehle, P. R. Pudasaini, R. R. Unocic, P. D. Rack, A. P. Baddorf, I. N. Ivanov, N. V. Lavrik, F. List, N. Gupta, K. V. Bets, B. I. Yakobson and S. N. Smirnov, *Nat. Mater.*, 2018, **17**, 318–322.

59 A. H. Castro Neto, F. Guinea, N. M. R. Peres, K. S. Novoselov and A. K. Geim, *Rev. Mod. Phys.*, 2009, **81**, 109–162.

60 Q. He, S. Wu, Z. Yin and H. Zhang, *Chem. Sci.*, 2012, **3**, 1764–1772.

61 L. H. Li and Y. Chen, *Adv. Funct. Mater.*, 2016, **26**, 2594–2608.

62 M. Chhowalla, H. S. Shin, G. Eda, L.-J. Li, K. P. Loh and H. Zhang, *Nat. Chem.*, 2013, **5**, 263–275.

63 K. Kalantar-zadeh, J. Z. Ou, T. Daeneke, A. Mitchell, T. Sasaki and M. S. Fuhrer, *Appl. Mater. Today*, 2016, **5**, 73–89.

64 L. Sun, M. G. Campbell and M. Dincă, *Angew. Chem., Int. Ed.*, 2016, **55**, 3566–3579.

65 E. Jin, M. Asada, Q. Xu, S. Dalapati, A. Addicoat Matthew, A. Brady Michael, H. Xu, T. Nakamura, T. Heine, Q. Chen and D. Jiang, *Science*, 2017, **357**, 673–676.

66 C. Tan, X. Cao, X.-J. Wu, Q. He, J. Yang, X. Zhang, J. Chen, W. Zhao, S. Han, G.-H. Nam, M. Sindoro and H. Zhang, *Chem. Rev.*, 2017, **117**, 6225–6331.

67 F. Bonaccorso, L. Colombo, G. Yu, M. Stoller, V. Tozzini, A. C. Ferrari, R. S. Ruoff and V. Pellegrini, *Science*, 2015, **347**, 1246501.

68 J. H. Gosling, O. Makarovsky, F. Wang, N. D. Cottam, M. T. Greenaway, A. Patanè, R. D. Wildman, C. J. Tuck, L. Turyanska and T. M. Fromhold, *Commun. Phys.*, 2021, **4**, 30.

69 Y. Zhang, J. P. Small, W. V. Pontius and P. Kim, *Appl. Phys. Lett.*, 2005, **86**, 073104.

70 A. Chaves, J. G. Azadani, H. Alsalman, D. R. da Costa, R. Frisenda, A. J. Chaves, S. H. Song, Y. D. Kim, D. He, J. Zhou, A. Castellanos-Gomez, F. M. Peeters, Z. Liu, C. L. Hinkle, S.-H. Oh, P. D. Ye, S. J. Koester, Y. H. Lee, P. Avouris, X. Wang and T. Low, *npj 2D Mater. Appl.*, 2020, **4**, 29.

71 S. Manzeli, D. Ovchinnikov, D. Pasquier, O. V. Yazyev and A. Kis, *Nat. Rev. Mater.*, 2017, **2**, 17033.

72 K. F. Mak, C. Lee, J. Hone, J. Shan and T. F. Heinz, *Phys. Rev. Lett.*, 2010, **105**, 136805.

73 S. Barua, H. S. Dutta, S. Gogoi, R. Devi and R. Khan, *ACS Appl. Nano Mater.*, 2018, **1**, 2–25.

74 D. Le, T. B. Rawal and T. S. Rahman, *J. Phys. Chem. C*, 2014, **118**, 5346–5351.

75 S. Ali, A. Raza, A. M. Afzal, M. W. Iqbal, M. Hussain, M. Imran and M. A. Assiri, *Adv. Mater. Interfaces*, 2022, **9**, 2200556.

76 A. Bolotsky, D. Butler, C. Dong, K. Gerace, N. R. Glavin, C. Muratore, J. A. Robinson and A. Ebrahimi, *ACS Nano*, 2019, **13**, 9781–9810.

6056 | *J. Mater. Chem. A*, 2023, **11**, 6016–6063

This journal is © The Royal Society of Chemistry 2023

77 Y. Wang, Y. Shao, D. W. Matson, J. Li and Y. Lin, *ACS Nano*, 2010, **4**, 1790–1798.

78 K. Kalantar-zadeh and J. Z. Ou, *ACS Sens.*, 2016, **1**, 5–16.

79 Z. Li and S. L. Wong, *Mater. Sci. Eng., C*, 2017, **70**, 1095–1106.

80 A. Hirsch and F. Hauke, *Angew. Chem., Int. Ed.*, 2018, **57**, 4338–4354.

81 V. Georgakilas, J. N. Tiwari, K. C. Kemp, J. A. Perman, A. B. Bourlinos, K. S. Kim and R. Zboril, *Chem. Rev.*, 2016, **116**, 5464–5519.

82 G. Reina, J. M. González-Domínguez, A. Criado, E. Vázquez, A. Bianco and M. Prato, *Chem. Soc. Rev.*, 2017, **46**, 4400–4416.

83 J. Wan, S. D. Lacey, J. Dai, W. Bao, M. S. Fuhrer and L. Hu, *Chem. Soc. Rev.*, 2016, **45**, 6742–6765.

84 Y. Xu, X. Xie, R. Zhang and W. Yuan, *Sens. Actuators, B*, 2022, **372**, 132670.

85 S. Eissa, G. C. Jimenez, F. Mahvash, A. Guermoune, C. Tlili, T. Szkopek, M. Zourob and M. Siaj, *Nano Res.*, 2015, **8**, 1698–1709.

86 F. Khurshid, M. Jeyavelan, K. Takahashi, M. S. Leo Hudson and S. Nagarajan, *RSC Adv.*, 2018, **8**, 20440–20449.

87 M. V. Sulleiro, A. Dominguez-Alfaro, N. Alegret, A. Silvestri and I. J. Gómez, *Sens. Bio-Sens. Res.*, 2022, **38**, 100540.

88 M. Zeng, Y. Xiao, J. Liu, K. Yang and L. Fu, *Chem. Rev.*, 2018, **118**, 6236–6296.

89 F. Schedin, A. K. Geim, S. V. Morozov, E. W. Hill, P. Blake, M. I. Katsnelson and K. S. Novoselov, *Nat. Mater.*, 2007, **6**, 652–655.

90 A. Nag, A. Mitra and S. C. Mukhopadhyay, *Sens. Actuators, A*, 2018, **270**, 177–194.

91 J. Martincová, M. Otyepka and P. Lazar, *Chem.–Eur. J.*, 2017, **23**, 13233–13239.

92 J. Gao, B. Li, J. Tan, P. Chow, T.-M. Lu and N. Koratkar, *ACS Nano*, 2016, **10**, 2628–2635.

93 J.-W. Jiang, *Front. Phys.*, 2015, **10**, 287–302.

94 J. Yoon, J. Lim, M. Shin, S.-N. Lee and J.-W. Choi, *Materials*, 2021, **14**, 518.

95 Z. U. D. Babar, B. Della Ventura, R. Velotta and V. Iannotti, *RSC Adv.*, 2022, **12**, 19590–19610.

96 K. Khan, J. Li, W. Zou, W. Xu, Y. Yang and W. Song, *J. Wuhan Univ. Technol., Mater. Sci. Ed.*, 2016, **31**, 1201–1205.

97 K. Khan, A. K. Tareen, M. Aslam, Y. Zhang, R. Wang, Z. Ouyang, Z. Gou and H. Zhang, *Nanoscale*, 2019, **11**, 21622–21678.

98 A. J. Mannix, X.-F. Zhou, B. Kiraly, J. D. Wood, D. Alducin, B. D. Myers, X. Liu, B. L. Fisher, U. Santiago, J. R. Guest, M. J. Yacaman, A. Ponce, A. R. Oganov, M. C. Hersam and N. P. Guisinger, *Science*, 2015, **350**, 1513–1516.

99 B. Feng, J. Zhang, R.-Y. Liu, T. Iimori, C. Lian, H. Li, L. Chen, K. Wu, S. Meng, F. Komori and I. Matsuda, *Phys. Rev. B*, 2016, **94**, 041408.

100 Y. Wang, J. Fan and M. Trenary, *Chem. Mater.*, 1993, **5**, 192–198.

101 F. Xia, H. Wang, D. Xiao, M. Dubey and A. Ramasubramaniam, *Nat. Photonics*, 2014, **8**, 899–907.

102 C. R. Dean, A. F. Young, I. Meric, C. Lee, L. Wang, S. Sorgenfrei, K. Watanabe, T. Taniguchi, P. Kim, K. L. Shepard and J. Hone, *Nat. Nanotechnol.*, 2010, **5**, 722–726.

103 X. Huang, P. Sheng, Z. Tu, F. Zhang, J. Wang, H. Geng, Y. Zou, C.-a. Di, Y. Yi, Y. Sun, W. Xu and D. Zhu, *Nat. Commun.*, 2015, **6**, 7408.

104 W. Bao, X. Cai, D. Kim, K. Sridhara and M. S. Fuhrer, *Appl. Phys. Lett.*, 2013, **102**, 042104.

105 D. J. Perello, S. H. Chae, S. Song and Y. H. Lee, *Nat. Commun.*, 2015, **6**, 7809.

106 Y. Wang, Y. Chen, S. D. Lacey, L. Xu, H. Xie, T. Li, V. A. Danner and L. Hu, *Mater. Today*, 2018, **21**, 186–192.

107 X. Yang, C. Shang, S. Zhou and J. Zhao, *Nanoscale Horiz.*, 2020, **5**, 1106–1115.

108 C. Zhang, B. Anasori, A. Seral-Ascaso, S.-H. Park, N. McEvoy, A. Shmeliov, G. S. Duesberg, J. N. Coleman, Y. Gogotsi and V. Nicolosi, *Adv. Mater.*, 2017, **29**, 1702678.

109 K. Hantanasirisakul, M.-Q. Zhao, P. Urbankowski, J. Halim, B. Anasori, S. Kota, C. E. Ren, M. W. Barsoum and Y. Gogotsi, *Adv. Electron. Mater.*, 2016, **2**, 1600050.

110 X. Jiang, A. V. Kuklin, A. Baev, Y. Ge, H. Ågren, H. Zhang and P. N. Prasad, *Phys. Rep.*, 2020, **848**, 1–58.

111 I. R. Shein and A. L. Ivanovskii, *Comput. Mater. Sci.*, 2012, **65**, 104–114.

112 C. J. Zhang, S. Pinilla, N. McEvoy, C. P. Cullen, B. Anasori, E. Long, S.-H. Park, A. Seral-Ascaso, A. Shmeliov, D. Krishnan, C. Morant, X. Liu, G. S. Duesberg, Y. Gogotsi and V. Nicolosi, *Chem. Mater.*, 2017, **29**, 4848–4856.

113 M. Mozafari and M. Soroush, *Mater. Adv.*, 2021, **2**, 7277–7307.

114 S. Kumar, Y. Lei, N. H. Alshareef, M. A. Quevedo-Lopez and K. N. Salama, *Biosens. Bioelectron.*, 2018, **121**, 243–249.

115 W. Y. Chen, S.-N. Lai, C.-C. Yen, X. Jiang, D. Peroulis and L. A. Stanciu, *ACS Nano*, 2020, **14**, 11490–11501.

116 J. Huang, Z. Li, Y. Mao and Z. Li, *Nano Sel.*, 2021, **2**, 1480–1508.

117 H. Lin, Y. Chen and J. Shi, *Adv. Sci.*, 2018, **5**, 1800518.

118 Y. Pei, X. Zhang, Z. Hui, J. Zhou, X. Huang, G. Sun and W. Huang, *ACS Nano*, 2021, **15**, 3996–4017.

119 L. Chen, X. Dai, W. Feng and Y. Chen, *Acc. Mater. Res.*, 2022, **3**, 785–798.

120 J. Wang, F. Ma, W. Liang and M. Sun, *Mater. Today Phys.*, 2017, **2**, 6–34.

121 X. Huang, Z. Yin, S. Wu, X. Qi, Q. He, Q. Zhang, Q. Yan, F. Boey and H. Zhang, *Small*, 2011, **7**, 1876–1902.

122 Y. Zhang, T.-T. Tang, C. Girit, Z. Hao, M. C. Martin, A. Zettl, M. F. Crommie, Y. R. Shen and F. Wang, *Nature*, 2009, **459**, 820–823.

123 C.-N. Yeh, K. Raidongia, J. Shao, Q.-H. Yang and J. Huang, *Nat. Chem.*, 2015, **7**, 166–170.

124 T. Kuila, S. Bose, P. Khanra, A. K. Mishra, N. H. Kim and J. H. Lee, *Biosens. Bioelectron.*, 2011, **26**, 4637–4648.

125 V. Georgakilas, M. Otyepka, A. B. Bourlinos, V. Chandra, N. Kim, K. C. Kemp, P. Hobza, R. Zboril and K. S. Kim, *Chem. Rev.*, 2012, **112**, 6156–6214.

This journal is © The Royal Society of Chemistry 2023

J. Mater. Chem. A, 2023, **11**, 6016–6063 | **6057**

126 R. Zhou and H. Gao, *WIREs Nanomedicine and Nanobiotechnology*, 2014, **6**, 452–474.

127 S. Syama and P. V. Mohanan, *Int. J. Biol. Macromol.*, 2016, **86**, 546–555.

128 S. Pattnaik, K. Swain and Z. Lin, *J. Mater. Chem. B*, 2016, **4**, 7813–7831.

129 B. Radisavljevic, A. Radenovic, J. Brivio, V. Giacometti and A. Kis, *Nat. Nanotechnol.*, 2011, **6**, 147–150.

130 G. H. Jeong, S. P. Sasikala, T. Yun, G. Y. Lee, W. J. Lee and S. O. Kim, *Adv. Mater.*, 2020, **32**, 1907006.

131 L. Nurdiwijayanto, R. Ma, N. Sakai and T. Sasaki, *Inorg. Chem.*, 2017, **56**, 7620–7623.

132 D.-W. Lee, J. Lee, I. Y. Sohn, B.-Y. Kim, Y. M. Son, H. Bark, J. Jung, M. Choi, T. H. Kim, C. Lee and N.-E. Lee, *Nano Res.*, 2015, **8**, 2340–2350.

133 J. H. Appel, D. O. Li, J. D. Podlevsky, A. Debnath, A. A. Green, Q. H. Wang and J. Chae, *ACS Biomater. Sci. Eng.*, 2016, **2**, 361–367.

134 H. Hu, A. Zavabeti, H. Quan, W. Zhu, H. Wei, D. Chen and J. Z. Ou, *Biosens. Bioelectron.*, 2019, **142**, 111573.

135 L. Wang, D. Xu, L. Jiang, J. Gao, Z. Tang, Y. Xu, X. Chen and H. Zhang, *Adv. Funct. Mater.*, 2021, **31**, 2004408.

136 Y. Xiao, Y. Li, Z. Guo, C. Tang, B. Sa, N. Miao, J. Zhou and Z. Sun, *Appl. Surf. Sci.*, 2021, **566**, 150634.

137 G. Yildiz, M. Bolton-Warberg and F. Awaja, *Acta Biomater.*, 2021, **131**, 62–79.

138 L. J. Hubble, J. S. Cooper, A. Sosa-Pintos, H. Kiiveri, E. Chow, M. S. Webster, L. Wieczorek and B. Raguse, *ACS Comb. Sci.*, 2015, **17**, 120–129.

139 B. Raguse, E. Chow, C. S. Barton and L. Wieczorek, *Anal. Chem.*, 2007, **79**, 7333–7339.

140 C. E. Davis, C. K. Ho, R. C. Hughes and M. L. Thomas, *Sens. Actuators, B*, 2005, **104**, 207–216.

141 Y. Liu, J. Parisi, X. Sun and Y. Lei, *J. Mater. Chem. A*, 2014, **2**, 9919–9943.

142 S. Ammu, V. Dua, S. R. Agnihotra, S. P. Surwade, A. Phulgirkar, S. Patel and S. K. Manohar, *J. Am. Chem. Soc.*, 2012, **134**, 4553–4556.

143 J. D. Fowler, M. J. Allen, V. C. Tung, Y. Yang, R. B. Kaner and B. H. Weiller, *ACS Nano*, 2009, **3**, 301–306.

144 B. Cho, M. G. Hahm, M. Choi, J. Yoon, A. R. Kim, Y.-J. Lee, S.-G. Park, J.-D. Kwon, C. S. Kim, M. Song, Y. Jeong, K.-S. Nam, S. Lee, T. J. Yoo, C. G. Kang, B. H. Lee, H. C. Ko, P. M. Ajayan and D.-H. Kim, *Sci. Rep.*, 2015, **5**, 8052.

145 H. Wohltjen, *Sens. Actuators*, 1984, **5**, 307–325.

146 R. Arsat, M. Breedon, M. Shafiei, P. G. Spizziri, S. Gilje, R. B. Kaner, K. Kalantar-zadeh and W. Wlodarski, *Chem. Phys. Lett.*, 2009, **467**, 344–347.

147 A. J. Ricco, S. J. Martin and T. E. Zipperian, *Sens. Actuators*, 1985, **8**, 319–333.

148 W. P. Jakubik, M. W. Urbańczyk, S. Kochowski and J. Bodzenta, *Sens. Actuators, B*, 2002, **82**, 265–271.

149 W. Yang, L. Gan, H. Li and T. Zhai, *Inorg. Chem. Front.*, 2016, **3**, 433–451.

150 B. Kumar, K. Min, M. Bashirzadeh, A. B. Farimani, M. H. Bae, D. Estrada, Y. D. Kim, P. Yasaei, Y. D. Park, E. Pop, N. R. Aluru and A. Salehi-Khojin, *Nano Lett.*, 2013, **13**, 1962–1968.

151 W. Xuan, M. He, N. Meng, X. He, W. Wang, J. Chen, T. Shi, T. Hasan, Z. Xu, Y. Xu and J. K. Luo, *Sci. Rep.*, 2014, **4**, 7206.

152 G. Korotcenkov and B. K. Cho, *Sens. Actuators, B*, 2013, **188**, 709–728.

153 G. Di Francia, B. Alfano and V. La Ferrara, *J. Sens.*, 2009, **2009**, 659275.

154 L. Zhang, K. Khan, J. Zou, H. Zhang and Y. Li, *Adv. Mater. Interfaces*, 2019, **6**, 1901329.

155 G. Korotcenkov, *Mater. Sci. Eng., B*, 2007, **139**, 1–23.

156 C. Wang, L. Yin, L. Zhang, D. Xiang and R. Gao, *Sensors*, 2010, **10**, 2088–2106.

157 H. Yang, J. Heo, S. Park, J. Song Hyun, H. Seo David, K.-E. Byun, P. Kim, I. Yoo, H.-J. Chung and K. Kim, *Science*, 2012, **336**, 1140–1143.

158 A. Singh, M. A. Uddin, T. Sudarshan and G. Koley, *Small*, 2014, **10**, 1555–1565.

159 B. P. Luther, S. D. Wolter and S. E. Mohney, *Sens. Actuators, B*, 1999, **56**, 164–168.

160 B. Liu, L. Chen, G. Liu, A. N. Abbas, M. Fathi and C. Zhou, *ACS Nano*, 2014, **8**, 5304–5314.

161 Y. Kim, S.-K. Kang, N.-C. Oh, H.-D. Lee, S.-M. Lee, J. Park and H. Kim, *ACS Appl. Mater. Interfaces*, 2019, **11**, 38902–38909.

162 T. Pham, G. Li, E. Bekyarova, M. E. Itkis and A. Mulchandani, *ACS Nano*, 2019, **13**, 3196–3205.

163 A. Liu, S. Lv, L. Jiang, F. Liu, L. Zhao, J. Wang, X. Hu, Z. Yang, J. He, C. Wang, X. Yan, P. Sun, K. Shimanoe and G. Lu, *Sens. Actuators, B*, 2021, **332**, 129444.

164 P. Bharathi, S. Harish, M. Shimomura, S. Ponnusamy, M. Krishna Mohan, J. Archana and M. Navaneethan, *Sens. Actuators, B*, 2022, **360**, 131600.

165 Q. He, Z. Zeng, Z. Yin, H. Li, S. Wu, X. Huang and H. Zhang, *Small*, 2012, **8**, 2994–2999.

166 D. J. Late, Y.-K. Huang, B. Liu, J. Acharya, S. N. Shirodkar, J. Luo, A. Yan, D. Charles, U. V. Waghmare, V. P. Dravid and C. N. R. Rao, *ACS Nano*, 2013, **7**, 4879–4891.

167 Y. Niu, J. Zeng, X. Liu, J. Li, Q. Wang, H. Li, N. F. d. Rooij, Y. Wang and G. Zhou, *Adv. Sci.*, 2021, **8**, 2100472.

168 X. Bai, H. Lv, Z. Liu, J. Chen, J. Wang, B. Sun, Y. Zhang, R. Wang and K. Shi, *J. Hazard. Mater.*, 2021, **416**, 125830.

169 R. R. Kumar, T. Murugesan, A. Dash, C.-H. Hsu, S. Gupta, A. Manikandan, A. k. Anbalagan, C.-H. Lee, N.-H. Tai, Y.-L. Chueh and H.-N. Lin, *Appl. Surf. Sci.*, 2021, **536**, 147933.

170 J.-H. Kim, J.-Y. Kim, A. Mirzaei, H. W. Kim and S. S. Kim, *Sens. Actuators, B*, 2021, **332**, 129493.

171 X. Chen, J. Hu, P. Chen, M. Yin, F. Meng and Y. Zhang, *Sens. Actuators, B*, 2021, **339**, 129902.

172 Q. Zhou, L. Zhu, C. Zheng and J. Wang, *ACS Appl. Mater. Interfaces*, 2021, **13**, 41339–41350.

173 D. Simon Patrick, P. Bharathi, M. Krishna Mohan, C. Muthamizchelvan, S. Harish and M. Navaneethan, *J. Mater. Sci.: Mater. Electron.*, 2022, **33**, 9235–9245.

6058 | *J. Mater. Chem. A*, 2023, **11**, 6016–6063

This journal is © The Royal Society of Chemistry 2023

174 H. Luo, J. Shi, C. Liu, X. Chen, W. Lv, Y. Zhou, M. Zeng, J. Yang, H. Wei, Z. Zhou, Y. Su, N. Hu and Z. Yang, *Nanotechnology*, 2021, **32**, 445502.

175 M. Reddeppa, N. T. KimPhung, G. Murali, K. S. Pasupuleti, B.-G. Park, I. In and M.-D. Kim, *Sens. Actuators, B*, 2021, **329**, 129175.

176 A. Govind, P. Bharathi, G. Mathankumar, M. K. Mohan, J. Archana, S. Harish and M. Navaneethan, *Diamond Relat. Mater.*, 2022, **128**, 109205.

177 D. Zhang, S. Yu, X. Wang, J. Huang, W. Pan, J. Zhang, B. E. Meteku and J. Zeng, *J. Hazard. Mater.*, 2022, **423**, 127160.

178 Z. Yang, L. Jiang, J. Wang, F. Liu, J. He, A. Liu, S. Lv, R. You, X. Yan, P. Sun, C. Wang, Y. Duan and G. Lu, *Sens. Actuators, B*, 2021, **326**, 128828.

179 D. Zhang, Q. Mi, D. Wang and T. Li, *Sens. Actuators, B*, 2021, **339**, 129923.

180 S. Gasso, M. K. Sohal and A. Mahajan, *Sens. Actuators, B*, 2022, **357**, 131427.

181 Z. Wang, F. Wang, A. Hermawan, Y. Asakura, T. Hasegawa, H. Kumagai, H. Kato, M. Kakihana, J. Zhu and S. Yin, *J. Mater. Sci. Technol.*, 2021, **73**, 128–138.

182 X. Guan, X. Yu, D. Periyanagounder, M. R. Benzigar, J.-K. Huang, C.-H. Lin, J. Kim, S. Singh, L. Hu, G. Liu, D. Li, J.-H. He, F. Yan, Q. J. Wang and T. Wu, *Adv. Opt. Mater.*, 2021, **9**, 2001708.

183 B. Sun, H. Lv, Z. Liu, J. Wang, X. Bai, Y. Zhang, J. Chen, K. Kan and K. Shi, *J. Mater. Chem. A*, 2021, **9**, 6335–6344.

184 L. Yao, X. Tian, X. Cui, R. Zhao, X. Xiao and Y. Wang, *J. Mater. Sci.: Mater. Electron.*, 2021, **32**, 27837–27848.

185 M. N. Islam and R. B. Channon, in *Bioengineering Innovative Solutions for Cancer*, ed. S. Ladame and J. Y. H. Chang, Academic Press, 2020, pp. 47–71, DOI: 10.1016/B978-0-12-813886-1.00004-8.

186 A. Chowdhury, S. Biswas, T. Singh and A. Chandra, *Electrochem. Sci. Adv.*, 2022, **2**, e2100030.

187 C. W. Lee, J. M. Suh and H. W. Jang, *Front. Chem.*, 2019, **7**, 708.

188 A. Raza, X. Zhang, S. Ali, C. Cao, A. A. Rafi and G. Li, *Photochem*, 2022, **2**, 272–298.

189 J. Wang, *Analyst*, 2005, **130**, 421–426.

190 A. Chen and S. Chatterjee, *Chem. Soc. Rev.*, 2013, **42**, 5425–5438.

191 S. Guo and S. Dong, *Chem. Soc. Rev.*, 2011, **40**, 2644–2672.

192 X. Hong, C. Tan, J. Chen, Z. Xu and H. Zhang, *Nano Res.*, 2015, **8**, 40–55.

193 S. Wu, Q. He, C. Tan, Y. Wang and H. Zhang, *Small*, 2013, **9**, 1160–1172.

194 P. K. Kannan, D. J. Late, H. Morgan and C. S. Rout, *Nanoscale*, 2015, **7**, 13293–13312.

195 S. Wu, Z. Zeng, Q. He, Z. Wang, S. J. Wang, Y. Du, Z. Yin, X. Sun, W. Chen and H. Zhang, *Small*, 2012, **8**, 2264–2270.

196 A. Raza, A. Rafiq, U. Qumar and J. Z. Hassan, *Sustainable Mater. Technol.*, 2022, **33**, e00469.

197 H. Liu, C. Duan, C. Yang, W. Shen, F. Wang and Z. Zhu, *Sens. Actuators, B*, 2015, **218**, 60–66.

198 Y. Wang, M. Zhao, J. Ping, B. Chen, X. Cao, Y. Huang, C. Tan, Q. Ma, S. Wu, Y. Yu, Q. Lu, J. Chen, W. Zhao, Y. Ying and H. Zhang, *Adv. Mater.*, 2016, **28**, 4149–4155.

199 Y. Han, R. Zhang, C. Dong, F. Cheng and Y. Guo, *Biosens. Bioelectron.*, 2019, **142**, 111529.

200 M. Mehmandoust, S. Çakar, M. Özacar, S. Salmanpour and N. Erk, *Top. Catal.*, 2022, **65**, 564–576.

201 Y. Wang, B. Zhang, Y. Tang, F. Zhao and B. Zeng, *Microchem. J.*, 2021, **168**, 106505.

202 Y. Sun, L. Xu, G. I. N. Waterhouse, M. Wang, X. Qiao and Z. Xu, *Sens. Actuators, B*, 2019, **281**, 107–114.

203 X. Fang, Z. Zeng, Q. Li, Y. Liu, W. Chu, T. Maiyalagan and S. Mao, *Sens. Actuators, B*, 2021, **332**, 129526.

204 R. Ji, W. Niu, S. Chen, W. Xu, X. Ji, L. Yuan, H. Zhao, M. Geng, J. Qiu and C. Li, *Biosens. Bioelectron.*, 2019, **144**, 111560.

205 B. G. Santos, J. M. Gonçalves, D. P. Rocha, G. S. Higino, T. P. Yadav, J. J. Pedrotti, P. M. Ajayan and L. Angnes, *Sens. Actuators*, 2022, **4**, 100073.

206 Z. Zhang, J. Xu, Y. Wen and T. Wang, *Mater. Sci. Eng., C*, 2018, **92**, 77–87.

207 R. Ji, S. Chen, W. Xu, Z. Qin, J. F. Qiu and C. R. Li, *Microchim. Acta*, 2018, **185**, 209.

208 V. Mariyappan, N. Karuppusamy, S.-M. Chen, P. Raja and R. Ramachandran, *Microchim. Acta*, 2022, **189**, 118.

209 T.-W. Chen, U. Rajaji, S.-M. Chen and R. Jothi Ramalingam, *Ultrason. Sonochem.*, 2019, **54**, 79–89.

210 J. Zou, S. Wu, Y. Liu, Y. Sun, Y. Cao, J.-P. Hsu, A. T. Shen Wee and J. Jiang, *Carbon*, 2018, **130**, 652–663.

211 H. Karimi-Maleh, R. Darabi, M. Shabani-Nooshabadi, M. Baghayeri, F. Karimi, J. Rouhi, M. Alizadeh, O. Karaman, Y. Vasseghian and C. Karaman, *Food Chem. Toxicol.*, 2022, **162**, 112907.

212 E. Puentes-Prado, S. Gutiérrez-Granados, C. Gómez-Solís and G. Ramírez-García, *FlatChem*, 2022, **35**, 100412.

213 S. Mert, B. Bankoğlu, A. Özkan, N. Atar and M. L. Yola, *J. Mol. Liq.*, 2018, **254**, 8–11.

214 X. Zhou, L. Yang, X. Tan, G. Zhao, X. Xie and G. Du, *Biosens. Bioelectron.*, 2018, **112**, 31–39.

215 Y. Wang, Y. Zhang, H. Sha, X. Xiong and N. Jia, *ACS Appl. Mater. Interfaces*, 2019, **11**, 36299–36306.

216 S. Selvarajan, A. Suganthi and M. Rajarajan, *Ultrason. Sonochem.*, 2018, **41**, 651–660.

217 B. Hatamluyi, M. Rezayi, H. R. Beheshti and M. T. Boroushaki, *Sens. Actuators, B*, 2020, **318**, 128219.

218 T. Iftikhar, Y. Xu, A. Aziz, G. Ashraf, G. Li, M. Asif, F. Xiao and H. Liu, *ACS Appl. Mater. Interfaces*, 2021, **13**, 31462–31473.

219 F. Gao, X. Tu, X. Ma, Y. Xie, J. Zou, X. Huang, F. Qu, Y. Yu and L. Lu, *Talanta*, 2020, **215**, 120891.

220 C. Xu, L. Liu, C. Wu and K. Wu, *Sens. Actuators, B*, 2020, **310**, 127885.

221 D. Cheng, X. Xiao, X. Li, C. Wang, Y. Liang, Z. Yu, C. Jin, N. Zhou, M. Chen, Y. Dong, Y. Lin, Z. Xie and C. Zhang, *J. Electrochem. Soc.*, 2018, **165**, B885–B892.

222 M. Baghayeri, M. Ghanei-Motlagh, R. Tayebee, M. Fayazi and F. Narenji, *Anal. Chim. Acta*, 2020, **1099**, 60–67.

This journal is © The Royal Society of Chemistry 2023

J. Mater. Chem. A, 2023, **11**, 6016–6063 | **6059**

223 Y. Dong, J. Li and L. Zhang, *Sens. Actuators, B*, 2020, **303**, 127208.

224 K. S. Ranjith, A. T. Ezhil Vilian, S. M. Ghoreishian, R. Umapathi, S.-K. Hwang, C. W. Oh, Y. S. Huh and Y.-K. Han, *J. Hazard. Mater.*, 2022, **421**, 126775.

225 P. Xiao, G. Zhu, X. Shang, B. Hu, B. Zhang, Z. Tang, J. Yang and J. Liu, *J. Electroanal. Chem.*, 2022, **916**, 116382.

226 M. Ni, J. Chen, C. Wang, Y. Wang, L. Huang, W. Xiong, P. Zhao, Y. Xie and J. Fei, *Microchem. J.*, 2022, **178**, 107410.

227 K. S. Bhat, S. Byun, A. Alam, M. Ko, J. An and S. Lim, *Talanta*, 2022, **244**, 123421.

228 X. Zhang, D. An, Z. Bi, W. Shan, B. Zhu, L. Zhou, L. Yu, H. Zhang, S. Xia and M. Qiu, *J. Electroanal. Chem.*, 2022, **911**, 116239.

229 H. Wang, L. Cai, Y. Wang, C. Liu, G. Fang and S. Wang, *Food Chem.*, 2022, **383**, 132382.

230 Y. Xia, X. Hu, Y. Liu, F. Zhao and B. Zeng, *Microchim. Acta*, 2022, **189**, 137.

231 T. S. Gopal, S. K. Jeong, T. A. Alrebdi, S. Pandiaraj, A. Alodhayb, M. Muthuramamoorthy and G. Andrews Nirmala, *Mater. Today Chem.*, 2022, **24**, 100891.

232 Y. Chen, S. Li, L. Zhang, T. Jing, J. Wang, L. Zhao, F. Li, C. Li and J. Sun, *J. Solid State Chem.*, 2022, **308**, 122919.

233 M. Li, L. Wang, R. Liu, J. Li, Q. Zhang, G. Shi, Y. Li, C. Hou and H. Wang, *Biosens. Bioelectron.*, 2021, **174**, 112828.

234 B. Anasori, M. R. Lukatskaya and Y. Gogotsi, *Nat. Rev. Mater.*, 2017, **2**, 16098.

235 M. Alhabeb, K. Maleski, B. Anasori, P. Lelyukh, L. Clark, S. Sin and Y. Gogotsi, *Chem. Mater.*, 2017, **29**, 7633–7644.

236 J. Liu, D. Su, K. Wu and J.-P. Wang, *J. Nanopart. Res.*, 2020, **22**, 66.

237 W. Lu, P. Yu, M. Jian, H. Wang, H. Wang, X. Liang and Y. Zhang, *ACS Appl. Mater. Interfaces*, 2020, **12**, 11825–11832.

238 M. Shin, J. Yoon, C. Yi, T. Lee and J.-W. Choi, *Nanomaterials*, 2019, **9**, 1076.

239 Z. Wang, S. Dong, M. Gui, M. Asif, W. Wang, F. Wang and H. Liu, *Anal. Biochem.*, 2018, **543**, 82–89.

240 Z. Wang, M. Gui, M. Asif, Y. Yu, S. Dong, H. Wang, W. Wang, F. Wang, F. Xiao and H. Liu, *Nanoscale*, 2018, **10**, 6629–6638.

241 J. Yoon, S. N. Lee, M. K. Shin, H.-W. Kim, H. K. Choi, T. Lee and J.-W. Choi, *Biosens. Bioelectron.*, 2019, **140**, 111343.

242 B. N. Shivananju, S. Yamdagni, R. Fazuldeen, A. K. S. Kumar, S. P. Nithin, M. M. Varma and S. Asokan, *IEEE Sens. J.*, 2014, **14**, 2615–2619.

243 D. Li, H. Lu, W. Qiu, J. Dong, H. Guan, W. Zhu, J. Yu, Y. Luo, J. Zhang and Z. Chen, *Opt. Express*, 2017, **25**, 28407–28416.

244 Y. Luo, C. Chen, K. Xia, S. Peng, H. Guan, J. Tang, H. Lu, J. Yu, J. Zhang, Y. Xiao and Z. Chen, *Opt. Express*, 2016, **24**, 8956–8966.

245 O. Leenaerts, B. Partoens and F. M. Peeters, *Phys. Rev. B: Condens. Matter Mater. Phys.*, 2008, **77**, 125416.

246 T. Ouyang, L. Lin, K. Xia, M. Jiang, Y. Lang, H. Guan, J. Yu, D. Li, G. Chen, W. Zhu, Y. Zhong, J. Tang, J. Dong, H. Lu, Y. Luo, J. Zhang and Z. Chen, *Opt. Express*, 2017, **25**, 9823–9833.

247 M. S. Siddiqui, A. Mandal, H. Kalita and M. Aslam, *Sens. Actuators, B*, 2022, **365**, 131930.

248 H. H. Hau, T. T. H. Duong, N. K. Man, T. Thi Viet Nga, C. Thi Xuan, D. Thi Thanh Le, N. Van Toan, C. M. Hung, N. Van Duy, N. Van Hieu and N. D. Hoa, *Sens. Actuators, A*, 2021, **332**, 113137.

249 S. Yadav, P. Chaudhary, K. N. Uttam, A. Varma, M. Vashistha and B. C. Yadav, *Nanotechnology*, 2019, **30**, 295501.

250 W. Wang, Y. Zhen, J. Zhang, Y. Li, H. Zhong, Z. Jia, Y. Xiong, Q. Xue, Y. Yan, N. S. Alharbi and T. Hayat, *Sens. Actuators, B*, 2020, **321**, 128471.

251 Y. Xia, C. Hu, S. Guo, L. Zhang, M. Wang, J. Peng, L. Xu and J. Wang, *ACS Appl. Nano Mater.*, 2020, **3**, 665–673.

252 X. Yu, X. Chen, X. Yu, X. Chen, X. Ding, X. Zhao and K. Tang, *IEEE Trans. Electron Devices*, 2022, **69**, 1321–1326.

253 Y. Ding, X. Guo, B. Du, X. Hu, X. Yang, Y. He, Y. Zhou and Z. Zang, *J. Mater. Chem. C*, 2021, **9**, 4838–4846.

254 G. Chen, J. Li and F. Meng, *J. Alloys Compd.*, 2022, **896**, 163063.

255 W. Li, Y. Zhang, X. Long, J. Cao, X. Xin, X. Guan, J. Peng and X. Zheng, *Sensors*, 2019, **19**, 2123.

256 A. Abun, B.-R. Huang, A. Saravanan, D. Kathiravan and P.-D. Hong, *J. Alloys Compd.*, 2020, **832**, 155005.

257 Y. Wang, Y. Zhou, G. Xie, J. Li, Y. Wang, X. Liu and Z. Zang, *ACS Appl. Mater. Interfaces*, 2021, **13**, 25250–25259.

258 Y. Han, D. Huang, Y. Ma, G. He, J. Hu, J. Zhang, N. Hu, Y. Su, Z. Zhou, Y. Zhang and Z. Yang, *ACS Appl. Mater. Interfaces*, 2018, **10**, 22640–22649.

259 M. A. Dwiputra, F. Fadhila, C. Imawan and V. Fauzia, *Sens. Actuators, B*, 2020, **310**, 127810.

260 A. Gupta, N. Sakhuja, R. K. Jha and N. Bhat, *Sens. Actuators, A*, 2021, **331**, 113008.

261 S. G. Leonardi, W. Wlodarski, Y. Li, N. Donato, Z. Sofer, M. Pumera and G. Neri, *FlatChem*, 2018, **9**, 21–26.

262 D. Liu, Z. Tang and Z. Zhang, *Sens. Actuators, B*, 2020, **303**, 127114.

263 Y. Chen, Y. Pei, Z. Jiang, Z. Shi, J. Xu, D. Wu, T. Xu, Y. Tian, X. Wang and X. Li, *Appl. Surf. Sci.*, 2018, **447**, 325–330.

264 R. Li, Y. Fan, Z. Ma, D. Zhang, Y. Liu and J. Xu, *Microchim. Acta*, 2021, **188**, 81.

265 H. An, T. Habib, S. Shah, H. Gao, A. Patel, I. Echols, X. Zhao, M. Radovic, M. J. Green and J. L. Lutkenhaus, *ACS Appl. Nano Mater.*, 2019, **2**, 948–955.

266 Y. Zhou, Y. Wang, Y. Wang and X. Li, *Anal. Chem.*, 2020, **92**, 16033–16042.

267 M. Balali-Mood, K. Naseri, Z. Tahergorabi, M. R. Khazdair and M. Sadeghi, *Front. Pharmacol.*, 2021, **12**, 227.

268 S. Mitra, A. J. Chakraborty, A. M. Tareq, T. B. Emran, F. Nainu, A. Khusro, A. M. Idris, M. U. Khandaker, H. Osman, F. A. Alhumaydhi and J. Simal-Gandara, *J. King Saud Univ., Sci.*, 2022, **34**, 101865.

269 C. Liu, Z. Sun, L. Zhang, J. Lv, X. F. Yu, L. Zhang and X. Chen, *Sens. Actuators, B*, 2018, **257**, 1093–1098.

270 J. R. Brent, N. Savjani, E. A. Lewis, S. J. Haigh, D. J. Lewis and P. O'Brien, *Chem. Commun.*, 2014, **50**, 13338–13341.

6060 | *J. Mater. Chem. A*, 2023, **11**, 6016–6063

This journal is © The Royal Society of Chemistry 2023

271 Q. Zhou, Q. Chen, Y. Tong and J. Wang, *Angew. Chem., Int. Ed.*, 2016, **55**, 11437–11441.

272 Y. Zeng and Z. Guo, *iScience*, 2021, **24**, 103116.

273 M. Qiu, A. Singh, D. Wang, J. Qu, M. Swihart, H. Zhang and P. N. Prasad, *Nano Today*, 2019, **25**, 135–155.

274 G. Abellán, V. Lloret, U. Mundloch, M. Marcia, C. Neiss, A. Görling, M. Varela, F. Hauke and A. Hirsch, *Angew. Chem., Int. Ed.*, 2016, **55**, 14557–14562.

275 Y. Zhao, H. Wang, H. Huang, Q. Xiao, Y. Xu, Z. Guo, H. Xie, J. Shao, Z. Sun, W. Han, X.-F. Yu, P. Li and P. K. Chu, *Angew. Chem., Int. Ed.*, 2016, **55**, 5003–5007.

276 D. He, Y. Wang, Y. Huang, Y. Shi, X. Wang and X. Duan, *Nano Lett.*, 2019, **19**, 331–337.

277 L. Wu, J. Wang, J. Lu, D. Liu, N. Yang, H. Huang, P. K. Chu and X.-F. Yu, *Small*, 2018, **14**, 1801405.

278 P. Li, D. Zhang, J. Liu, H. Chang, Y. e. Sun and N. Yin, *ACS Appl. Mater. Interfaces*, 2015, **7**, 24396–24402.

279 M. Shaban and A. R. Galaly, *Sci. Rep.*, 2016, **6**, 25307.

280 Z. Yin, H. Li, H. Li, L. Jiang, Y. Shi, Y. Sun, G. Lu, Q. Zhang, X. Chen and H. Zhang, *ACS Nano*, 2012, **6**, 74–80.

281 J. Z. Ou, W. Ge, B. Carey, T. Daeneke, A. Rotbart, W. Shan, Y. Wang, Z. Fu, A. F. Chrimes, W. Wlodarski, S. P. Russo, Y. X. Li and K. Kalantar-zadeh, *ACS Nano*, 2015, **9**, 10313–10323.

282 N. Huo, S. Yang, Z. Wei, S.-S. Li, J.-B. Xia and J. Li, *Sci. Rep.*, 2014, **4**, 5209.

283 C. J. Zhou, W. H. Yang, Y. P. Wu, W. Lin and H. L. Zhu, *J. Phys. D: Appl. Phys.*, 2015, **48**, 285303.

284 D. J. Late, T. Doneux and M. Bougouma, *Appl. Phys. Lett.*, 2014, **105**, 233103.

285 A. N. Abbas, B. Liu, L. Chen, Y. Ma, S. Cong, N. Aroonyadet, M. Köpf, T. Nilges and C. Zhou, *ACS Nano*, 2015, **9**, 5618–5624.

286 L. Kou, T. Frauenheim and C. Chen, *J. Phys. Chem. Lett.*, 2014, **5**, 2675–2681.

287 D. Chen, X. Hou, H. Wen, Y. Wang, H. Wang, X. Li, R. Zhang, H. Lu, H. Xu, S. Guan, J. Sun and L. Gao, *Nanotechnology*, 2009, **21**, 035501.

288 H. Fan and X. Jia, *Solid State Ionics*, 2011, **192**, 688–692.

289 J. Liu, Z. Guo, F. Meng, T. Luo, M. Li and J. Liu, *Nanotechnology*, 2009, **20**, 125501.

290 J. Wang, P. Yang, X. Wei and Z. Zhou, *Nanoscale Res. Lett.*, 2015, **10**, 119.

291 D. Sarkar, W. Liu, X. Xie, A. C. Anselmo, S. Mitragotri and K. Banerjee, *ACS Nano*, 2014, **8**, 3992–4003.

292 J. Lee, P. Dak, Y. Lee, H. Park, W. Choi, M. A. Alam and S. Kim, *Sci. Rep.*, 2014, **4**, 7352.

293 L. Wang, Y. Wang, J. I. Wong, T. Palacios, J. Kong and H. Y. Yang, *Small*, 2014, **10**, 1101–1105.

294 C.-H. Lu, H.-H. Yang, C.-L. Zhu, X. Chen and G.-N. Chen, *Angew. Chem., Int. Ed.*, 2009, **48**, 4785–4787.

295 S. He, B. Song, D. Li, C. Zhu, W. Qi, Y. Wen, L. Wang, S. Song, H. Fang and C. Fan, *Adv. Funct. Mater.*, 2010, **20**, 453–459.

296 Y. Wen, F. Xing, S. He, S. Song, L. Wang, Y. Long, D. Li and C. Fan, *Chem. Commun.*, 2010, **46**, 2596–2598.

297 Y. Wen, C. Peng, D. Li, L. Zhuo, S. He, L. Wang, Q. Huang, Q.-H. Xu and C. Fan, *Chem. Commun.*, 2011, **47**, 6278–6280.

298 Y. Zhang, B. Zheng, C. Zhu, X. Zhang, C. Tan, H. Li, B. Chen, J. Yang, J. Chen, Y. Huang, L. Wang and H. Zhang, *Adv. Mater.*, 2015, **27**, 935–939.

299 J. Huang, L. Ye, X. Gao, H. Li, J. Xu and Z. Li, *J. Mater. Chem. B*, 2015, **3**, 2395–2401.

300 Y. Yang, T. Liu, L. Cheng, G. Song, Z. Liu and M. Chen, *ACS Appl. Mater. Interfaces*, 2015, **7**, 7526–7533.

301 Q. Xi, D.-M. Zhou, Y.-Y. Kan, J. Ge, Z.-K. Wu, R.-Q. Yu and J.-H. Jiang, *Anal. Chem.*, 2014, **86**, 1361–1365.

302 Y. Yuan, R. Li and Z. Liu, *Anal. Chem.*, 2014, **86**, 3610–3615.

303 C. Tan, P. Yu, Y. Hu, J. Chen, Y. Huang, Y. Cai, Z. Luo, B. Li, Q. Lu, L. Wang, Z. Liu and H. Zhang, *J. Am. Chem. Soc.*, 2015, **137**, 10430–10436.

304 Q. Wang, W. Wang, J. Lei, N. Xu, F. Gao and H. Ju, *Anal. Chem.*, 2013, **85**, 12182–12188.

305 M. Rong, L. Lin, X. Song, T. Zhao, Y. Zhong, J. Yan, Y. Wang and X. Chen, *Anal. Chem.*, 2015, **87**, 1288–1296.

306 Z. Fan and H. Zhang, *Chem. Soc. Rev.*, 2016, **45**, 63–82.

307 Y. Peng, Y. Huang, Y. Zhu, B. Chen, L. Wang, Z. Lai, Z. Zhang, M. Zhao, C. Tan, N. Yang, F. Shao, Y. Han and H. Zhang, *J. Am. Chem. Soc.*, 2017, **139**, 8698–8704.

308 K. Xu, R. Zhou, K. Takei and M. Hong, *Adv. Sci.*, 2019, **6**, 1900925.

309 X. Lin, W. L. J. Hasi, S. Q. G. W. Han, X. T. Lou, D. Y. Lin and Z. W. Lu, *Phys. Chem. Chem. Phys.*, 2015, **17**, 31324–31331.

310 W. Wei, Y. Du, L. Zhang, Y. Yang and Y. Gao, *J. Mater. Chem. C*, 2018, **6**, 8793–8803.

311 C. Li, S. Guo, L. Cao and J. Li, *Ind. Mark. Manag.*, 2018, **72**, 152–160.

312 C. Li, J. Yu, S. Xu, S. Jiang, X. Xiu, C. Chen, A. Liu, T. Wu, B. Man and C. Zhang, *Adv. Mater. Technol.*, 2018, **3**, 1800174.

313 H. Qiu, M. Wang, S. Jiang, L. Zhang, Z. Yang, L. Li, J. Li, M. Cao and J. Huang, *Sens. Actuators, B*, 2017, **249**, 439–450.

314 C. Li, A. Liu, C. Zhang, M. Wang, Z. Li, S. Xu, S. Jiang, J. Yu, C. Yang and B. Man, *Opt. Express*, 2017, **25**, 20631–20641.

315 C. Li, S. Xu, J. Yu, S. Jiang, A. Liu, Z. Li, S. Zhang, X. Zhao, C. Zhang and B. Man, *Sens. Actuators, B*, 2018, **274**, 152–162.

316 J. Wu, N. Mao, L. Xie, H. Xu and J. Zhang, *Angew. Chem., Int. Ed.*, 2015, **54**, 2366–2369.

317 A. C. Ferrari, J. C. Meyer, V. Scardaci, C. Casiraghi, M. Lazzeri, F. Mauri, S. Piscanec, D. Jiang, K. S. Novoselov, S. Roth and A. K. Geim, *Phys. Rev. Lett.*, 2006, **97**, 187401.

318 S. Mathew, T. K. Chan, D. Zhan, K. Gopinadhan, A. Roy Barman, M. B. H. Breese, S. Dhar, Z. X. Shen, T. Venkatesan and J. T. L. Thong, *J. Appl. Phys.*, 2011, **110**, 084309.

319 J. Chen, Y. Li, Y. Huang, H. Zhang, X. Chen and H. Qiu, *Microchim. Acta*, 2019, **186**, 58.

320 K. Srinivasan, K. Subramanian, K. Murugan, G. Benelli and K. Dinakaran, *Environ. Sci. Pollut. Res.*, 2018, **25**, 10567–10576.

321 P. Sharma and M. S. Mehata, *Mater. Res. Bull.*, 2020, **131**, 110978.

This journal is © The Royal Society of Chemistry 2023

J. Mater. Chem. A, 2023, **11**, 6016–6063 | **6061**

322 L. Ruan, Y. Zhao, Z. Chen, W. Zeng, S. Wang, D. Liang and J. Zhao, *Appl. Surf. Sci.*, 2020, **528**, 146811.

323 L. Kong, X. Zhou, G. Shi and Y. Yu, *Analyst*, 2020, **145**, 6369–6377.

324 T.-W. Lin, N. Dhenadhayalan, H.-L. Lee, Y.-T. Lin, K.-C. Lin and A. H. H. Chang, *Sens. Actuators, B*, 2019, **281**, 659–669.

325 S. Feng, J. Lv, F. Pei, X. Lv, Y. Wu, Q. Hao, Y. Zhang, Z. Tong and W. Lei, *Spectrochim. Acta, Part A*, 2020, **231**, 118131.

326 J. Shi, Y. Zhang, P. Wang, Y. Nie and Q. Ma, *Talanta*, 2022, **237**, 122969.

327 P. Behera, K. K. Singh, S. Pandit, D. Saha, D. K. Saini and M. De, *ACS Appl. Nano Mater.*, 2021, **4**, 3843–3851.

328 K. Chen, W. Zhang, Y. Zhang, L. Huang, R. Wang, X. Yue, W. Zhu, D. Zhang, X. Zhang, Y. Zhang and J. Wang, *Sens. Actuators, B*, 2018, **259**, 717–724.

329 M. Junaid, M. Imran, M. Ikram, M. Naz, M. Aqeel, H. Afzal, H. Majeed and S. Ali, *Appl. Nanosci.*, 2019, **9**, 1593–1602.

330 J. J. Wang, Y. Liu, Z. Ding, L. Zhang, C. Han, C. Yan, E. Amador, L. Yuan, Y. Wu, C. Song, Y. Liu and W. Chen, *Bioact. Mater.*, 2022, **17**, 360–368.

331 E. Sameiyan, Z. Khoshbin, P. Lavaee, M. Ramezani, M. Alibolandi, K. Abnous and S. M. Taghdisi, *Talanta*, 2021, **235**, 122779.

332 Y. Yan, C. Zhang, W. Gu, C. Ding, X. Li and Y. Xian, *J. Phys. Chem. C*, 2016, **120**, 12170–12177.

333 V. K. Singh, H. Mishra, R. Ali, S. Umrao, R. Srivastava, S. Abraham, A. Misra, V. N. Singh, H. Mishra, R. S. Tiwari and A. Srivastava, *ACS Appl. Nano Mater.*, 2019, **2**, 566–576.

334 M. Pacheco, V. d. l. Asunción-Nadal, B. Jurado-Sánchez and A. Escarpa, *Biosens. Bioelectron.*, 2020, **165**, 112286.

335 J. Ge, G. Xin, Y.-H. Du, J.-J. Chen, L. Zhang, D.-M. Bai, D.-Y. Ji, Y.-L. Hu and Z.-H. Li, *Sens. Actuators, B*, 2017, **249**, 189–194.

336 X. Zuo, H. Zhang, Q. Zhu, W. Wang, J. Feng and X. Chen, *Biosens. Bioelectron.*, 2016, **85**, 464–470.

337 H. Safardoust-Hojaghan, O. Amiri, M. Hassanpour, M. Panahi-Kalamuei, H. Moayedi and M. Salavati-Niasari, *Food Chem.*, 2019, **295**, 530–536.

338 F. Du, L. Sun, Q. Zen, W. Tan, Z. Cheng, G. Ruan and J. Li, *Sens. Actuators, B*, 2019, **288**, 96–103.

339 Z. Liu, Z. Mo, X. Niu, X. Yang, Y. Jiang, P. Zhao, N. Liu and R. Guo, *J. Colloid Interface Sci.*, 2020, **566**, 357–368.

340 M. Wan, J. Zhou, H. Yang, X. Dai, Y. Zheng, Z. Xia and L. Wang, *ACS Appl. Nano Mater.*, 2022, **5**, 11715–11722.

341 F. Wang, H. Wang, X. Cui and Y. Liu, *Sens. Diagn.*, 2022, **1**, 1080–1087.

342 D. Huang, Y. Wu, F. Ai, X. Zhou and G. Zhu, *Sens. Actuators, B*, 2021, **342**, 130074.

343 Y. Bai, Y. He, Y. Wang and G. Song, *Microchim. Acta*, 2021, **188**, 401.

344 W. Luo, H. Liu, X. Liu, L. Liu and W. Zhao, *Colloids Surf., B*, 2021, **201**, 111631.

345 Y. Bai, Y. He, M. Wang and G. Song, *Sens. Actuators, B*, 2022, **357**, 131410.

346 S. Li, J. Ma, X. Zhao, P. Zhu, M. Xu, Y. Niu, D. Luo and Q. Xu, *Chin. Chem. Lett.*, 2022, **33**, 1850–1854.

347 X. Gao, X. Shao, L. Qin, Y. Li, S. Huang and L. Deng, *Nanoscale Res. Lett.*, 2021, **16**, 160.

348 J. Moyer, D. Wilson, I. Finkelshtein, B. Wong and R. Potts, *Diabetes Technol. Ther.*, 2012, **14**, 398–402.

349 M. F. Bergeron, *J. Sci. Med. Sport*, 2003, **6**, 19–27.

350 R. C. Stern, *N. Engl. J. Med.*, 1997, **336**, 487–491.

351 M. Bariya, H. Y. Y. Nyein and A. Javey, *Nat. Electron.*, 2018, **1**, 160–171.

352 H. Xu, Y. F. Lu, J. X. Xiang, M. K. Zhang, Y. J. Zhao, Z. Y. Xie and Z. Z. Gu, *Nanoscale*, 2018, **10**, 2090–2098.

353 L. Cao, C. Fang, R. Zeng, X. Zhao, F. Zhao, Y. Jiang and Z. Chen, *Sens. Actuators, B*, 2017, **252**, 44–54.

354 D. Khatayevich, T. Page, C. Gresswell, Y. Hayamizu, W. Grady and M. Sarikaya, *Small*, 2014, **10**, 1505–1513.

355 B. Zhang and T. Cui, *Sens. Actuators, A*, 2012, **177**, 110–114.

356 X. Xuan, H. S. Yoon and J. Y. Park, *Biosens. Bioelectron.*, 2018, **109**, 75–82.

357 H. Lee, T. K. Choi, Y. B. Lee, H. R. Cho, R. Ghaffari, L. Wang, H. J. Choi, T. D. Chung, N. Lu, T. Hyeon, S. H. Choi and D.-H. Kim, *Nat. Nanotechnol.*, 2016, **11**, 566–572.

358 F.-Y. Kong, S.-X. Gu, W.-W. Li, T.-T. Chen, Q. Xu and W. Wang, *Biosens. Bioelectron.*, 2014, **56**, 77–82.

359 H. Lee, C. Song, S. Hong Yong, S. Kim Min, R. Cho Hye, T. Kang, K. Shin, H. Choi Seung, T. Hyeon and D.-H. Kim, *Sci. Adv.*, 2017, **3**, e1601314.

360 D. Kinnamon, R. Ghanta, K.-C. Lin, S. Muthukumar and S. Prasad, *Sci. Rep.*, 2017, **7**, 13312.

361 R. B. Rakhi, P. Nayak, C. Xia and H. N. Alshareef, *Sci. Rep.*, 2016, **6**, 36422.

362 S. Borini, R. White, D. Wei, M. Astley, S. Haque, E. Spigone, N. Harris, J. Kivioja and T. Ryhänen, *ACS Nano*, 2013, **7**, 11166–11173.

363 J.-W. Yoon and J.-H. Lee, *Lab Chip*, 2017, **17**, 3537–3557.

364 Y. Pang, J. Jian, T. Tu, Z. Yang, J. Ling, Y. Li, X. Wang, Y. Qiao, H. Tian, Y. Yang and T.-L. Ren, *Biosens. Bioelectron.*, 2018, **116**, 123–129.

365 F. A. R. Mendes, A. França-Pinto, M. A. Martins, A. Cukier, R. Stelmach, P. Giavina-Bianchi and C. R. F. Carvalho, *J. Asthma*, 2019, **56**, 674–679.

366 Y. Jung, H. G. Moon, C. Lim, K. Choi, H. S. Song, S. Bae, S. M. Kim, M. Seo, T. Lee, S. Lee, H.-H. Park, S. C. Jun, C.-Y. Kang and C. Kim, *Adv. Funct. Mater.*, 2017, **27**, 1700068.

367 L. Wang, J. A. Jackman, J. H. Park, E.-L. Tan and N.-J. Cho, *J. Mater. Chem. B*, 2017, **5**, 4019–4024.

368 K. Shehzad, T. Shi, A. Qadir, X. Wan, H. Guo, A. Ali, W. Xuan, H. Xu, Z. Gu, X. Peng, J. Xie, L. Sun, Q. He, Z. Xu, C. Gao, Y.-S. Rim, Y. Dan, T. Hasan, P. Tan, E. Li, W. Yin, Z. Cheng, B. Yu, Y. Xu, J. Luo and X. Duan, *Adv. Mater. Technol.*, 2017, **2**, 1600262.

369 M. C. Caccami, M. Y. S. Mulla, C. Occhiuzzi, C. D. Natale and G. Marrocco, *IEEE Sens. J.*, 2018, **18**, 8893–8901.

370 J. He, P. Xiao, J. Shi, Y. Liang, W. Lu, Y. Chen, W. Wang, P. Théato, S.-W. Kuo and T. Chen, *Chem. Mater.*, 2018, **30**, 4343–4354.

371 B. Du, D. Yang, X. She, Y. Yuan, D. Mao, Y. Jiang and F. Lu, *Sens. Actuators, B*, 2017, **251**, 180–184.

6062 | *J. Mater. Chem. A*, 2023, **11**, 6016–6063

This journal is © The Royal Society of Chemistry 2023

372 N. Li, X. Chen, X. Chen, X. Ding and X. Zhao, *IEEE Electron Device Lett.*, 2017, **38**, 806–809.

373 D. Zhang, Y. e. Sun, P. Li and Y. Zhang, *ACS Appl. Mater. Interfaces*, 2016, **8**, 14142–14149.

374 P. Sahatiya, A. Kadu, H. Gupta, P. Thanga Gomathi and S. Badhulika, *ACS Appl. Mater. Interfaces*, 2018, **10**, 9048–9059.

375 B. Cho, J. Yoon, S. K. Lim, A. R. Kim, D.-H. Kim, S.-G. Park, J.-D. Kwon, Y.-J. Lee, K.-H. Lee, B. H. Lee, H. C. Ko and M. G. Hahm, *ACS Appl. Mater. Interfaces*, 2015, **7**, 16775–16780.

376 E. S. Muckley, M. Naguib and I. N. Ivanov, *Nanoscale*, 2018, **10**, 21689–21695.

377 H. Choi, J. S. Choi, J.-S. Kim, J.-H. Choe, K. H. Chung, J.-W. Shin, J. T. Kim, D.-H. Youn, K.-C. Kim, J.-I. Lee, S.-Y. Choi, P. Kim, C.-G. Choi and Y.-J. Yu, *Small*, 2014, **10**, 3685–3691.

378 H. Xu, J. X. Xiang, Y. F. Lu, M. K. Zhang, J. J. Li, B. B. Gao, Y. J. Zhao and Z. Z. Gu, *ACS Appl. Mater. Interfaces*, 2018, **10**, 11785–11793.

379 J.-S. Kim, H.-W. Yoo, H. O. Choi and H.-T. Jung, *Nano Lett.*, 2014, **14**, 5941–5947.

380 C. C. Mayorga-Martinez, A. Ambrosi, A. Y. S. Eng, Z. Sofer and M. Pumera, *Adv. Funct. Mater.*, 2015, **25**, 5611–5616.

381 B. Cho, A. R. Kim, D. J. Kim, H.-S. Chung, S. Y. Choi, J.-D. Kwon, S. W. Park, Y. Kim, B. H. Lee, K. H. Lee, D.-H. Kim, J. Nam and M. G. Hahm, *ACS Appl. Mater. Interfaces*, 2016, **8**, 19635–19642.

382 S.-Y. Cho, H.-J. Koh, H.-W. Yoo, J.-S. Kim and H.-T. Jung, *ACS Sens.*, 2017, **2**, 183–189.

383 A. Shokri and N. Salami, *Sens. Actuators, B*, 2016, **236**, 378–385.

384 X.-f. Yu, Y.-c. Li, J.-b. Cheng, Z.-b. Liu, Q.-z. Li, W.-z. Li, X. Yang and B. Xiao, *ACS Appl. Mater. Interfaces*, 2015, **7**, 13707–13713.

385 W. Yuan, K. Yang, H. Peng, F. Li and F. Yin, *J. Mater. Chem. A*, 2018, **6**, 18116–18124.

386 Y. Zhang, X. Jiang, J. Zhang, H. Zhang and Y. Li, *Biosens. Bioelectron.*, 2019, **130**, 315–321.

387 E. Lee, A. VahidMohammadi, B. C. Prorok, Y. S. Yoon, M. Beidaghi and D.-J. Kim, *ACS Appl. Mater. Interfaces*, 2017, **9**, 37184–37190.

388 S. J. Kim, H.-J. Koh, C. E. Ren, O. Kwon, K. Maleski, S.-Y. Cho, B. Anasori, C.-K. Kim, Y.-K. Choi, J. Kim, Y. Gogotsi and H.-T. Jung, *ACS Nano*, 2018, **12**, 986–993.

389 D. Ye, G. Liang, H. Li, J. Luo, S. Zhang, H. Chen and J. Kong, *Talanta*, 2013, **116**, 223–230.

390 J. Kim, G. Valdés-Ramírez, A. J. Bandodkar, W. Jia, A. G. Martinez, J. Ramírez, P. Mercier and J. Wang, *Analyst*, 2014, **139**, 1632–1636.

391 C. H. Mak, C. Liao, Y. Fu, M. Zhang, C. Y. Tang, Y. H. Tsang, H. L. W. Chan and F. Yan, *J. Mater. Chem. C*, 2015, **3**, 6532–6538.

392 M. S. Mannoor, H. Tao, J. D. Clayton, A. Sengupta, D. L. Kaplan, R. R. Naik, N. Verma, F. G. Omenetto and M. C. McAlpine, *Nat. Commun.*, 2012, **3**, 763.

393 C. Liao, C. Mak, M. Zhang, H. L. W. Chan and F. Yan, *Adv. Mater.*, 2015, **27**, 676–681.

394 F. Xing, G.-X. Meng, Q. Zhang, L.-T. Pan, P. Wang, Z.-B. Liu, W.-S. Jiang, Y. Chen and J.-G. Tian, *Nano Lett.*, 2014, **14**, 3563–3569.

395 P. T. K. Loan, W. Zhang, C.-T. Lin, K.-H. Wei, L.-J. Li and C.-H. Chen, *Adv. Mater.*, 2014, **26**, 4838–4844.

396 S. Sridevi, K. S. Vasu, S. Asokan and A. K. Sood, *Biosens. Bioelectron.*, 2015, **65**, 251–256.

397 S. Sridevi, K. S. Vasu, S. Sampath, S. Asokan and A. K. Sood, *J. Biophotonics*, 2016, **9**, 760–769.

398 T. Liu, C. Wang, X. Gu, H. Gong, L. Cheng, X. Shi, L. Feng, B. Sun and Z. Liu, *Adv. Mater.*, 2014, **26**, 3433–3440.

399 M. Nurunnabi, Z. Khatun, G. R. Reeck, D. Y. Lee and Y.-k. Lee, *ACS Appl. Mater. Interfaces*, 2014, **6**, 12413–12421.

400 K. Deisseroth, *Nat. Methods*, 2011, **8**, 26–29.

401 D.-W. Park, A. A. Schendel, S. Mikael, S. K. Brodnick, T. J. Richner, J. P. Ness, M. R. Hayat, F. Atry, S. T. Frye, R. Pashaie, S. Thongpang, Z. Ma and J. C. Williams, *Nat. Commun.*, 2014, **5**, 5258.

402 S. C. P. Williams and K. Deisseroth, *Proc. Natl. Acad. Sci. U. S. A.*, 2013, **110**, 16287.

403 S. Lee, I. Jo, S. Kang, B. Jang, J. Moon, J. B. Park, S. Lee, S. Rho, Y. Kim and B. H. Hong, *ACS Nano*, 2017, **11**, 5318–5324.

404 J. Kim, M. Kim, M.-S. Lee, K. Kim, S. Ji, Y.-T. Kim, J. Park, K. Na, K.-H. Bae, H. Kyun Kim, F. Bien, C. Young Lee and J.-U. Park, *Nat. Commun.*, 2017, **8**, 14997.

405 C. Choi, M. K. Choi, S. Liu, M. S. Kim, O. K. Park, C. Im, J. Kim, X. Qin, G. J. Lee, K. W. Cho, M. Kim, E. Joh, J. Lee, D. Son, S.-H. Kwon, N. L. Jeon, Y. M. Song, N. Lu and D.-H. Kim, *Nat. Commun.*, 2017, **8**, 1664.

406 T. Wang, H. Yang, D. Qi, Z. Liu, P. Cai, H. Zhang and X. Chen, *Small*, 2018, **14**, 1702933.

407 T. Xue, S. R. Bongu, H. Huang, W. Liang, Y. Wang, F. Zhang, Z. Liu, Y. Zhang, H. Zhang and X. Cui, *Chem. Commun.*, 2020, **56**, 7041–7044.

This journal is © The Royal Society of Chemistry 2023

J. Mater. Chem. A, 2023, **11**, 6016–6063 | **6063**